The Dissertation Committee for Seyoung Kim certifies that this is the approved version of the following dissertation:

Electron Transport in Graphene Transistors and Heterostructures: Towards Graphene-based Nanoelectronics

Committee:

Emanuel Tutuc, Supervisor

Sanjay K. Banerjee, Supervisor

Allan MacDonald

Ananth Dodabalapur

Jack C. Lee

Leonard F. Register

Electron Transport in Graphene Transistors and Heterostructures: Towards Graphene-based Nanoelectronics

by

Seyoung Kim, B.S.E.E.; M.S.E.

DISSERTATION

Presented to the Faculty of the Graduate School of

The University of Texas at Austin

in Partial Fulfillment

of the Requirements

for the Degree of

DOCTOR OF PHILOSOPHY

The University of Texas at Austin

May, 2012

To my parents

Acknowledgments

During my Ph.D. study I have incurred a tremendous debt to many people, and this limited space would not be enough to express all my sincere appreciation and gratitude to them. My days here at the University of Texas at Austin would have not been quite fruitful as it has been, if I had not encountered those great people who decorated my graduate life with meaningful and memorable moments. First and foremost, I would like to take this opportunity to express my gratitude to my academic advisors, Professor Emanuel Tutuc and Professor Sanjay K. Banerjee, who have guided me with patience and sincerity through my graduate studies. They devoted their expertise, knowledge and experience to nurture my still fledging identity as a member of academia, and I feel chiefly indebted for the insightful advice and encouraging support they have provided me. My special thanks go to Dr. Luigi Colombo for sharing his wisdom on dielectric deposition, and also my committee members, Professors Allan MacDonald, Ananth Dodabalapur, Jack C. Lee and Leonard F. Register for their valuable advices on this dissertation.

I would like to extend my sincere and heartfelt appreciation to my colleagues, with whom I feel very fortunate to have worked together. I greatly appreciate Insun Jo for all the collaborations and friendship. My gratitude also goes to my former group members, Yonghyun Kim, Junghyo Nah, Tackhwi Lee, Se-Hoon Lee, Davood Shahrjerdi, Fahmida Ferdousi, Mustafa Jamil, Tarik Akyol and to current group members, En-Shao Liu, Babak Fallahazad, David Dillen, Micah Points, Jae Hyun Ahn,

Kyounghwan Kim, Kayoung Lee, Kamran Varahramyan, Jiwon Chang, Dharmendar Reddy, Chris Corbet, Michael Ramon, Hema Chandra Prakash Movva, Dax Crum, Junghwan Yeom, Donghwi Koh and Sangwoo Kang. The knowledge and experience they have shared with me as well as the teamwork we have built have been truly invaluable assets to my research. Colleagues from MacDonald group, Hongki Min, Jeil Jung, Dagim Tilahun and Wang-Kong Tse, certainly deserve my sincere appreciation.

My friends, regardless how far apart we are now, have always taken care of me and motivated me even at my worst moments: my five-year roommate Jaeyong Chung, Flower Four members Donghyuk Shin and Ick-jae Yoon, and Jungho Jo, Minkyu Jeong, Dam Sunwoo, Eunjung Jang, Joonsoo Kim, Heejung Park, Joonsoo Lee, Kyoung Eun Kweon, Joonsung Park, Joonsung Yang, Min Jang, Keunwoo Park, Jongwon Lee and those who I have failed to mention here but will certainly be remembered. They deserve my heartfelt appreciation for the warm friendship they have shown me. All the members of the ECE softball team, UT Red Devils soccer team and PRC indoor soccer have been a great source of refreshment. I thank you all.

Finally, I wish to convey my overwhelming gratitude to my parents, Taeja Lee and Il Sang Kim, and everyone in my family for the unconditional love and unwavering support I have received from them. They have been truly an infinite fountain of strength and hope for me. I would like to offer them my immeasurable love and thanks.

SEYOUNG KIM

Austin, Texas

MAY 2012

Electron Transport in Graphene Transistors and Heterostructures: Towards Graphene-based Nanoelectronics

Seyoung Kim, Ph.D.
The University of Texas at Austin, 2012

Supervisors: Emanuel Tutuc, Sanjay K. Banerjee

Two graphene layers placed in close proximity offer a unique system to investigate interacting electron physics as well as to test novel electronic device concepts. In this system, the interlayer spacing can be reduced to value much smaller than that achievable in semiconductor heterostructures, and the zero energy band-gap allows the realization of coupled hole-hole, electron-hole, and electron-electron two-dimensional systems in the same sample. Leveraging the fabrication technique and electron transport study in dual-gated graphene field-effect transistors, we realize independently contacted graphene double layers separated by an ultra-thin dielectric. We probe the resistance and density of each layer, and quantitatively explain their dependence on the backgate and interlayer bias. We experimentally measure the Coulomb drag between the two graphene layers for the first time, by flowing current in one layer and measuring the voltage drop in the opposite layer. The drag resistivity gauges the momentum transfer between the two layers, which, in turn, probes the interlayer electron-electron scattering rate. The temperature dependence of the Coulomb drag above temperatures of 50 K reveals that the ground state in each layer is a Fermi liquid. Below 50 K we observe mesoscopic fluctuations of the drag resistivity, as a result

of the interplay between coherent intralayer transport and interlayer interaction. In addition, we develop a technique to directly measure the Fermi energy in an electron system as a function of carrier density using double layer structure. We demonstrate this method in the double layer graphene structure and probe the Fermi energy in graphene both at zero and in high magnetic fields. Lastly, we realize dual-gated bilayer graphene devices, where we investigate quantum Hall effects at zero energy as a function of transverse electric field and perpendicular magnetic field. Here we observe a development of $\nu = 0$ quantum Hall state at large electric fields and in high magnetic fields, which is explained by broken spin and valley spin symmetry in the zero energy Landau levels.

Table of Contents

List of Tables

List of Figures

Chapter 1

Introduction

After the first experimental discovery of its isolated form in 2004 [10], graphene, a single layer to few layers of carbon atoms sp^2-bonded in a honeycomb lattice, has been attracting not only physicists, but also device engineers who are eager to take advantage of its favorable properties in electronic devices. The most exciting aspect of graphene is its high mobility, which can, in principle, lead to high-speed field-effect transistors (FET). Carrier mobility in graphene is shown to reach 1,000,000 cm^2/Vs for levitated samples at low temperatures [11] and over 10,000 cm^2/Vs for samples supported on SiO_2 even at room temperature [12], which is about ten times higher than Si metal-oxide-semiconductor field-effect transistors (MOSFET), making it a potential high-mobility channel replacement for Si. Also, graphene is an intrinsically two-dimensional material. The planar nature of graphene enables the immediate application of highly developed planar process technology of today's semiconductor industry onto graphene-based device fabrication.

Device engineer's dream of building a graphene-based logic switch with ultimate high mobility and atomically thin body, however, is challenged by a high OFF-state current and non-saturating drain current observed in graphene devices because graphene is a zero-bandgap semiconductor or semi-metal. The Klein tunneling phenomenon, which is of a great interest to physicists [13], allows Dirac Fermions

in graphene [14] to tunnel through barriers, preventing the implementation of PN junctions. Nevertheless, the unique bandstructure, transport properties and thermomechanical stability make graphene a very promising material for high frequency FETs for analog and RF applications [15] and 'beyond complementary metal-oxide-semiconductor (CMOS)' nanoelectronic devices such as the bilayer pseudo-spin field-effect transistor (BiSFET) [2].

1.1 Overview

The purpose of this dissertation is to describe the author's experimental exploration carried out in two different graphene device structures: (1) dual-gated graphene transistors; and, (2) double layer graphene heterostructures. Realization of the dual-gated graphene FET structure was initially motivated by the necessity of local gate control. Most of the early graphene experiments were performed in devices with a single, global back gate, which limits the number of gates to one per substrate [10]. To fabricate a local top gate, a uniform gate dielectric deposition technique on graphene preferably with high dielectric constant (κ) is essential. However, it turned out to be difficult due to the chemical inertness of graphene's basal plane. We developed a technique to deposit a high-κ dielectric layer on the surface of graphene by atomic layer deposition (ALD) using an intentional nucleation layer and fabricated dual-gated single layer graphene FETs. The carrier mobility in graphene is primarily dominated by the extrinsic impurity scattering such as charged impurities in the dielectric [16]. Transport study and simple device modeling show that the impact of a top-gate dielectric stack on the transport characteristics is minimal, which en-

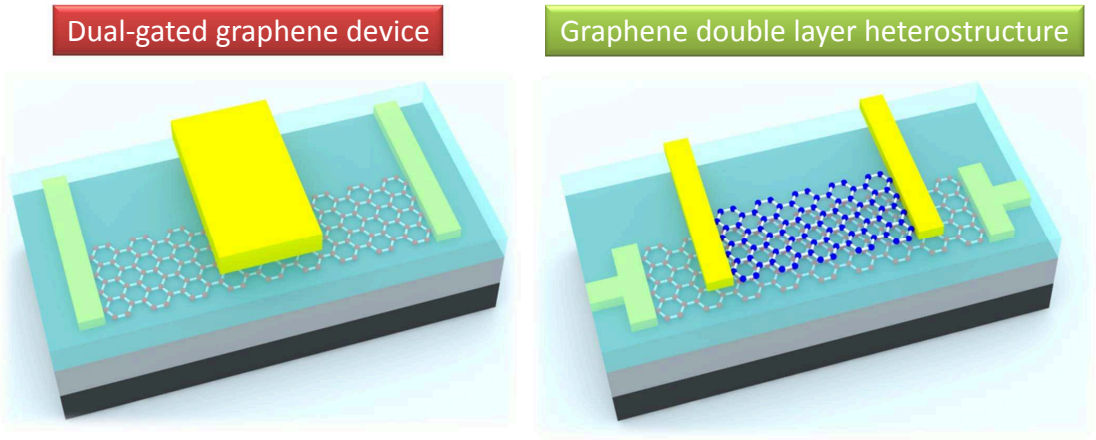

Figure 1.1: Two graphene device structures studied in this dissertation: a dual-gated single and bilayer graphene device (left), and double layer graphene heterostructure (right). Graphene is placed on a dielectric (grey)/back gate (black) stack and contacted/gated by metal (yellow).

sures that the dielectric layer does not significantly increase the carrier scattering, and consequently degrade the device characteristics [17]. The dielectric deposition technique, understanding of the electrostatics of the dual-gated system and simple analytical model we developed provide essential fundamentals to realize and study advanced graphene devices, such as double layer graphene systems.

Graphene AB-stacked bilayer, consisting of two closely coupled graphene layers with AB stacking, is an interesting material because of its transverse electric field (E field) tunable bandgap [18, 19]. Using this property, researchers have demonstrated higher on/off ratio graphene transistor [20], which is highly desirable for logic device applications. In a perpendicular magnetic field (B field), the density of states of bilayer graphene is quantized into discrete and degenerate energy levels, called Landau levels [21]. Interestingly, the zero-energy Landau levels in graphene bilayers are eight-fold degenerate, originated from two-spin, two-valley and two-orbital

degeneracy. Using a dual-gated bilayer graphene FET, where we can independently control the transverse E field and density with two gates, we experimentally observe the lifting of spin and valley degeneracy as a function of E field and B field [9, 22].

Double layer graphene heterostructures, where two graphene single layers are placed in a close proximity but electrically isolated, provide a fascinating test ground for interacting electron physics and novel device concepts. Using the dielectric deposition technique and graphene transfer technique, we demonstrate the double layer graphene devices and experimentally measured the Coulomb drag between carriers in two graphene layers for the first time [3]. We show that the Coulomb drag in graphene follows a temperature and carrier density dependence consistent with the Fermi liquid regime at temperatures higher than 50 K, while random drag fluctuations become dominant at temperatures below 50 K. The fluctuations result from the interplay between phase-coherent intralayer transport and interlayer interaction. The Coulomb drag provides key insight into the interaction between the two layers, as well as information on the ground states in individual graphene layers.

Careful modeling of the double layer structure led us to develop a technique to directly measure the relative Fermi energy in an electron system [4]. The principle of our technique is that when one graphene layer is at its charge neutrality point, the interlayer bias applied to the graphene layer is equal to the opposite layer's Fermi energy in units of eV. This method shares its basic principle with Kelvin probe measurement, using one of the two layers as a resistively detected Kelvin probe [23]. To demonstrate this method, we probed the Fermi energy as a function of carrier density in graphene at zero and in high magnetic fields using graphene double layer heterostructures. We showed that the Fermi velocity, Landau level spacing, and Landau

level broadening in graphene are accurately determined by our technique.

1.2 Outline

This dissertation is organized as follows. Chapter 2, Chapter 3 and Chapter 4 are focused on graphene double layer devices. Chapter 2 covers fabrication, layer characterization and modeling of graphene double layer system. In Chapter 3, the history and Boltzmann transport theory of Coulomb drag phenomenon, and Coulomb drag measurements performed in graphene double layers in average drag regime and fluctuation regime are discussed in detail. In Chapter 4, we describe a novel method to measure Fermi energy as a function of density using one of the graphene layers as a carrier density sensor in graphene double layers. The principle of the technique and the relative Fermi energy in graphene measured in zero and high magnetic fields are presented. In Chapter 5, spin-polarized to valley-polarized transition at $\nu = 0$ quantum Hall states (QHS) in a dual-gated bilayer graphene structure is presented. Fabrication, characterization, quantum Hall effects, and broken symmetry states caused by different mechanisms are discussed. Finally, in Chapter 6 the conclusions are summarized, and future studies are suggested.

Chapter 2

Graphene Double Layers

In this chapter, we discuss the fabrication and characterization of graphene double layer structure where two graphene single layers are independently contacted, positioned at close proximity and separated by an ultra-thin dielectric to prevent direct conduction between the layers. The motivation and advantages of studying graphene double layer system are first presented, followed by the experimental realization, layer density and resistivity characterization. We develop a simple model to explain layer density dependence on back gate and interlayer biases, which shows excellent agreement with experimental observation. The model serves as a powerful tool to analyze the Coulomb drag data in Chapter 3 and to develop a Fermi energy measurement technique in Chapter 4.

2.1 Introduction

Double layer systems formed by two layers of carriers in close proximity are a fascinating test ground for electron physics. In certain conditions, a layer degree of freedom in the system leads to ground states with no counterpart in the single layer case. In particular, the prospect of electron-hole-pair (indirect exciton) formation [24, 25] and dipolar superfluidity [26] has fueled the research of electron-hole double layers in GaAs/AlGaAs heterostructures [27, 28].

Graphene is a particularly interesting material to explore interacting double layers [29]. The flexible density control and the high Fermi energy as well as the intrinsically two-dimensional nature make graphene greatly advantageous in accessing interesting phenomena both experimentally and theoretically. The bandstructure of graphene featuring a zero energy bandgap and symmetric conduction and valence band enables seamless layer density control without excessive electric fields. As demonstrated in Chapter 2.4.2, layer densities as well as carrier type can be tuned by gate and interlayer bias in graphene double layers. This allows experimental exploration of physical quantities as a function of top and bottom layer density, which is not easily achievable in semiconductor quantum wells mainly due to absence of ambipolar contacts and difficulty in gating. The large Fermi energy in graphene favors correlated electron states at elevated temperatures, making mesoscopic physics accessible at higher temperatures than in other systems [30, 31] . The truly two-dimensional nature of graphene simplifies the experimental analysis and theoretical study because the consideration of finite layer thickness is not required, unlike in semiconductor quantum wells. With all these advantages, it is highly desirable to experimentally explore graphene double layers and extend our understanding of the electron-electron interactions and mesoscopic phenomena in two-dimensional systems.

Another important motivation which fueled the research on graphene double layer is the theoretical prediction that the graphene double layer system may work as a transistor which is expected to outperform current Si-based transistors. Using the graphene double layer structure, Banerjee *et al.* proposed a new type of transistor, called Bilayer pseudoSpin Field-Effect Transistor (BiSFET), which is expected to operate at lower voltage and lower power than currently possible with Complementary

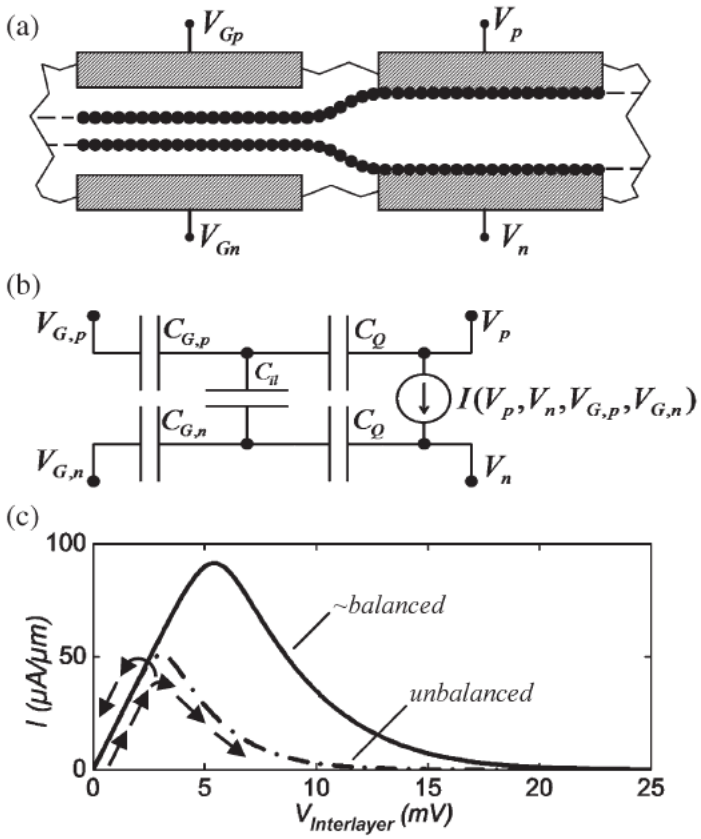

Figure 2.1: (a) Schematic representation of a BiSFET, (b) circuit model, and (c) expected interlayer current-voltage (I-V) characteristics for the BiSFET. Adapted from Ref.[2].

Metal-Oxide-Semiconductor (CMOS) Field-Effect Transistors (FETs) [2]. The basic principle of BiSFET operation is as follows. In normal conditions and the interlayer resistance is very high in BiSFET since two graphene layers are separated by a thin, but highly insulating dielectric layer [Figure 2.1(a)]. Under certain conditions, electrons in one layer and holes in the other layer can make pairs resulting in electron-hole pairs/exciton condensates (Bosons) [30], which dramatically lower the interlayer resistance. Using this phenomenon, one can operate a graphene double layer system as a transistor. Since the condensation condition can be easily broken by small voltage bias, the interlayer current (I) vs voltage (V) curve shows negative differential resistance behavior [Figure 2.1(c)]. The theoretical prediction of electron-hole pairing and feasibility of the novel device idea provide strong motivation to experimental realization and exploration of such system.

Here, we describe the fabrication of an independently contacted graphene double layer, and characterize the system by transport measurements.

2.2 Realization of Graphene Double Layers

In this section, we discuss the fabrication process of our independently contacted graphene double layers in detail. The realization of independently contacted graphene double layers requires two crucial ingredients: (1) an ultrathin, yet highly insulating, dielectric layer on graphene to separate the two layers; (2) a method to align and position another graphene layer on a pre-existing graphene device with minimum or no degradation in material quality for the second layer. To produce the double layer structure, we start from a standard back-gated single layer graphene device on

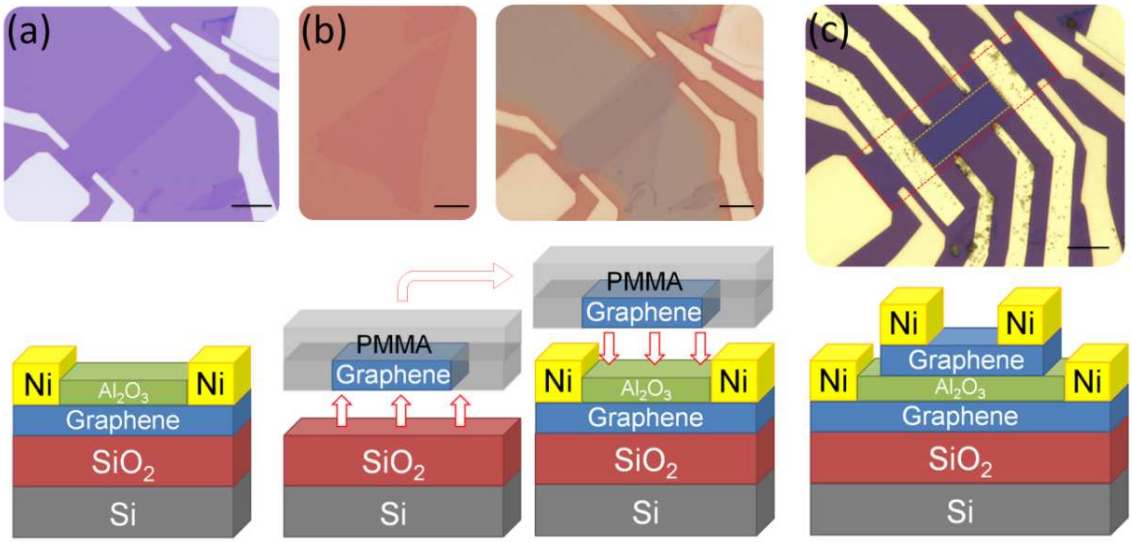

Figure 2.2: Optical micrograph and schematic representation (bottom) of the fabrication process of an independently contacted graphene double layer (BiSFET2). (a) A bottom-gated single layer graphene device with Hall bar geometry and with Al_2O_3 interlayer dielectric on top. (b) Top graphene layer is detached from a separate substrate and transferred onto the pre-established device. (c) e-beam lithography and metal deposition define top layer contacts. The scale bars in all panels are 10 μm. Adapted from Ref.[3].

SiO_2/Si substrate and deposit thin Al_2O_3 layer by first depositing an Al nucleation layer, followed by atomic layer deposition (ALD) [Figure 2.2(a)], and then transfer another graphene captured in poly(methyl methacrylate) (PMMA) membrane onto the bottom graphene layer [Figure 2.2(b)]. Top layer contacts defined by standard electron beam (e-beam) lithography and metal deposition complete a graphene double layer device [Figure 2.2(c)]. The further details of each step are discussed in the following subsections.

2.2.1 Back-gated graphene device

The first step in fabrication of a graphene double layer device is to establish a back-gated single layer graphene device. Graphene flakes used in this study are mechanically exfoliated from natural graphite (NGS Naturgraphit GmbH) onto a 280-300 nm thick SiO_2 dielectric, thermally grown on a highly doped Si substrate with an As doping concentration of $\sim 10^{20} cm^{-3}$ (Addison Engineering Inc.) as illustrated in Figure 2.2. We put a small graphite piece on the low-tack semiconductor tape (Ultratape), and peel it off as many times as possible. Then, we place the tape on the SiO_2/Si substrate, apply some pressure, and detach the tape to transfer thin graphite flakes onto the substrate. Now, we can bring the substrate to an optical microscope and inspect the surface until we hunt a usable single layer graphene flake. This technique is widely used and thin graphene sheets down to single layer of high quality can be found. The 280-300 nm thick SiO_2 is chosen to maximize the contrast between the graphene flake and substrate [32]. A brief O_2 plasma cleaning of SiO_2 surface before exfoliation helps adhesion between graphene and SiO_2.

E-beam lithography, metal liftoff and etching step are used to define a Hall bar on the bottom layer as exemplified in Figure 2.4. A single e-beam resist layer with 4% 996K PMMA is spin-coated on the surface at low final spin-speed as well as low acceleration rate in order to minimize damage on graphene flake; otherwise, graphene samples are easily ruptured at this step. An e-beam evaporator (CHA Industries), or thermal evaporator (Denton Vacuum, LLC) is used to deposit metal contacts consisted of a 50 nm-thick Ni or a combination of 5-nm Cr and 40-nm Au.

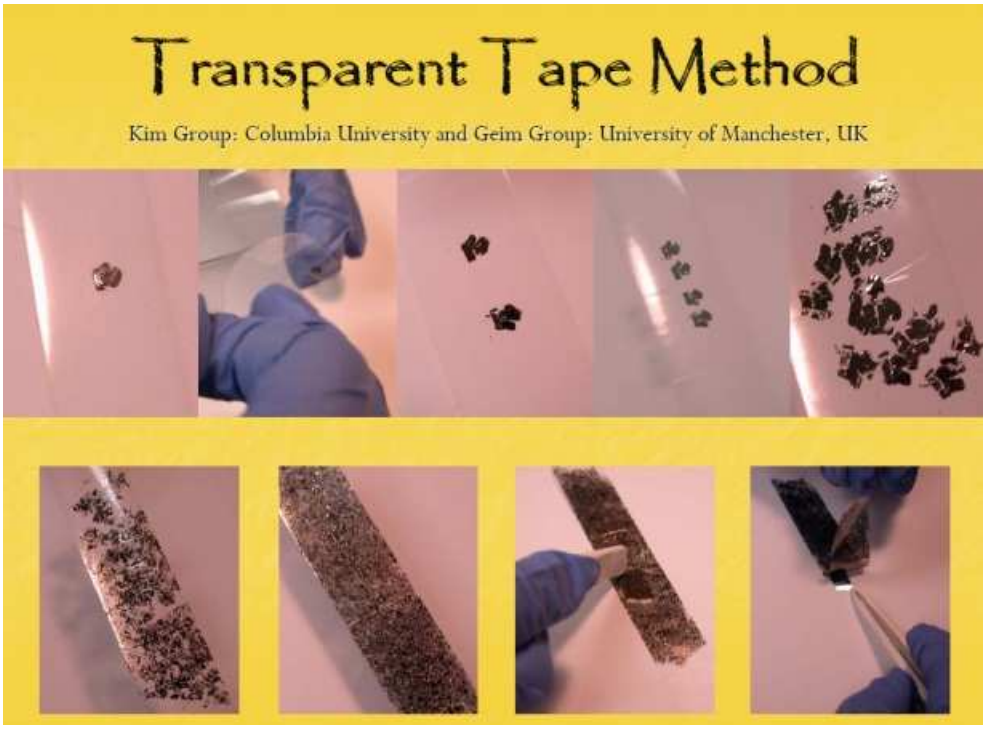

Figure 2.3: Mechanical exfoliation of graphene flakes from a natural graphite chunk onto a SiO_2 substrate.

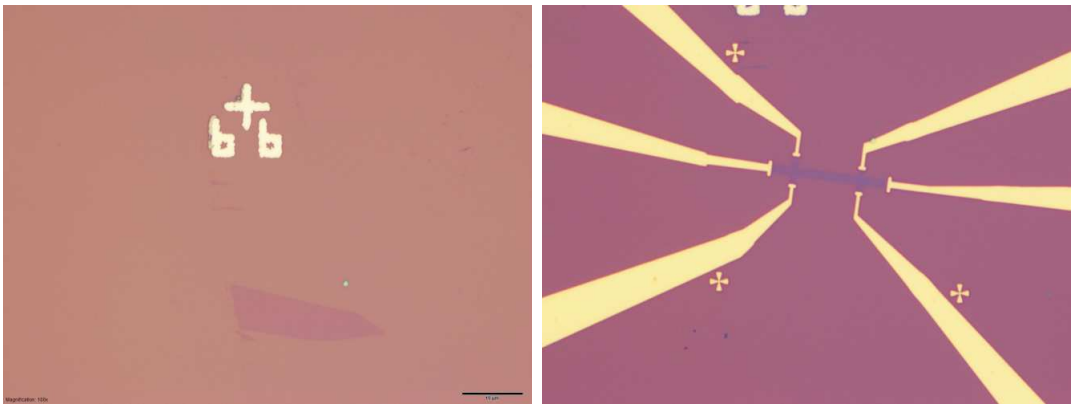

Figure 2.4: Optical images of the bottom layer graphene in BiSFET15 as-exfoliated (left) and after Hall bar device fabrication (right). The scale bar is 20 μm which applies for both panels. Large numbers and a cross in the left panel and small crosses in the right panel serve as alignment markers for e-beam lithography steps.

2.2.2 Interlayer dielectric

Direct deposition of high-κ dielectric materials, such as Al_2O_3 and HfO_2, on graphene by H_2O-based ALD is difficult because of the hydrophobic nature of graphene basal plane. Y. Xuan *et al.* reported that a trial to grow high-κ Al_2O_3 layer on a HOPG surface by ALD leads to a selective growth only at the steps between graphite layers, where the broken carbon bonds along the terraces serve as 1D nucleation center to initiate ALD process [33]. Therefore, some groups tested functionalization of graphene's surface to achieve dielectric layer growth on graphene by ALD [15, 34–37].

Our approach in enabling high-κ dielectric layer to grow on graphene by ALD is to provide intentional nucleation sites on the inert surface of graphene. We deposit a single or a few atomic layers of Al layer on the surface of graphene by e-beam evaporation prior to the Al_2O_3 layer growth by ALD, as illustrated in Figure 2.5. A thin and uniform Al layer covering the target graphene surface introduces plenty of homogeneous nuclei and allows subsequent Al_2O_3 film growth. The growth of Al_2O_3 on graphene by out technique is verified by atomic force microscope [Figure 2.6, right panel], and the complete oxidation of the nucleation layer is also confirmed by X-ray photoelectron spectroscopy.

After confirming the uniform growth of Al_2O_3 on graphene, we deposit a 4- to 8-nm thick Al_2O_3 on the back-gated single layer graphene device using our technique [17]. First we deposit a 1- to 2-nm Al interfacial layer by e-beam evaporator, and trasfer the graphene device into our ALD chamber (Savannah, Cambridge Nano Tech Inc.) *ex-situ*. Alternating H_2O and Al_2O_3 precursor steps corresponding to the target

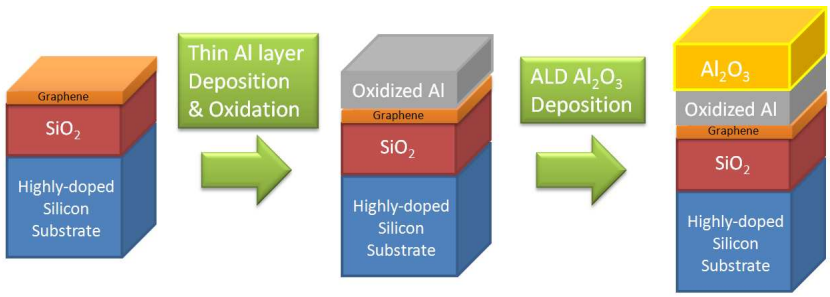

Figure 2.5: Introducing a thin layer of Al by e-beam evaporation provides nucleation sites on graphene for subsequent ALD growth.

thickness (0.92 nm/cycle) are performed to grow 3- to 5-nm-thick Al_2O_3 [Figure 2.2 (a)]. Graphene top-gated devices with ultrathin, 2.5 nm Al_2O_3 (1.5 nm Al + 1.2 nm Al_2O_3 by ALD) were demonstrated without significant interlayer leakage current, evincing the scalability of this technique.

2.2.3 Top graphene layer fabrication

In the previous section we prepared a back-gated single layer graphene Hall bar with a thin Al_2O_3 dielectric layer grown by ALD, which will be used as a bottom graphene layer in a graphene double layer structure. Now, we prepare the second, top graphene layer on a separate SiO_2/Si substrate by mechanical exfoliation. Then we apply a few micron-thick PMMA film on the substrate and cure it. Next, the PMMA film capturing the graphene layer and some alignment marks are detached from the host substrate using an NaOH etch [38], forming a free-standing membrane. The membrane is placed face down on the substrate containing the bottom graphene layer [Figure 2.2 (b)] and aligned with it. A drop of deionized water is used as a lubricant to prevent damage of graphene layers during the transfer and alignment process. The

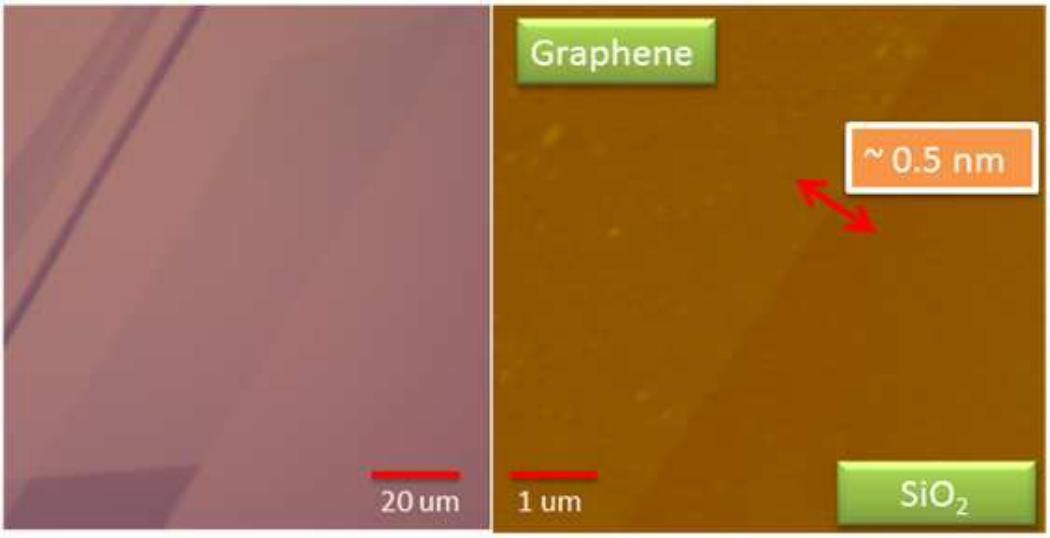

Figure 2.6: Optical microscopy of a single layer graphene flake with 20-nm Al_2O_3 layer grown by the technique (left), and atomic force microscopy of the same sample at the step between graphene and SiO_2 (right).

alignment is done manually with tweezers under the optical microscope. After the water completely dries, the transferred PMMA film adheres tightly on the surface. Using the as-transferred PMMA as an e-beam resist, a Hall bar device is subsequently defined on the top layer [Figure 2.2 (c)]. A stylus profilometer (Veeco Dektek 150) is used to measure the thickness of the PMMA film. If the PMMA film is too thick to perform normal e-beam lithography, we etch PMMA film with O_2 plasma until the thickness becomes less than 1 μm.

2.2.4 Sample statistics and summary

A total of sixteen back-gated, independently contacted graphene double layers have been fabricated in this study. Samples show mobilities between 5,400 and 11,000

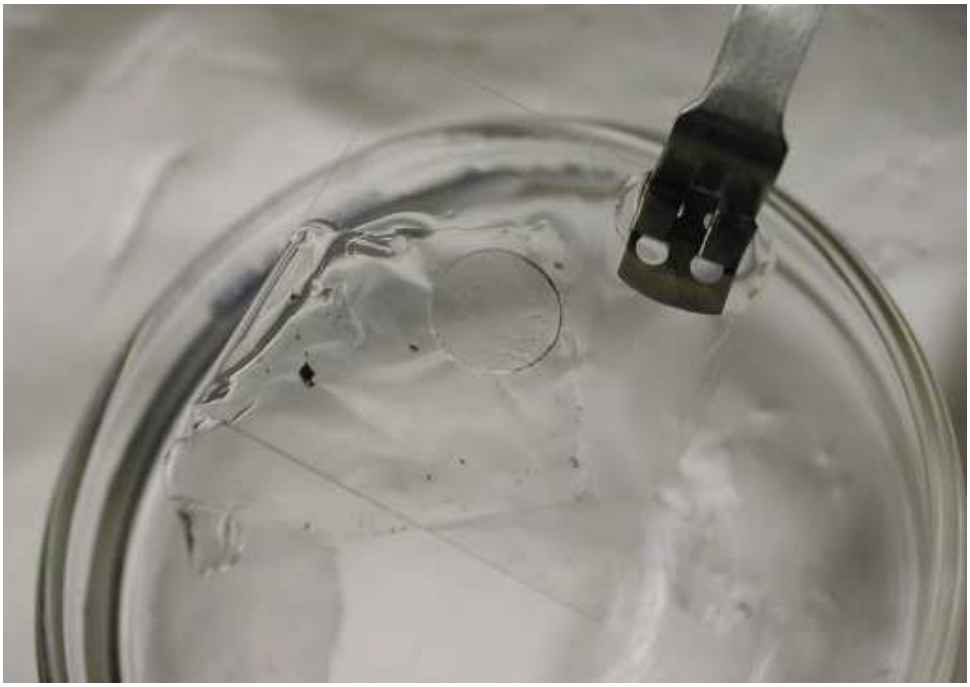

Figure 2.7: PMMA membrane detached from the substrate. Most of the graphene flakes exfoliated on the original substrate are captured in the PMMA film and detached. Large and thick graphene flakes are visible as black dots. A thin cover glass with a hole is used to handle the film to prevent any strain or damage.

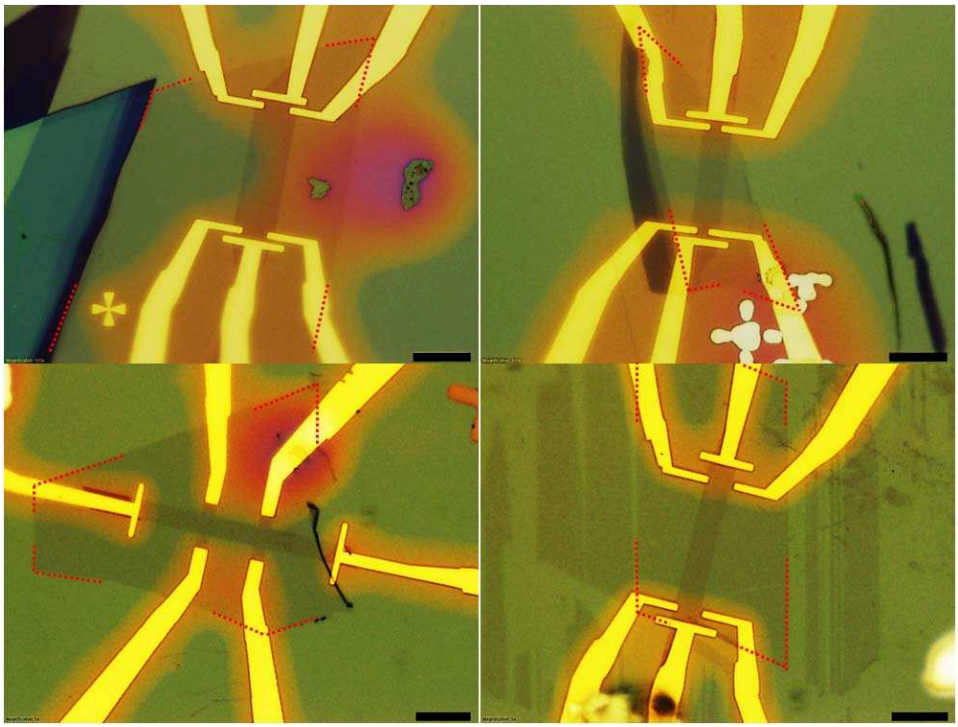

Figure 2.8: A top graphene layer captured in PMMA film is transferred and aligned with the bottom graphene layer. BiSFET6 (top left), BiSFET8 (top right), BiSFET12 (bottom left) and BiSFET13 (bottom right). The red guideline marks the selected edge of the transferred graphene layer for visibility. The scale bar is 10 μm.

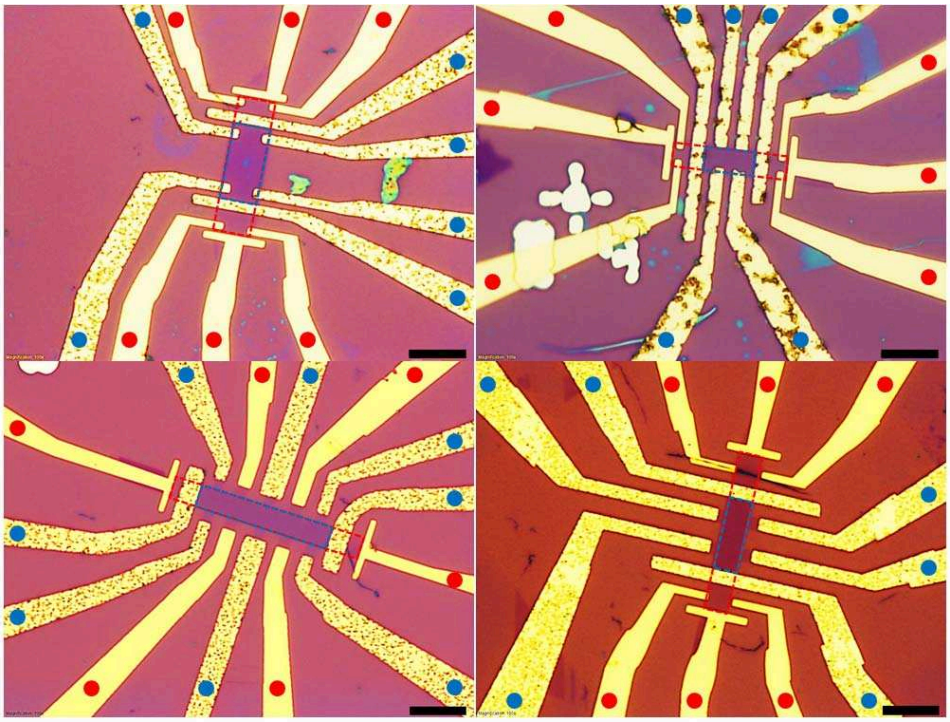

Figure 2.9: Back-gated graphene double layer devices: BiSFET6 (top left), BiSFET8 (top right), BiSFET12 (bottom left) and BiSFET13 (bottom right). Various device designs are used. The red (blue) dashed contour marks bottom (top) graphene layer, and red (blue) dots indicate bottom (top) contacts. The scale bar is 10 μm.

cm^2/Vs for the bottom layer, 4,500 and 10,000 cm^2/Vs for the top layer, and interlayer leakage resistance higher than 1 GΩ if measureable. The high mobility of the top layer confirms that the manual transfer process does not significantly degrade the quality of graphene. These structures are markedly different from graphene bilayers exfoliated from natural graphite consisting of two graphene monolayers in Bernal stacking [21]. We will discuss graphene AB-stacked bilayers in Chapter 5.

2.3 Layer Characterization and Modeling

We now turn to the individual layer characterization. Top (ρ_T) and bottom (ρ_B) layer resistivities measured as a function of V_{BG} in three different graphene double layer devices at T = 300 K are shown in Figure 2.10. We probe layer resistivities using small signal, low frequency lock-in techniques, and the potential of the both layers is held at zero (ground) for this measurement. The dependence of ρ_B on the applied V_{BG} shows ambipolar conduction and a finite resistance at the charge neutrality (Dirac) point, consistent with the expected response of gated single layer graphene where the dominant scatters are the charged impurities present in the dielectric [39] and/or at the interface between graphene and substrate as further discussed in Figure 2.12 [16]. More interestingly, the top layer resistivity also changes as a result of the applied V_{BG}. This observation indicates an incomplete screening of the gate-induced electric field by the bottom layer; the electric field originated from the back gate is not entirely screened by the bottom layer and partially reaches to the top layer to modulate top layer density and, consequently, layer resistivity. This effect is most pronounced in the vicinity of the bottom layer's charge neutrality point,

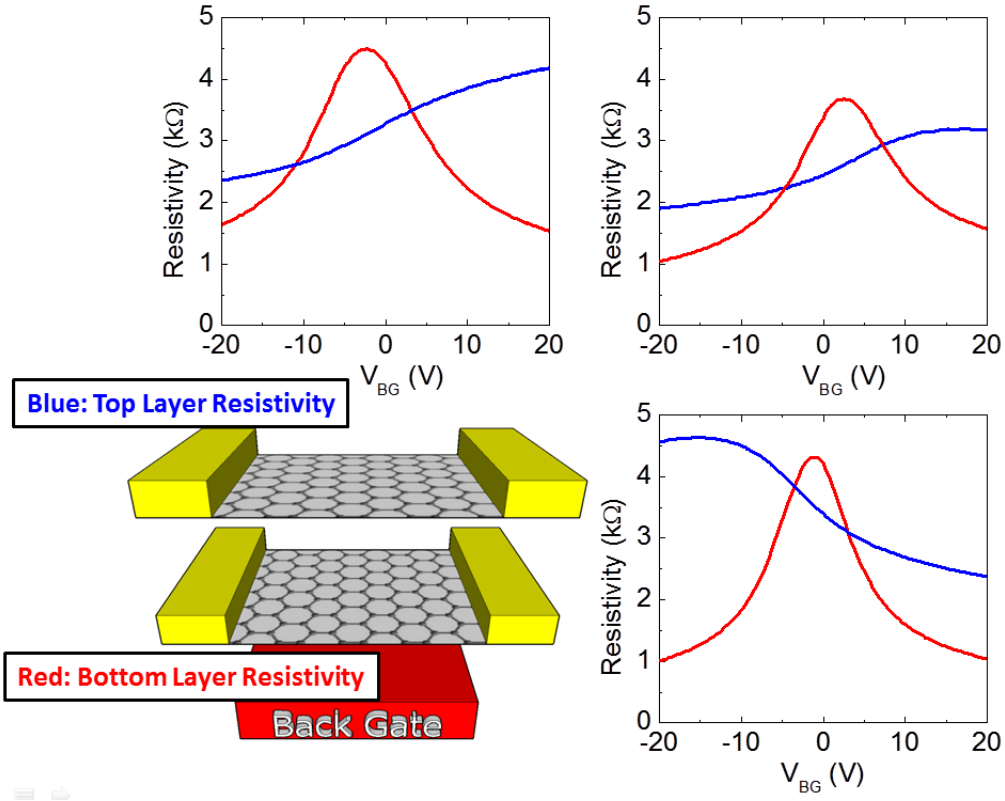

Figure 2.10: ρ_B (red) and ρ_T (blue) vs V_{BG} measured at T = 300 K and in various devices: BiSFET5(top left), BiSFET4 (top right), and BiSFET6 (bottom right).

a consequence of the reduced density of states in graphene. As we show below, we can quantitatively explain the V_{BG} dependence of layer densities and resistivities.

2.3.1 Layer density modeling: single layer graphene

We first analyze and model the layer density dependence on V_{BG} in a back-gated graphene single layer in order to understand that in a double layer graphene device. Let us assume that we have a back-gated single layer graphene whose carrier density (n) can be controlled by an applied bias on the metallic back gate (V_{BG}) as

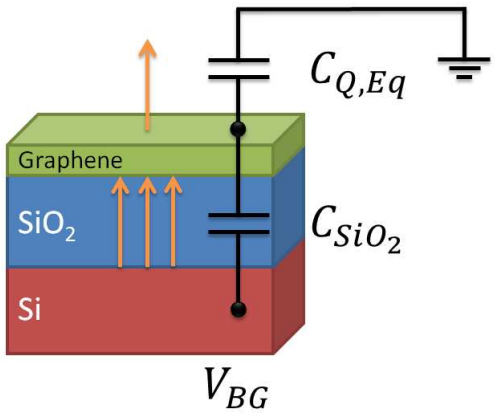

Figure 2.11: Schematic representation of a back-gated graphene structure and equivalent circuit. The orange arrows demonstrate electric field originated from the Si back gate when positive V_{BG} is applied and graphene layer is grounded.

shown in Figure 2.11. Regarding this system as a parallel plate capacitor, the layer density in graphene and V_{BG} can be related as:

$$V_{BG} = \frac{en}{C_{BG}}. \tag{2.1}$$

Here we assume that the work function difference between single layer graphene (4.5 - 4.8 eV [40]) and the highly doped Si gate is zero, and graphene is at its charge neutrality point when $V_{BG} = 0$ V. If there are practically infinite electron states available in graphene at zero energy as in a metal plate, the above equation is correct, and the carrier density will be simply proportional to the applied V_{BG}. However, it is not the case for an atomically thin graphene layer where the density of states is limited.

Due to the Pauli's exclusion principle, only one electron can occupy a certain quantum state. If all the electron states available at the given energy are fully occupied, then the system's Fermi energy needs to be increased to allow electrons occupy

the higher energy states. This effect can be included in Equation 2.1 by adding the Fermi energy term:

$$V_{BG} - \frac{E_F}{e} = \frac{en}{C_{BG}}, \tag{2.2}$$

where E_F denotes the Fermi energy of the channel material. In other words, one needs to pay some penalty, Fermi energy or surface potential, to induce charge carriers when only a limited number of states are available. Most of the electric fields are screened by the graphene layer while the rest penetrates through the graphene layer and sets the surface potential of graphene at E_F/e. This phenomenon of a quantum origin can be modeled as a series capacitance, named quantum capacitance [41] in the equivalent circuit as shown in Figure 2.11.

The quantum capacitance is a conceptual capacitance adopted to explain the change of surface potential or Fermi energy in the host material at a certain charge carrier density. By definition, C_Q is directly proportional to the density of states in the host material, and C_Q in graphene can be written as:

$$C_Q = e^2 D\left(E\right) = \frac{2}{\pi(\hbar v_F)^2} E = \frac{2e^2}{\hbar v_F \sqrt{\pi}} \sqrt{n}, \tag{2.3}$$

where $D\left(E\right) = (2/\pi(\hbar v_F)^2)E = (2/\hbar v_F\sqrt{\pi})\sqrt{n}$ is the density of states in graphene. Equation 2.2 can be rearranged to explicitly contain C_Q as illustrated in Figure 2.11:

$$V_{BG} = \left(\frac{1}{C_{BG}} + \frac{1}{C_{Q,Eq}}\right) en, \tag{2.4}$$

where the equivalent quantum capacitance $C_{Q,Eq}$ is half of C_Q due to the integration:

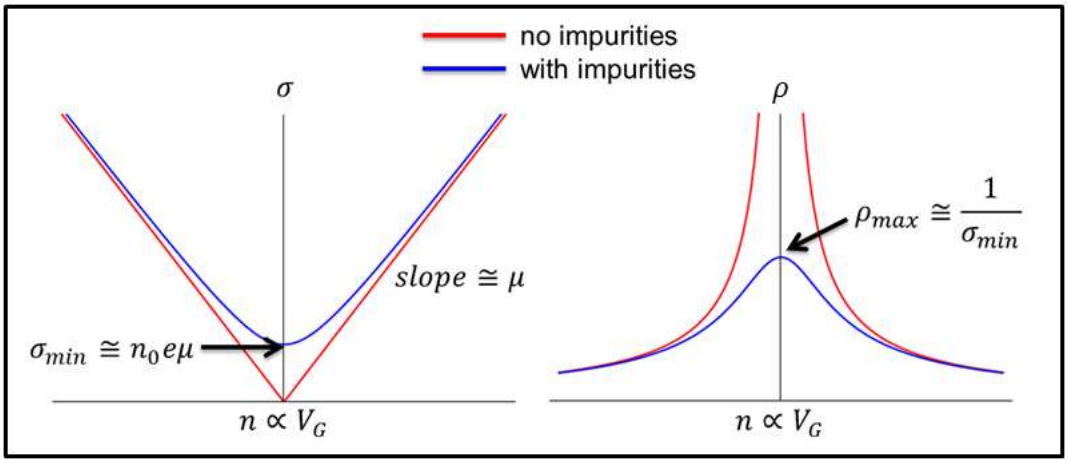

Figure 2.12: Conductivity and resistivity curves of single layer graphene with (blue) and without the presence of charged impurities (red). In realistic graphene devices placed on the non-ideal substrates, we expect to measure blue curves.

$$C_{Q,Eq} = \frac{e^2}{\hbar v_F \sqrt{\pi}} \sqrt{n}. \tag{2.5}$$

Equation 2.4 provides interesting observations: (1) the effect of quantum capacitance is negligible when C_Q is much larger than the geometrical capacitance, C_{BG} in this case; (2) when C_Q is small, equivalently when the density of states is small, C_Q affects the electrostatic profile in the system significantly. Therefore, following the $\sqrt{n}$ dependence, the effect of C_Q is maximized near the charge neutrality point in graphene, while the effect becomes insignificant at higher density.

Equation 2.2 as well as $E_F = \hbar v_F \sqrt{\pi n}$ in graphene provides an analytical solution of n as a function of V_{BG} [9]:

$$n\left[V_{BG}\right] = \left(\sqrt{\left(\frac{\hbar v_F \sqrt{\pi} C_{BG}}{2e^2} \right)^2 + \frac{C_{BG}}{e} V_{BG}} - \frac{\hbar v_F \sqrt{\pi} C_{BG}}{2e^2} \right)^2. \tag{2.6}$$

With this analytical expression, we can calculate the layer density at V_{BG}, and we can also calculate layer resistivity ρ using the following equation [17]:

$$\rho = \frac{1}{\sqrt{n^2 + n_0^2} e\mu}. \tag{2.7}$$

where μ is the layer mobility, n_0 represents the residual carrier concentration in graphene layer generated by charged impurities in the vicinity of the graphene channel [42], which should converge to zero for disorder-free graphene layer [16]. Figure 2.12 describes the effect of n_0 on the conductivity or resistivity of graphene: the minimum conductivity or maximum resistivity value is limited to a finite value by the existence of n_0.

We model the total resistance R_{total} of a graphene channel by extending Equation 2.7. By separating the total resistance into a contact resistance $R_{contact}$ and channel resistance $R_{channel} = N_{sq}/\sqrt{n^2 + n_0^2} e\mu$, we obtain:

$$R_{total} = R_{contact} + \frac{N_{sq}}{\sqrt{n^2 + n_0^2} e\mu}, \tag{2.8}$$

where the number of squares N_{sq}=L/W is defined by length (L) and width (W) of the channel. Equation 2.8 can be utilized to extract relevant device parameters such as $R_{contact}$, $n_0$and μ by fitting with the experimental data [17].

2.3.2 Layer density modeling: double layer graphene

Based on the understanding of the back-gated structure, we continue our discussion to understand the layer density dependence on V_{BG} in a graphene double

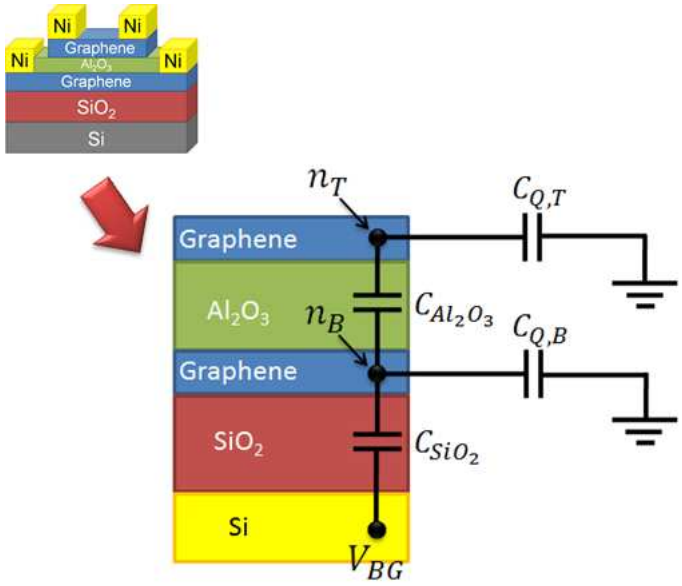

Figure 2.13: Schematic of a graphene double layer structure and equivalent circuit when both graphene layers are grounded. The quantum capacitances, $C_{Q,T}$ and $C_{Q,B}$, allow the finite surface potential in graphene layers.

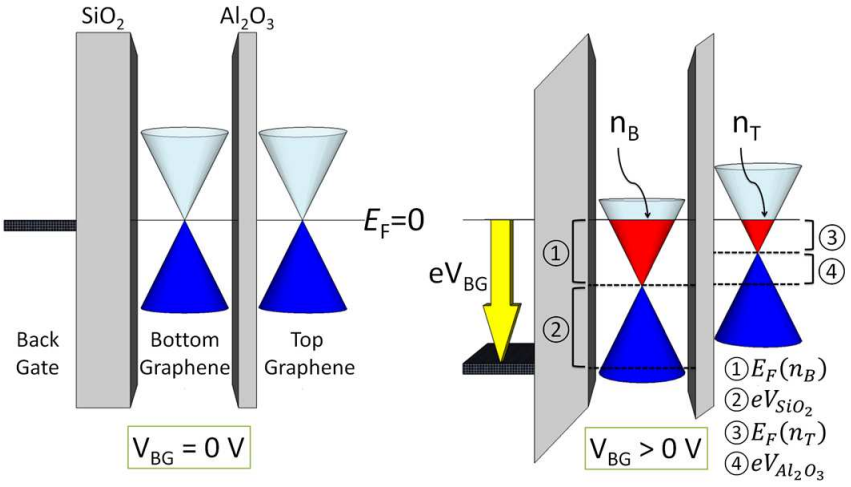

Figure 2.14: Band diagram across the graphene bilayer heterostructure at $V_{BG} = 0$ V (left), and at a positive V_{BG} (right). Both layers are assumed to be at the charge neutrality point and aligned with the back gate Fermi level at $V_{BG} = 0$ V. Adapted from Ref.[3].

layer structure, where a dielectric and another graphene layer is deposited on the top of the back-gated single layer [Figure 2.13]. Figure 2.14 illustrates the band diagram of the graphene bilayer at $V_{BG} = 0$ V. For simplicity, the gate Fermi energy and the charge neutrality point in the two layers are assumed to be at zero energy. Once a finite V_{BG} is applied, finite charge densities are induced in both top (n_T) and bottom (n_B) layers. We obtain two equations from the band diagram, which provides n_B and n_T at the given V_{BG}. As we discussed in the previous section, the difference between the gate and bottom layer Fermi level is distributed partly across the SiO_2 dielectric and partly on the Fermi energy of the bottom graphene layer:

$$eV_{BG} - E_F(n_B) = \frac{e^2(n_B + n_T)}{C_{SiO_2}}, \tag{2.9}$$

where $E_F(n) = \hbar v_F \sqrt{\pi\, n}$ is the Fermi energy in graphene measured with respect to the charge neutrality point at a carrier density n, e is the electron charge, $v_F = 1.1 \times 10^6 m/s$ is the Fermi velocity in graphene, and C_{SiO_2} denotes SiO_2 dielectric capacitance per unit area. $n_{B,T}$ and $E_F(n)$ are positive when the carriers are electrons, and negative when the carriers are holes. Compared to Equation 2.2, we have an additional n_T term because now we have another graphene layer to screen the gate-induced electric fields. Similarly, the Fermi energy difference between the two layers is responsible for the potential drop across the Al_2O_3 interlayer dielectric:

$$E_F(n_B) = \frac{e^2 n_T}{C_{Al_2O_3}} + E_F(n_T), \tag{2.10}$$

where $C_{Al_2O_3}$ is the Al_2O_3 dielectric capacitance per unit area. This equation is exactly the same form with Equation 2.2 if $E_F(n_B)$ is replaced with eV_{BG}, which

indicates that the bottom layer's surface potential works just as a gate bias to the top layer. Equations 2.9 and 2.10 can be solved self-consistently to determine n_B and n_T as a function of V_{BG}.

Once we obtain n_B and n_T as a function of V_{BG}, we can calculate ρ_B and ρ_T using the following equation [17]:

$$\rho_{B,T} = \frac{1}{\sqrt{n_{B0,T0}^2 + n_{B,T}^2} e\mu_{B,T}}, \tag{2.11}$$

where $\mu_B(\mu_T)$ is the bottom (top) layer mobility, $n_{B0}(n_{T0})$ represents the residual carrier concentration in bottom (top) layer generated by charged impurities. Figure 2.15 data show a good agreement between the measured layer resistivities and densities (symbols) in BiSFET2 and the calculations (solid lines) with n_{B0} =3.8 $\times$ 10^{11} cm^{-2}, n_{T0} = 6.3 $\times$ 10^{11} cm^{-2}, μ_B = 5,500 cm^2/Vs, μ_B = 4,500 cm^2/Vs, $V_{Dirac,TL}$ = -0.6 V and $V_{Dirac,BL}$ = -12 V, where $V_{Dirac,BL}$ indicates the position of $n_B = 0$ point expressed in V_{BG} and $V_{Dirac,TL}$ is the position of $n_T = 0$ point in terms of the top layer voltage. This confirms that the asymmetric and weak dependence of the top layer resistivities on V_{BG} observed in Figure 2.10 and Figure 2.15, is, in fact, an expected response originated from the quantum capacitance in the bottom layer. The layer mobilities, determined from Hall measurements, are μ_B = 5,400 cm^2/Vs and μ_T = 4,500 cm^2/Vs at T = 4.2 K.

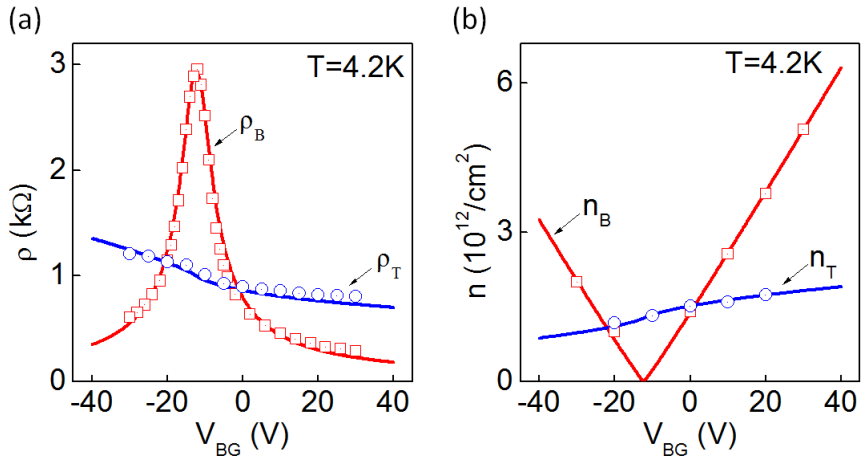

Figure 2.15: (a) Layer resistivities and (b) densities vs V_{BG} measured at T = 4.2 K in BiSFET2. Depending on V_{BG}, both electrons and holes can be induced in the bottom layer; the top layer consistently contains electrons in the available V_{BG} window, owing to unintentional doping. Experimental data (shapes) and calculation (lines) show excellent agreement. Adapted from Ref.[3].

2.4 Layer Characterization with an Applied Interlayer Bias

2.4.1 Measurement setup

We have so far discussed the layer density and resistivity as a function of a single back gate bias, V_{BG}. This significantly limits our measurement range in terms of layer densities because it is impossible to control layer densities in top and bottom layer separately. Here we introduce an interlayer bias technique which enables independent layer density control. We use an acoustic transformer (Jensen Transformers, model: SUB-BB) to isolate one layer and apply a DC bias to the layer while the other layer is maintained at ground potential. This configuration allows simultaneous measurement of the top and bottom layer resistivity as a function of back gate bias and the interlayer bias, using small signal, low frequency lock-in techniques and with

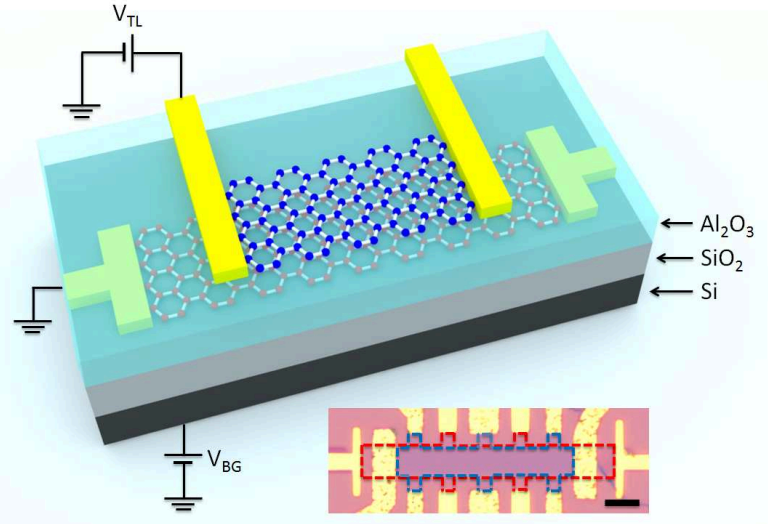

Figure 2.16: Schematic representation of a double layer graphene device, and measurement configuration. Lower right: optical micrograph of a complete device, BiSFET12. The red (blue) contour marks the bottom (top) layer. The scale bar is 5 μm. Adapted from Ref.[4].

two lock-in amplifiers (Stanford Research Systems, SR-830). In all the interlayer bias measurements discussed in this dissertation, we ground the bottom layer ($V_{BL} = 0$) and apply an interlayer bias to the top layer (V_{TL}) as shown in Figure 2.16. We investigate three samples, BiSFET8, BiSFET11 and BiSFET12 for the discussion in this section, and focus on data collected from BiSFET12 with a 7.5 nm thick Al_2O_3 interlayer dielectric and an interlayer resistance larger than 1 GΩ. Both layer mobilities are 10,000 cm^2/Vs at 0.4 K confirmed by Hall measurements.

Data in Figure 2.18 show the longitudinal resistivity of the bottom (ρ_B) and top (ρ_T) layer measured as a function of V_{TL}, and at different V_{BG} values. For simplicity V_{BG} and V_{TL} are referenced with respect to the bias values at which both layers are at the Dirac point: V_{BG} = 8 V, V_{TL} = -0.01 V. The data $\rho_{B,T}$ vs V_{TL}

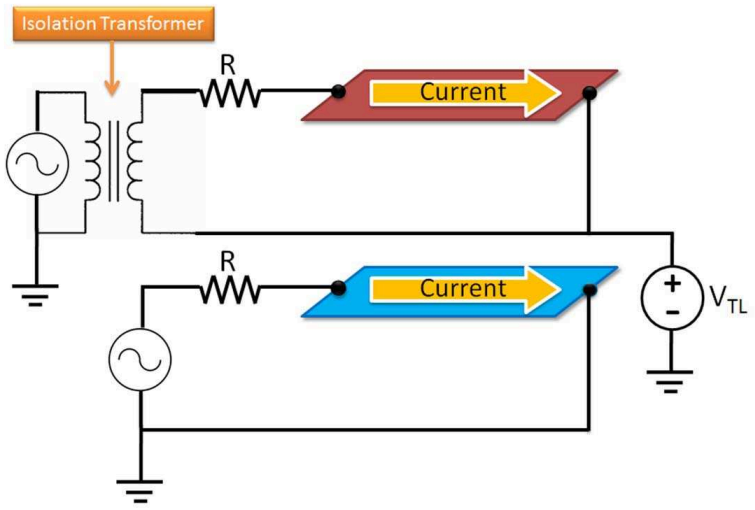

Figure 2.17: Layer resistivity measurement setup using an isolation transformer, which isolates the top layer from the rest of the circuit. A DC bias, V_{TL}, can be applied to the top layer.

exhibit the symmetric, ambipolar transport characteristic typical in graphene [16], and with a charge neutrality point which is V_{BG} dependent.

The shift of the charge neutrality point of the bottom layer as a function of V_{BG} is explained by picturing the bottom layer as a dual-gated graphene single layer, with the Si substrate as a bottom gate and the top graphene layer serving as a top gate. In fact, the slope of the charge neutrality point of bottom layer in the V_{BG} and V_{TL} plane provides is equal to the ratio between the back gate and top graphene gate capacitance, $-C_{SiO_2}/(C_{Al_2O_3} \parallel C_{Q,T})$. Using this expression, we can determine $C_{Q,T}$ from the observed slope and, consequently, the density of states in the top layer since $C_Q = e^2 D(E)$ [43]. Now we can explain that the non-linear slope found near the zero voltage point, where the charge neutrality points of both layers are crossing, results from the reduced $C_{Q,T}$ at low n_T. At high n_T, where $C_{Q,T} \gg C_{Al_2O_3}$ the

expression is approximated to be $-C_{SiO_2}/C_{Al_2O_3}$. With $C_{SiO_2} = 12$ nF/cm^2, we can determine the interlayer dielectric capacitance to be $C_{Al_2O_3} = 340$ nF/cm^2, which is also confirmed by Hall measurements. The non-linearity found near the zero voltage point, where the charge neutrality point of both layers are crossing, results from the reduced quantum capacitance in the top graphene, providing the information on top layer's density of states.

On the other hand, the dependence of the ρ_T vs V_{TL} data on V_{BG} is more subtle, and implies an incomplete screening of the back gate electric field by the bottom layer as discussed in the previous section. A large portion of the electric field originated from the back gate will be screened by the bottom layer, while the remaining portion penetrates the bottom layer and reaches to the top layer, modulating the position of the top layer charge neutrality point. With the interlayer bias, it will be clearly shown that the amount of the electric field penetrating the bottom layer is directly dependent on the Fermi energy in the bottom layer.

2.4.2 Layer density modeling with an interlayer bias

The interlayer bias term can be added in Equations 2.9 and 2.10 to quantitatively explain the top (n_T) and bottom (n_B) layer carrier density dependence on V_{BG} and V_{TL} using a modified band diagram model. Figure 2.19 shows two examples of band diagrams in the graphene double layer, at finite V_{BG} and $V_{TL} = 0$ V [Figure 2.19 (left)], as well as finite V_{TL} and $V_{BG} = 0$ V [Figure 2.19 (right)]. For simplicity the back gate Fermi energy and the two graphene layers' charge neutrality points are assumed to be aligned at $V_{BG} = 0$ V and with both layers at ground potential.

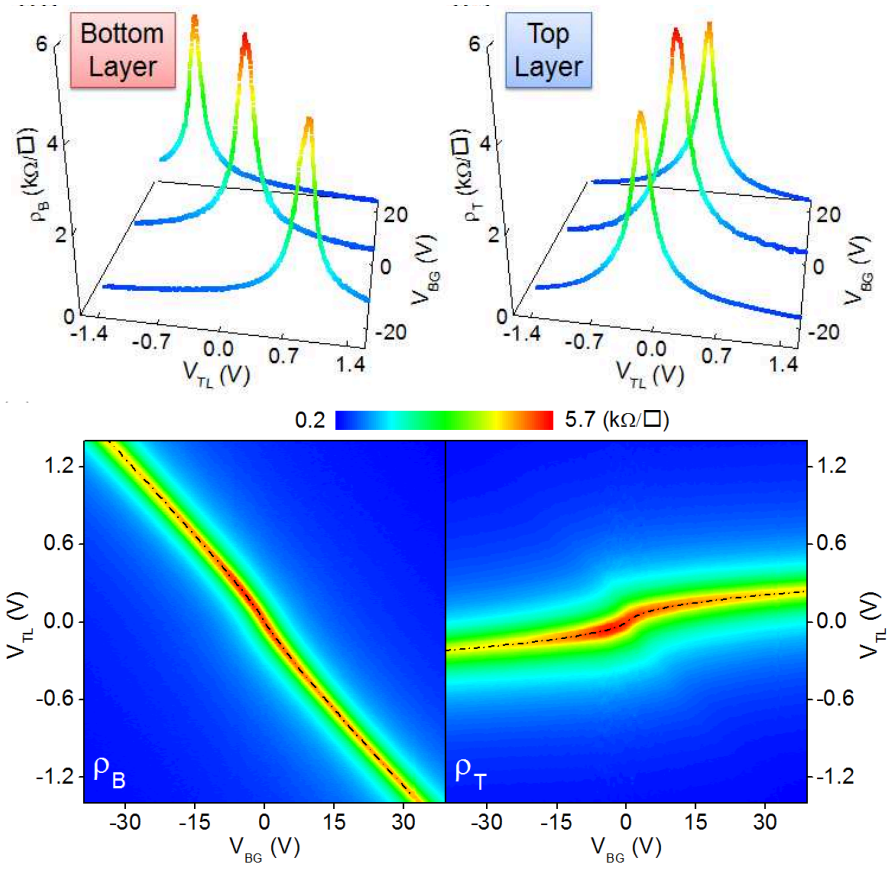

Figure 2.18: Layer resistivities as a function of V_{TL} and V_{BG} measured at T = 0.4 K (BiSFET12).

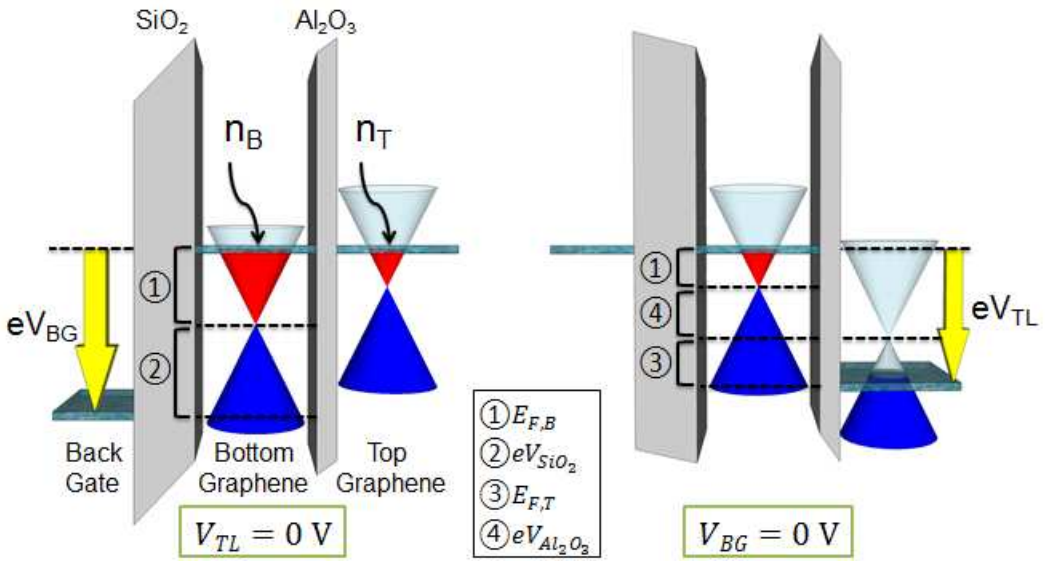

Figure 2.19: Band diagram of a graphene double layer under an applied back gate (left) or interlayer bias (right). Adapted from Ref.[4].

In Figure 2.19 (right) the V_{TL} bias is assumed to be positive, resulting in electrons (holes) induced in the bottom (top) layer. We emphasize that no assumptions are made with regard to the E_F dependence on n_B and n_T, and this model should work for any combination of top and bottom layer materials.

From the band diagram, we write the applied V_{BG} as the sum of the potential drop across the SiO_2 dielectric and the Fermi energy of the bottom layer:

$$eV_{BG}=\frac{e^2(n_B+n_T)}{C_{SiO_2}}+E_F\left(n_B\right), \tag{2.12}$$

which is equivalent to Equation 2.9. The effect of interlayer bias will be indirectly included through the term, n_T. The difference between $E_F(n_B)$ and applied V_{TL} bias is the sum of the potential drop across the Al_2O_3 dielectric and the Fermi energies of the two layers:

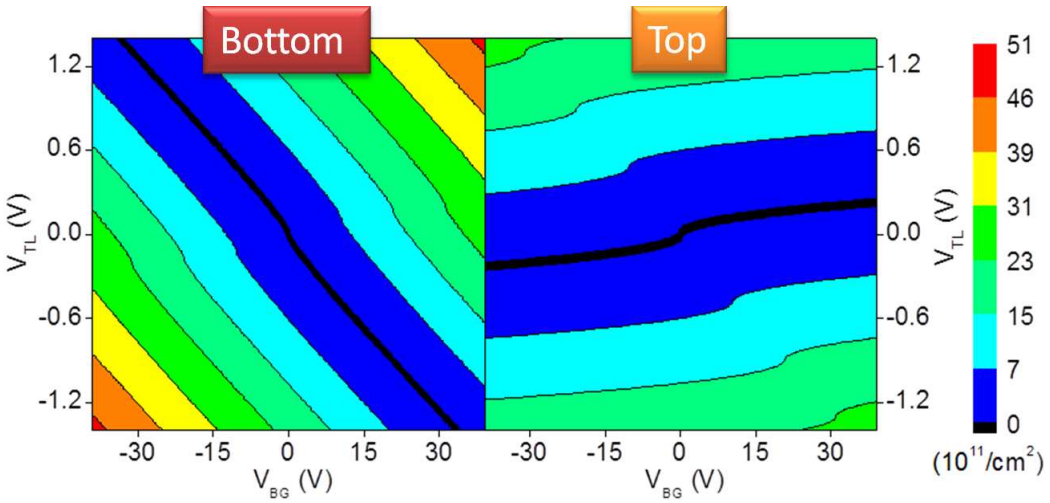

Figure 2.20: Calculated layer densities using the band diagram model, plotted in V_{BG} and V_{TL} plane with $C_{SiO_2} = 12$ nF/cm^2, $C_{Al_2O_3} = 340$ nF/cm^2 and $v_F = 1.1 \times 10^6$ m/s.

$$E_F\left(n_B\right) - eV_{TL} = \frac{e^2 n_T}{C_{Al_2O_3}} + E_F(n_T). \tag{2.13}$$

By solving Equations 2.12 and 2.13 self-consistently with the theoretical $E_F(n)$ for single layer graphene, $E_F(n) = \hbar\, v_F \sqrt{\pi\, n}$, where $v_F = 1.1 \times 10^6$ m/s is the Fermi velocity in graphene, the carrier densities in top and bottom graphene layer can be calculated. Figure 2.20 shows the top (right panel) and bottom (left panel) layer density calculation results in contour plots. We present both hole and electron density with a positive sign for better visibility. The position of the charge neutrality lines in Figure 2.18 and zero density lines in Figure 2.20 shows an excellent agreement, indicating that the model describes well the layer density dependence on back gate and interlayer biases in the double layer system.

2.4.3 Layer density modeling with residual carrier density

We can improve the accuracy of the density model by including the effect of the residual carrier density in the top (n_{T0}) and bottom (n_{B0}) layers. Due to the electric-hole puddles, the finite conductivity present even at the charge neutrality point can be modeled using a residual carrier density [16]. The non-zero carrier density at charge neutrality point alters not only the conductivity profile, but also density of states or quantum capacitance C_Q in a graphene layer. Xia *et al.* directly measured C_Q in graphene and showed that inclusion of the residual carrier density explains the constant and finite C_Q measured near the charge neutrality well [44].

To account for the effect of the residual carrier density in our model, we include the parameters n_{B0} and n_{T0} in the E_F expression:

$$E_F^*\left[n_{B,T}\right] = \frac{e^2 n_{B,T}}{\frac{1}{2}C_Q^*} = \hbar v_F \sqrt{\pi} \frac{n_{B,T}}{\left(n_{B,T}^2 + n_{B0,T0}^2\right)^{\frac{1}{4}}}, \tag{2.14}$$

where $C_Q^* = 2e^2 / \left(\hbar v_F \sqrt{\pi} \sqrt{\left(n_{B,T}^2 + n_{B0,T0}^2\right)^{\frac{1}{4}}}\right)$. This expression allows $E_F^*\left[n_{B,T}\right] = 0$ at $n_{B,T} = 0$, and $E_F^*\left[n_{B,T}\right] \approx E_F\left[n_{B,T}\right]$ at $n_{B,T} \gg 0$ as shown in Figure 2.21 where the Fermi energy calculated as a function of layer density at different residual carrier densities are plotted. By substituting the modified Fermi energy expression into Equations 2.12 and 2.13, we obtain the following equations:

$$V_{BG} = \frac{e\left(n_B + n_T\right)}{C_{SiO_2}} + \frac{E_F^*\left(n_B\right)}{e}, \tag{2.15}$$

$$\frac{E_F^*\left(n_B\right)}{e} - V_{TL} = \frac{e\ n_T}{C_{Al_2O_3}} + \frac{E_F^*\left(n_T\right)}{e}. \tag{2.16}$$

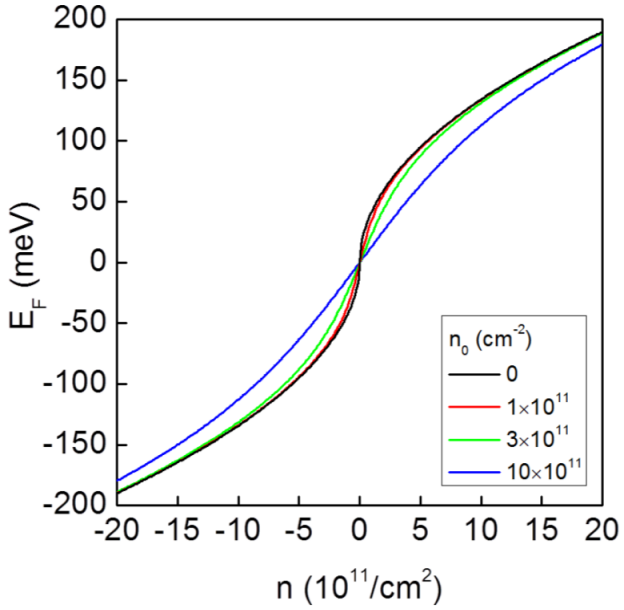

Figure 2.21: Fermi energy in graphene $E_F^*[n_{B,T}] = \hbar v_F \sqrt{\pi} n_{B,T} / \left(n_{B,T}^2 + n_{B0,T0}^2\right)^{\frac{1}{4}}$ as a function of layer density at different residual carrier density n_0 values.

By solving these two equations self-consistently, we can calculate layer densities including the impact of finite residual carrier densities on $E_F(n)$ in both layers.

2.5 Conclusion

We fabricate graphene double layer devices, measure each layer's resistivity and density and develop a simple model to explain layer densities and resistivities dependence on V_{BG} and V_{TL}. Both layers show high mobility values which are comparable to single layer graphene devices fabricated on SiO_2 substrate. The results confirm that the transfer process does not degrade the top layer's quality. A good understanding of each layer's characteristic serves as a cornerstone for analyzing interesting phenomena in the graphene double layer system in the following chapters.

Chapter 3

Coulomb Drag in Graphene Double Layers

In this chapter, we discuss the Coulomb drag phenomenon between electrons residing in a graphene double layer system consisting of two, independently contacted graphene single layers separated by an ultrathin dielectric. We provide a general overview on the history and physics of Coulomb drag and report experimental observation of Coulomb drag in graphene for the first time. At temperatures higher than 50 K, the Coulomb drag follows a temperature and carrier density dependence consistent with the Fermi liquid regime. As the temperature is reduced, the Coulomb drag exhibits giant fluctuations with increasing amplitude, thanks to the interplay between coherent transport in the graphene layer and interaction between the two layers.

3.1 Coulomb Drag: Overview

Electron-electron interaction is responsible for fascinating effects in condensed matters, and provides a research area of great interest both theoretically and experimentally. It plays a leading role in phenomena ranging from high-temperature superconductivity and the fractional quantum Hall effect, to Wigner crystallization, the Mott transition and Coulomb gaps in disordered systems. However, probing

electron-electron interaction by transport measurements is difficult because electron-electron interaction has only an indirect effect on the transport properties in single layer structures. This is a direct consequence of the momentum and total current conserving nature of the electron-electron interaction in perfectly pure, translationally invariant systems. For example, the average total current probed by transport measurement is unaffected by electron-electron momentum transfer since the total momentum is conserved.

In spite of the above argument, direct measurement of the electron-electron interaction is possible if one considers a system consisted of two closely coupled layers. Although total momentum in the system is conserved, that within an individual layer is not necessarily conserved. This is the principle that led theorists to investigate an effect which became known as Coulomb drag. The idea of measuring Coulomb drag as a direct probe of electron-electron interaction in a double layer system was first suggested by Pogrebinskii in 1977 [45] and later by Price in 1983 [46]. They predicted that for two conducting systems separated by an insulator, there will be a drag of carriers in one layer due to the direct Coulomb interaction with the carriers in the other layer. The fundamental importance of the Coulomb drag measurement lies in the fact that it probes the interlayer scattering rate *directly*.

Hubner and Shockley carried out the earliest drag-like experiment, who measured phonon-assisted electron-electron scattering in Si n-p-n vertical junction in 1960 [47]. While the measurement set up was identical, the mechanism of electron-electron scattering was not Coulomb-originated because of the large layer separation, $\sim$100 μm.

Improvement in molecular beam epitaxy (MBE) technology and device fabrica-

tion technique enabled the realization of independently contacted and closely spaced GaAs/AlGaAs double layer heterostructures, and new transport measurements such as Coulomb drag became possible. The first drag measurements in the modern format were performed in 1989 by Solomon *et al.* at IBM [48], who measured the Coulomb drag currents induced in a 100-nm-thick, three-dimensional GaAs gate by the drive current in two-dimensional channel in GaAs substrate. In 1991, Gramila *et al* at Bell Laboratories measured the Coulomb drag effect between two separate two-dimensional layers for the first time [49]. They found that the magnitude, sign, temperature and barrier thickness dependence of the observed drag to be in a reasonable agreement with Coulomb drag theory derived by MacDonald *et al.* using Boltzmann transport theory. Sivan *et al.* first investigated the Coulomb drag between electrons and holes in 1992 [50], reporting an order of magnitude larger momentum transfer rate than theory predicted. This experiment was the first one seeking evidence for exciton formation and condensation using Coulomb drag as a probing tool; however, unambiguous signature of electron-hole pairing was not found.

The Coulomb drag measurement in double layer structures is similar to a typical four-point resistance measurement, in which a current is driven through two wires and the voltage drop in the *same* layer is measured using the other two wires. In the Coulomb drag measurement, the drive current (I_{drive}, I_2) is still driven through two wires in one layer (drive layer, active layer or layer 2); however, the longitudinal voltage drop (V_{drag}, V_1) is measured in the *opposite* layer (drag layer, passive layer or layer 1) as illustrated in Figure 3.1. If there is no interaction between the layers, there would be no voltage drop measured in the drag layer which is electrically isolated from the drive layer.

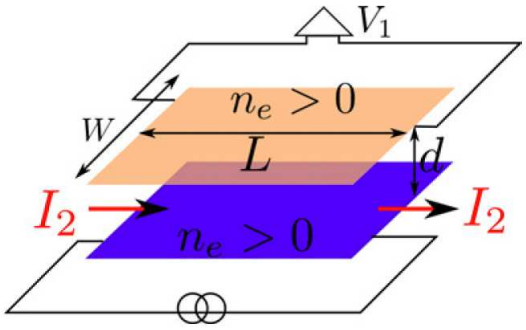

Figure 3.1: Graphical representation of a Coulomb drag experiment. Adapted from Ref.[5].

The electrons or holes in one layer can feel the *screened* Coulomb potential due to the electrons or holes in the other layer. The net result of this interaction is that the carriers in the drive layer try to transfer a portion of the momentum they have to the carriers in the other layer. This means that if we open the circuit in the drag layer, a small pile up of charge occurs in one end of the layer, which results in a voltage appearing across the drag layer. This is the V_{drag} we measure experimentally. In the linear response regime, we can define a drag resistance as:

$$\rho_{drag} = \frac{W}{L}\frac{V_1}{I_2}. \tag{3.1}$$

We define the sign of drag resistivity as positive when the electric fields in both layers are in the same direction. Since drag carriers are always swept away in the direction in which drive layer carriers moves, the sign of V_{drag} is negative when the carrier types in two layers are of the same type, and V_{drag} becomes positive when two layers have different type of carriers [Figure 3.2].

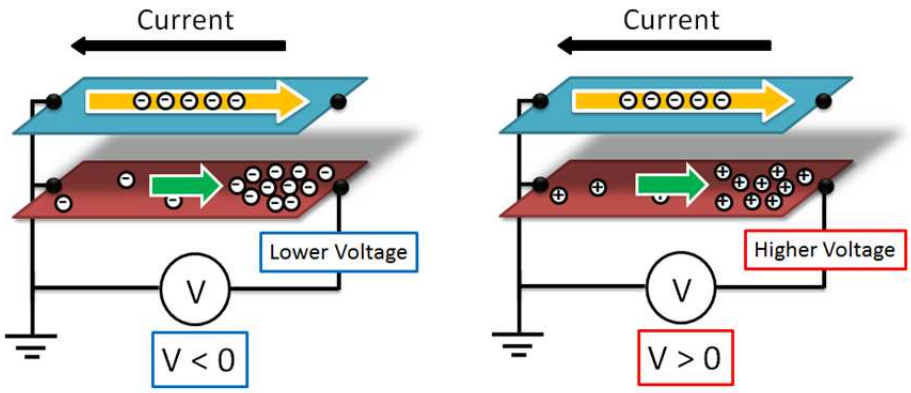

Figure 3.2: Sign of V_{drag} corresponding to carrier types in double layers. A positive (negative) V_{drag} is measured when both layers have opposite (identical) carrier types.

3.2 Boltzmann Transport Analysis of Coulomb Drag

The first full derivation of a Coulomb drag equation using Boltzmann transport theory was published by Jauho and Smith in 1993 [51]. While the Boltzmann approach is semi-classical and unable to capture higher order quantum effects, Boltzmann transport analysis of Coulomb drag provides a transparent origin of the terms appearing in the resultant equation such as temperature, interlayer separation and carrier densities. Therefore, it is instructive to study the Coulomb drag theory using Boltzmann formalism. Alternative approaches of the problem were reported by the collective excitation approach [52], the Green's function formalism starting from the Kubo formula [53, 54] and memory function formalism [55].

3.2.1 Boltzmann transport equation

The Boltzmann transport equation describes the evolution of the non-equilibrium distribution function, f($\mathbf{r}$, $\mathbf{k}$, t), as a function of time. The distribution function rep-

resents the probability of finding a carrier with crystal momentum, $\mathbf{k}$, at location $\mathbf{r}$, at time t. Since the distribution function provides each and every particle's position and momentum as a function of time, various macroscopic quantities of interest, such as carrier density, current density and kinetic energy density, can be obtained from it. The way one can derive the distribution function is to solve the Boltzmann transport equation.

Let us first derive the Boltzmann transport equation in the general form. In the absence of collisions, the particle conservation requires that:

$$f\left(\mathbf{r}+\mathbf{d}r,\mathbf{v}+\mathbf{d}vt+dt\right)=f\left(\mathbf{r},\mathbf{v},t\right). \tag{3.2}$$

In the presence of collisions, events which can change the momentum of a particle, but not its position at the given time, the consequent change in the distribution function must be equal to the change by collisions:

$$f\left(\mathbf{r}+\mathbf{d}r,\mathbf{v}+\mathbf{d}v,t+dt\right)-f\left(\mathbf{r},\mathbf{v},t\right)=dt\left(\frac{\delta f}{\delta t}\right)_{col}. \tag{3.3}$$

By taking the infinitesimal limit, we obtain the Boltzmann transport equation:

$$\frac{\delta f}{\delta t}+\frac{\delta f}{\delta \mathbf{r}}\mathbf{v}+\frac{d\mathbf{k}}{dt}\frac{\delta f}{\delta \mathbf{k}}=\left(\frac{\delta f}{\delta t}\right)_{col}, \tag{3.4}$$

and in the three-dimensional form,

$$\frac{\delta f}{\delta t}+\mathbf{v}\cdot\nabla_{\mathbf{r}}f+\mathbf{a}\cdot\nabla_{\mathbf{v}}f=\left(\frac{\delta f}{\delta t}\right)_{col}. \tag{3.5}$$

The Boltzmann transport equation cannot be solved analytically in most of the cases, and several approximations are made to solve the equation. One method to simplify the Boltzmann transport equation is to linearize it and restrict the changes in the distribution function to small deviations from equilibrium:

$$f(\mathbf{k}) = f^{\circ}(\mathbf{k}) + \Delta f(\mathbf{k}), \tag{3.6}$$

where $f^{\circ}(\mathbf{k})$ represents the equilibrium distribution function (Fermi-Dirac distribution) and the change in the distribution function, $\Delta f(\mathbf{k})$, is assumed to be small. Another technique is the relaxation time approximation which will be discussed in the later subsection. We will use the linearization and relaxation time approximation in the following chapters to derive the expression for the Coulomb drag resistivity.

3.2.2 Interlayer momentum transfer rate

The momentum transfer rate from the drive layer to the drag layer, dP/dt, is equal to the total force applied on the carriers in the drag layer due to the induced electric field in the drag layer, E_1:

$$\frac{dP}{dt} = n_1 e E_1. \tag{3.7}$$

By definition, the drag resistivity is expressed as follows:

$$\rho_{drag} = \frac{W}{L}\frac{V_1}{I_2} = \frac{E_1}{J_2} = \frac{E_1}{\sigma_2 E_2} = \frac{1}{\sigma_2 E_2 n_1 e}\frac{dP}{dt}, \tag{3.8}$$

where $E_{1,2}$ is the electric field, $J_{1,2}$ is the current density, $\sigma_{1,2}$ is the resistivity in the corresponding layer. Equation 3.8 indicates that we can obtain the expression for ρ_{drag} by knowing the explicit expression for $n_1 e E_1$ and, consequently, dP/dt. This can be done by solving the Boltzmann transport equation, Equation 3.4, for the drag layer, layer 1.

Since no current is flowing in the drag layer, the electron distribution is taken to be the equilibrium one, the Fermi-Dirac distribution. Then, the Boltzmann transport equation for the drag layer (layer 1) becomes:

$$\frac{d\mathbf{k_1}}{dt}\frac{\delta f_{\mathbf{k1}}}{\delta \mathbf{k_1}} = \left(\frac{\delta f_{\mathbf{k_1}}}{\delta t}\right)_{col}. \tag{3.9}$$

Since

$$\hbar\frac{d\mathbf{k_1}}{dt} = -e\mathbf{E_1}, \tag{3.10}$$

Equation 3.9 becomes:

$$\frac{(-e)\mathbf{E_1}}{\hbar}\frac{\delta f_{\mathbf{k1}}}{\delta \mathbf{k_1}} = \left(\frac{\delta f_{\mathbf{k_1}}}{\delta t}\right)_{col}. \tag{3.11}$$

Now we define x axis along the direction of current flow and y axis to be orthogonal to x axis. If we multiply both sides of Equation 3.11 by k_{1x} and sum over the states $k_1\sigma_1$, we obtain:

$$2\int \frac{d\mathbf{k_1}}{(2\pi)^2} k_{1x}\frac{(-e)\mathbf{E_1}}{\hbar}\frac{\delta}{\delta k_{1\mathrm{x}}} f^{\circ}_{\mathbf{k_1}} = \sum_{\sigma_1}\int \frac{d\mathbf{k_1}}{(2\pi)^2} k_{1x}\left(\frac{\delta f_{\mathbf{k_1}}}{\delta t}\right)_{col}, \tag{3.12}$$

and after partial integration the left side becomes:

$$2\int \frac{d\mathbf{k_1}}{(2\pi)^2} k_{1x} \frac{(-e)\mathbf{E_1}}{\hbar} \frac{\delta}{\delta k_{1\mathrm{x}}} f^{\circ}_{\mathbf{k_1}} = \frac{eE_1 n_1}{\hbar} = \frac{1}{\hbar}\frac{dP}{dt}. \tag{3.13}$$

Therefore,

$$\frac{dP}{dt} = \hbar \sum_{\sigma_1} \int \frac{d\mathbf{k_1}}{(2\pi)^2} k_{1x} \left(\frac{\delta f_{\mathbf{k_1}}}{\delta t}\right)_{col}. \tag{3.14}$$

Substituting Equation 3.14 into Equation 3.8, we obtain the expression for ρ_{drag}:

$$\rho_{drag} = \frac{\hbar}{\sigma_2 E_2 n_1 e} \sum_{\sigma_1} \int \frac{d\mathbf{k_1}}{(2\pi)^2} k_{1x} \left(\frac{\delta f_{\mathbf{k_1}}}{\delta t}\right)_{col}. \tag{3.15}$$

Now, we need to derive an explicit form for the collision rate term to calculate the drag resistivity.

3.2.3 Collision term calculation

3.2.3.1 Intralayer scattering

It is informative to calculate the collision term in a single layer before we discuss the double layer case. In a single layer, we can construct the collision integral by considering the phase space restrictions to scattering, along with the scattering probability, $\Omega_{k\to k'}$. $\Omega_{k\to k'}\ \mathrm{d}k'$ indicates the probability per unit time that an electron in a state $\mathbf{k}$ will be scattered into a state with the same spin, contained in an infinitesimal element $\mathrm{d}k'$ around k'. The probability per unit time of an electron in

a state $\mathbf{k}$, leaving d$\mathbf{k}$ via collisions is the sum of all the probabilities for the electron *existing* in a state $\mathbf{k}$ to scatter into a certain state $\mathbf{k}^{'}$ which is *empty*:

$$\left(\frac{\delta f(\mathbf{k})}{\delta t}\right)_{out} = -f\left(\mathbf{k}\right)\int\left(\frac{1}{2\pi}\right)^{d}\Omega_{\mathbf{k}\rightarrow\mathbf{k}'}\left(1-f(\mathbf{k}^{'})\right)d\mathbf{k}^{'}. \tag{3.16}$$

The probability per unit time of an electron in a state $\mathbf{k}^{'}$, leaving $d\mathbf{k}^{'}$ via collisions is the sum of all the probabilities for the electron *existing* in a state $\mathbf{k}^{'}$ to scatter into the state $\mathbf{k}$ which is *empty*:

$$\left(\frac{\delta f(\mathbf{k})}{\delta t}\right)_{in} = (1-f(\mathbf{k}))\int\left(\frac{1}{2\pi}\right)^{d}\Omega_{\mathbf{k}'\rightarrow\mathbf{k}}f(\mathbf{k}^{'})d\mathbf{k}^{'}. \tag{3.17}$$

Therefore, the total change in the distribution function by the collisions in a single layer is:

$$\begin{aligned}\left(\frac{\delta f(\mathbf{k})}{\delta t}\right)_{col} &= \left(\frac{\delta f(\mathbf{k})}{\delta t}\right)_{out}+\left(\frac{\delta f(\mathbf{k})}{\delta t}\right)_{in}\\ &= \int\left(\frac{1}{2\pi}\right)^{d}\left[\Omega_{\mathbf{k}'\rightarrow\mathbf{k}}\left(1-f\left(\mathbf{k}\right)\right)f(\mathbf{k}^{'})-\Omega_{\mathbf{k}\rightarrow\mathbf{k}'}f(\mathbf{k})(1-f(\mathbf{k}^{'}))\right]d\mathbf{k}^{'},\end{aligned} \tag{3.18}$$

where $d=2$ for a Coulomb drag system where each layer is regarded as a mathematical two-dimensional plane.

3.2.3.2 Interlayer scattering

We are interested in the scattering events between charged particles in different layers. By applying the similar approach we used for the single layer scattering

case, we can derive the collision term for the interlayer scattering events. Since two incoming momenta ($\mathbf{k}_1$,$\mathbf{k}_2$) and two outgoing momenta ($\mathbf{k}_{1'}$,$\mathbf{k}_{2'}$) are involved in the double layer case, the scattering probability, Ω, is now a function of four momenta, and the occupancy of all four states must be taken into account. In addition, energy and momentum conservation need to be enforced by delta functions. The collision term for interlayer electron-electron scattering including spin summations is:

$$\left(\frac{\delta f(\mathbf{k_1})}{\delta t}\right)_{col} = \sum_{\sigma_{1'}\sigma_2\sigma_{2'}} \int \frac{d\mathbf{k_{1'}}}{(2\pi)^2} \int \frac{d\mathbf{k_2}}{(2\pi)^2} \int \frac{d\mathbf{k_{2'}}}{(2\pi)^2} \Omega\left(\mathbf{k_1}, \mathbf{k_2} \rightarrow \mathbf{k_{1'}}, \mathbf{k_{2'}}\right) \times \mathrm{S}\left(\mathrm{f}_{\mathbf{k_1}}, \mathrm{f}_{\mathbf{k_2}}, \mathrm{f}_{\mathbf{k_{1'}}}, \mathrm{f}_{\mathbf{k_{2'}}}\right) \delta\left(\mathbf{k_1}+\mathbf{k_2}-\mathbf{k_{1'}}-\mathbf{k_{2'}}\right) \delta\left(\varepsilon_{\mathbf{k_1}}+\varepsilon_{\mathbf{k_2}}-\varepsilon_{\mathbf{k_{1'}}}-\varepsilon_{\mathbf{k_{2'}}}\right), \quad (3.19)$$

where S function is defined as:

$$\mathrm{S}\left(\mathrm{f}_{\mathbf{k_1}}, \mathrm{f}_{\mathbf{k_2}}, \mathrm{f}_{\mathbf{k_{1'}}}, \mathrm{f}_{\mathbf{k_{2'}}}\right) = \mathrm{f}_{\mathbf{k_{1'}}} \mathrm{f}_{\mathbf{k_{2'}}} \left(1-\mathrm{f}_{\mathbf{k_1}}\right)\left(1-\mathrm{f}_{\mathbf{k_2}}\right) - \mathrm{f}_{\mathbf{k_1}} \mathrm{f}_{\mathbf{k_2}} \left(1-\mathrm{f}_{\mathbf{k_{1'}}}\right)\left(1-\mathrm{f}_{\mathbf{k_{2'}}}\right),$$

which explains the occupancy of in-flow and out-flow states. It is noteworthy that at the same distribution case ($\mathrm{f}_1 = \mathrm{f}_2$), such as the equilibrium state ($\mathrm{f}_i = \mathrm{f}_i^{\circ}$), there is no net flow of probability around a closed cycle of states, $\mathrm{S} = 0$. Therefore, momentum transfer from the drive layer to the drag layer arises because of the asymmetry of the electron distribution of one layer relative to the other layer.

3.2.3.3 S function

In the following paragraphs, it will be shown that S function in Equation 3.19 can be approximated by:

$$\mathrm{S}\left(\mathrm{f}_{\mathbf{k_1}}, \mathrm{f}_{\mathbf{k_2}}, \mathrm{f}_{\mathbf{k_1'}}, \mathrm{f}_{\mathbf{k_2'}}\right) \approx f^{\circ}_{\mathbf{k_1}} f^{\circ}_{\mathbf{k_2}} (1-f^{\circ}_{\mathbf{k_1}})(1-f^{\circ}_{\mathbf{k_1}})[\psi_{\mathbf{k_1'}} - \psi_{\mathbf{k_1}} + \psi_{\mathbf{k_2'}} - \psi_{\mathbf{k_2}}], \tag{3.20}$$

where ψ, a slowly varying function of energy, is a deviation function that describes how different the distribution function is from the equilibrium distribution, and f° is the equilibrium, Fermi-Dirac, distribution function.

First, we linearize the distribution function f with the assumption of weak interlayer scattering; the distribution function is not too much deviated from the equilibrium. From Equation 3.6, the following approximations can be derived:

$$f = f^{\circ} + \Delta f \approx f^{\circ} + \frac{\delta f^{\circ}}{\delta \varepsilon} \left(-k_B T \ \psi\left(\varepsilon\right)\right) = f^{\circ} + f^{\circ}\left(1-f^{\circ}\right)\psi\left(\varepsilon\right), \tag{3.21}$$

and similarly,

$$\frac{f}{1-f} \approx \frac{f^{\circ}}{1-f^{\circ}} + \frac{f^{\circ}}{1-f^{\circ}} \psi\left(\varepsilon\right). \tag{3.22}$$

Second, another equation useful to simplify S is obtained from the energy conservation:

$$\left(\frac{f^{\circ}_{\mathbf{k_1}}}{1-f^{\circ}_{\mathbf{k_1}}}\right)\left(\frac{f^{\circ}_{\mathbf{k_2}}}{1-f^{\circ}_{\mathbf{k_2}}}\right) = \left(\frac{f^{\circ}_{\mathbf{k_1'}}}{1-f^{\circ}_{\mathbf{k_1'}}}\right)\left(\frac{f^{\circ}_{\mathbf{k_2'}}}{1-f^{\circ}_{\mathbf{k_2'}}}\right). \tag{3.23}$$

Substituting Equations 3.21, 3.22 and 3.23 into the expression of S function, we can rearrange S as follows:

$$
\begin{aligned}
\mathrm{S}\left(\mathrm{f}_{\mathbf{k_1}}, \mathrm{f}_{\mathbf{k_2}}, \mathrm{f}_{\mathbf{k_1'}}, \mathrm{f}_{\mathbf{k_2'}}\right) &= \mathrm{f}_{\mathbf{k_1'}}\mathrm{f}_{\mathbf{k_2'}}\left(1-\mathrm{f}_{\mathbf{k_1}}\right)\left(1-\mathrm{f}_{\mathbf{k_2}}\right) - \mathrm{f}_{\mathbf{k_1}}\mathrm{f}_{\mathbf{k_2}}\left(1-\mathrm{f}_{\mathbf{k_1'}}\right)\left(1-\mathrm{f}_{\mathbf{k_2'}}\right) \\
&= \left(1-\mathrm{f}_{\mathbf{k_1}}\right)\left(1-\mathrm{f}_{\mathbf{k_2}}\right)\left(1-\mathrm{f}_{\mathbf{k_1'}}\right)\left(1-\mathrm{f}_{\mathbf{k_2'}}\right) \\
&\times \left[\left(\frac{f_{\mathbf{k_1'}}}{1-f_{\mathbf{k_1'}}}\right)\left(\frac{f_{\mathbf{k_2'}}}{1-f_{\mathbf{k_2'}}}\right) - \left(\frac{f_{\mathbf{k_1}}}{1-f_{\mathbf{k_1}}}\right)\left(\frac{f_{\mathbf{k_2}}}{1-f_{\mathbf{k_2}}}\right)\right] \\
&= \left(1-\mathrm{f}_{\mathbf{k_1}}\right)\left(1-\mathrm{f}_{\mathbf{k_2}}\right)\left(1-\mathrm{f}_{\mathbf{k_1'}}\right)\left(1-\mathrm{f}_{\mathbf{k_2'}}\right) \times \left(\frac{f^{\circ}_{\mathbf{k_1}}}{1-f^{\circ}_{\mathbf{k_1}}}\right)\left(\frac{f^{\circ}_{\mathbf{k_2}}}{1-f^{\circ}_{\mathbf{k_2}}}\right) \\
&\times \left[\left(1+\psi_{\mathbf{k_1'}}\right)\left(1+\psi_{\mathbf{k_2'}}\right) - \left(1+\psi_{\mathbf{k_1}}\right)\left(1+\psi_{\mathbf{k_2}}\right)\right].
\end{aligned}
$$

We may ignore the higher order terms of ψ because the deviation function assumed to be a small correction to the equilibrium distribution. Then we obtain the simplified result which is the same with Equation 3.20:

$$
\mathrm{S}\left(\mathbf{f}_{\mathbf{k_1}}, \mathbf{f}_{\mathbf{k_2}}, \mathbf{f}_{\mathbf{k_1'}}, \mathbf{f}_{\mathbf{k_2'}}\right) \approx f^{\circ}_{\mathbf{k_1}} f^{\circ}_{\mathbf{k_2}}\left(1-f^{\circ}_{\mathbf{k_1'}}\right)\left(1-f^{\circ}_{\mathbf{k_2'}}\right)\left[\psi_{\mathbf{k_1'}}-\psi_{\mathbf{k_1}}+\psi_{\mathbf{k_2'}}-\psi_{\mathbf{k_2}}\right].
$$

By substituting Equation 3.20 into Equation 3.19 and omitting the integration with $k_2^{'}$ due to the momentum conservation gives:

$$
\begin{aligned}
\left(\frac{\delta f(\mathbf{k_1})}{\delta t}\right)_{col} = \sum_{\sigma_{1'}\sigma_2\sigma_{2'}} \int \frac{d\mathbf{k_{1'}}}{(2\pi)^2} \int \frac{d\mathbf{k_2}}{(2\pi)^2} \Omega\left(\mathbf{k_1}, \mathbf{k_2} \rightarrow \mathbf{k_{1'}}, \mathbf{k_{2'}}\right) \\
\times f^{\circ}_{\mathbf{k_1}} f^{\circ}_{\mathbf{k_2}}\left(1-f^{\circ}_{\mathbf{k_1'}}\right)\left(1-f^{\circ}_{\mathbf{k_2'}}\right)\left[\psi_{\mathbf{k_1'}}-\psi_{\mathbf{k_1}}+\psi_{\mathbf{k_2'}}-\psi_{\mathbf{k_2}}\right] \\
\times \delta\left(\varepsilon_{\mathbf{k_1}}+\varepsilon_{\mathbf{k_2}}-\varepsilon_{\mathbf{k_1'}}-\varepsilon_{\mathbf{k_2'}}\right). \qquad (3.24)
\end{aligned}
$$

3.2.3.4 Deviation function

Now, we derive the explicit expression of the deviation function, ψ, using the relaxation time approximation. If we assume the dominant scattering mechanism is weak impurity scattering in the layer, not the interlayer electron-electron scattering, the distribution function of the drive layer is close to the equilibrium one, and we can use single layer Boltzmann equation to describe the dynamics of the drive layer in the relaxation time approximation:

$$\frac{\mathbf{F_2}}{\hbar}\frac{\delta f_{\mathbf{k_2}}}{\delta \mathbf{k_2}} = e\mathbf{E_2}\frac{1}{\hbar}\frac{\delta\varepsilon}{\delta \mathbf{k_2}}\frac{\delta f^{\circ}_{\mathbf{k_2}}}{\delta\varepsilon} = \mathrm{e}E_2\mathbf{v_2}\frac{\delta f^{\circ}_{\mathbf{k_2}}}{\delta\varepsilon} = \frac{\triangle f(\mathbf{k_2})}{\tau_2} \approx \frac{\frac{\delta f^{\circ}_{\mathbf{k_2}}}{\delta\varepsilon}\left(-k_BT\ \psi_{\mathbf{k_2}}\right)}{\tau_2},$$

where $E_2$is the electric field in the drive layer, directed along the x-axis, and τ_2 is an energy-independent momentum relaxation time, which determines the electron mobility, $\mu_2 = e\tau_2/m$. If we determine the direction of the current to be parallel to x-axis, then we can express the deviation function of the drive layer as:

$$\psi_{\mathbf{k_2}} = -\frac{1}{k_BT}\tau_2 \mathrm{e}v_{2x}E_2. \tag{3.25}$$

The drag layer's deviation function is zero because there is no current flow in the drag layer, and therefore the distribution function is the equilibrium one:

$$\psi_{\mathbf{k_1}} = 0,$$
$$f_{\mathbf{k_1}} = f^{\circ}_{\mathbf{k_1}}.$$

From the momentum conservation, we obtain:

$$v_{2\mathrm{x}}-v_{2'\mathrm{x}}=v_{1\mathrm{x}}-v_{1'\mathrm{x}}=\frac{\hbar}{m}\left(k_{1\mathrm{x}}-k_{1'\mathrm{x}}\right),$$

assuming the effective mass in both layers are identical. Now, further simplification can be made with:

$$\psi_{\mathbf{k_{1'}}}-\psi_{\mathbf{k_1}}+\psi_{\mathbf{k_{2'}}}-\psi_{\mathbf{k_2}}=\frac{\hbar\tau_2 \mathrm{e}E_2}{k_BT\ m}\left(k_{1'\mathrm{x}}-k_{1\mathrm{x}}\right). \tag{3.26}$$

Substituting Equation 3.26 into Equation 3.24 provides the following equation:

$$\begin{aligned}\left(\frac{\delta f(\mathbf{k_1})}{\delta t}\right)_{col}=&\frac{\hbar\tau_2 \mathrm{e}E_2}{k_BT\ m}\sum_{\sigma_{1'}\sigma_2\sigma_{2'}}\int\frac{d\mathbf{k_{1'}}}{(2\pi)^2}\int\frac{d\mathbf{k_2}}{(2\pi)^2}\Omega\left(\mathbf{k_1},\mathbf{k_2}\rightarrow\mathbf{k_{1'}},\mathbf{k_{2'}}\right)\\&\times f^{\circ}_{\mathbf{k_1}}f^{\circ}_{\mathbf{k_2}}\left(1-f^{\circ}_{\mathbf{k_{1'}}}\right)\left(1-f^{\circ}_{\mathbf{k_{2'}}}\right)\left(k_{1'\mathrm{x}}-k_{1\mathrm{x}}\right)\\&\times\delta\left(\varepsilon_{\mathbf{k_1}}+\varepsilon_{\mathbf{k_2}}-\varepsilon_{\mathbf{k_{1'}}}-\varepsilon_{\mathbf{k_{2'}}}\right).\end{aligned} \tag{3.27}$$

3.2.4 Coulomb drag resistivity

Now, we can substitute Equation 3.27 into Equation 3.15 to have:

$$\begin{aligned}\rho_{drag}=&\frac{\hbar}{\sigma_2E_2n_1e}\sum_{\sigma_1}\int\frac{d\mathbf{k_1}}{(2\pi)^2}k_{1x}\left(\frac{\delta f_{\mathbf{k_1}}}{\delta t}\right)_{col}\\=&\frac{\hbar}{\sigma_2E_2n_1e}\frac{e\hbar^2E_2\tau_2}{4mk_BT}\sum_{\sigma_1\sigma_{1'}\sigma_2\sigma_{2'}}\int\frac{d\mathbf{k_1}}{(2\pi)^2}\int\frac{d\mathbf{k_{1'}}}{(2\pi)^2}\int\frac{d\mathbf{k_2}}{(2\pi)^2}\Omega\left(\mathbf{k_1},\mathbf{k_2}\rightarrow\mathbf{k_{1'}},\mathbf{k_{2'}}\right)\\&\times f^{\circ}_{\mathbf{k_1}}f^{\circ}_{\mathbf{k_2}}\left(1-f^{\circ}_{\mathbf{k_{1'}}}\right)\left(1-f^{\circ}_{\mathbf{k_{2'}}}\right)\times k_{1x}\left(k_{1'\mathrm{x}}-k_{1\mathrm{x}}\right)\times\delta\left(\varepsilon_{\mathbf{k_1}}+\varepsilon_{\mathbf{k_2}}-\varepsilon_{\mathbf{k_{1'}}}-\varepsilon_{\mathbf{k_{2'}}}\right).\end{aligned}$$

We can simplify the equations in the following manner. First, the spin summation provides a factor of 4, not 16, because the spin state in each layer must be the same. Second, the symmetry of the integrand with respect to the interchange of $\mathbf{k}_1$ and $\mathbf{k}_{1'}$and the independence of the relaxation rate on the direction of electric field either along the x- or y-axis provides another equality:

$$k_{1x}\left(k_{1'\mathrm{x}}-k_{1\mathrm{x}}\right)=k_{1'x}\left(k_{1\mathrm{x}}-k_{1'\mathrm{x}}\right)=-\frac{1}{2}(k_{1'\mathrm{x}}-k_{1\mathrm{x}})^2\equiv=-\frac{1}{4}(\mathbf{k_{1'}}-\mathbf{k_1})^2=-\frac{\mathbf{q^2}}{4},$$

where $\mathbf{q}=\mathbf{k_{1'}}-\mathbf{k_1}=\mathbf{k_2}-\mathbf{k_{2'}}$ is the transferred momentum for the particle in the drive layer to one in the drag layer. Third, if we assume that the scattering amplitude, Ω, depends only on the transferred momentum $\mathbf{q}$ and not on the specific momentum values of $\mathbf{k}_1$,$\mathbf{k}_{1'}$, $\mathbf{k}_2$ and $\mathbf{k}_{2'}$, then the integral over $\mathbf{k}_{1'}$ can be replaced by an integral over $\mathbf{q}$:

$$\begin{aligned}\rho_{drag}=&-\frac{\hbar}{\sigma_2 E_2 n_1 e}\frac{e\hbar^2 E_2\tau_2}{4mk_BT}\int\frac{d\mathbf{q}}{(2\pi)^2}\int\frac{d\mathbf{k_{1'}}}{(2\pi)^2}\int\frac{d\mathbf{k_2}}{(2\pi)^2}\Omega\left(\mathbf{q}\right)\mathbf{q}^2\\&\times f^{\circ}_{\mathbf{k_1}}f^{\circ}_{\mathbf{k_2}}\left(1-f^{\circ}_{\mathbf{k_1+q}}\right)\left(1-f^{\circ}_{\mathbf{k_{2'}-q}}\right)\\&\times\delta(\varepsilon_{\mathbf{k_1}}+\varepsilon_{\mathbf{k_2}}-\varepsilon_{\mathbf{k_1+q}}-\varepsilon_{\mathbf{k_2-q}}).\end{aligned}\tag{3.28}$$

Further simplification of the expression is possible using the following three identities:

$$\delta\left(\varepsilon_{\mathbf{k_1}}+\varepsilon_{\mathbf{k_2}}-\varepsilon_{\mathbf{k_1+q}}-\varepsilon_{\mathbf{k_{2'}-q}}\right)=\hbar\int_{-\infty}^{\infty}d\omega\ \delta\left(\varepsilon_{\mathbf{k_1}}-\varepsilon_{\mathbf{k_1+q}}-\hbar\omega\right)\delta\left(\varepsilon_{\mathbf{k_2}}-\varepsilon_{\mathbf{k_2-q}}+\hbar\omega\right),$$

$$f^{\circ}\left(\varepsilon\right)\left[1-f^{\circ}\left(\varepsilon+\hbar\omega\right)\right]=\frac{f^{\circ}\left(\varepsilon\right)-f^{\circ}\left(\varepsilon+\hbar\omega\right)}{1-\exp\left(-\frac{\hbar\omega}{k_BT}\right)},$$

$$\left[1-\exp\left(-\frac{\hbar\omega}{k_BT}\right)\right]\left[1-\exp\left(\frac{\hbar\omega}{k_BT}\right)\right]=-4\sinh^2\left(\frac{\hbar\omega}{2k_BT}\right).$$

After substituting the three identities, the Coulomb drag expression becomes:

$$\begin{aligned}\rho_{drag}=-\frac{\hbar}{\sigma_2E_2n_1e}\frac{e\hbar^3E_2\tau_2}{4mk_BT}\int\frac{d\mathbf{q}}{\left(2\pi\right)^2}\Omega\left(\mathbf{q}\right)\mathbf{q}^2\int d\omega\frac{1}{\sinh^2\left(\frac{\hbar\omega}{2k_BT}\right)}\\ \times\left[\int\frac{d\mathbf{k_1}}{\left(2\pi\right)^2}(f^{\circ}_{\mathbf{k_1}}-f^{\circ}_{\mathbf{k_1+q}})\delta\left(\hbar\omega-\varepsilon_{\mathbf{k_1}}+\varepsilon_{\mathbf{k_1+q}}\right)\right]\\ \times\left[\int\frac{d\mathbf{k_2}}{\left(2\pi\right)^2}(f^{\circ}_{\mathbf{k_2}}-f^{\circ}_{\mathbf{k_2-q}})\delta\left(\hbar\omega+\varepsilon_{\mathbf{k_2}}-\varepsilon_{\mathbf{k_2-q}}\right)\right].\end{aligned}\tag{3.29}$$

It is convenient to express Equation 3.29 in terms of the two-dimensional susceptibility function $\chi_{\mathbf{k_1}}(\mathbf{q},\omega)$ defined by:

$$\chi_{\mathbf{k_1}}\left(\mathbf{q},\ \omega\right)=-\int\frac{d\mathbf{k_1}}{\left(2\pi\right)^2}\frac{f^{\circ}_{\mathbf{k_1}}-f^{\circ}_{\mathbf{k_{1'}}}}{\varepsilon_{\mathbf{k_1}}-\varepsilon_{\mathbf{k_{1'}}}+\hbar\omega+\mathrm{i}\delta}.$$

Using the above equation, it can be shown that:

$$\int\frac{d\mathbf{k_1}}{\left(2\pi\right)^2}\left(f^{\circ}_{\mathbf{k_1}}-f^{\circ}_{\mathbf{k_1+q}}\right)\delta\left(\hbar\omega-\varepsilon_{\mathbf{k_1}}+\varepsilon_{\mathbf{k_1+q}}\right)=\frac{1}{\pi}\mathrm{Im}\chi_{\mathbf{k_1}}\left(\mathbf{q},\ \omega\right),$$

and

$$\int \frac{d\mathbf{k_2}}{(2\pi)^2}\left(f^{\circ}_{\mathbf{k_2}}-f^{\circ}_{\mathbf{k_2-q}}\right)\delta\left(\hbar\omega+\varepsilon_{\mathbf{k_2}}-\varepsilon_{\mathbf{k_2-q}}\right)=-\frac{1}{\pi}\mathrm{Im}\chi_{\mathbf{k_2}}\left(\mathbf{q},\ \omega\right).$$

Substituting these results into Equation 3.29 and observing the integrand is an even function of ω, we finally obtain the general formula of Coulomb drag resistivity:

$$\rho_{drag}=-\frac{\hbar^3}{2\pi^2e^2k_BT}\frac{1}{n_1n_2}\int\frac{d\mathbf{q}}{(2\pi)^2}\Omega\left(\mathbf{q}\right)\ \mathbf{q}^2\int d\omega\frac{\mathrm{Im}\chi_{\mathbf{k_1}}\left(\mathbf{q},\ \omega\right)\ \mathrm{Im}\chi_{\mathbf{k_2}}\left(\mathbf{q},\ \omega\right)}{\sinh^2\left(\frac{\hbar\omega}{2k_BT}\right)}. \tag{3.30}$$

The different terms in this equation can be interpreted as following: (1) $\mathbf{q}^2$ – momentum transfer between the layers; (2) $\Omega\left(\mathbf{q}\right)$ – the effective interaction; and (3) $\int d\omega\frac{\mathrm{Im}\chi_{\mathbf{k_1}}(\mathbf{q},\ \omega)\ \mathrm{Im}\chi_{\mathbf{k_2}}(\mathbf{q},\ \omega)}{\sinh^2\left(\frac{\hbar\omega}{2k_BT}\right)}$ – phase-space.

3.2.5 Analytical formula for weak-coupling limit

In most cases, Equation 3.30 needs to be evaluated numerically. To obtain further insight of the Coulomb drag phenomenon, we follow Jauho *et al.* [51] and extract an analytical result for sufficiently low temperatures ($T \ll T_F$) and small momentum transfer cases ($q \ll k_F$) via the following approaches: (1) Imχ is approximated by its low frequency expansion; (2) the interaction potential was determined from Poisson's equation for a point source situated in one of the two layers and screened by both layers; (3) the static screening of this potential is treated in the Thomas-Fermi approximation, which assumes momentum transfer wave vectors $\mathbf{q}$ will be less than the Thomas-Fermi screening wave vector q_{TF} appropriate to two-dimensions.

$$\mathrm{Im}\chi\left(\mathbf{q},\omega\right)\approx\frac{m^2}{2\pi\hbar^3k_F}\frac{\omega}{q},\mathrm{when T}\ll\mathrm{T_F},$$

If the two layers assumed to be identical, then we can perform the integration.

$$\frac{1}{k_BT}\int_0^\infty d\omega\frac{\left[\mathrm{Im}\chi_{\mathbf{k_2}}\left(\mathbf{q},\ \omega\right)\right]^2}{\sinh^2\left(\frac{\hbar\omega}{2k_BT}\right)}=\frac{\left(k_BT\right)^2m^4}{3\hbar^9k_F^2}\frac{1}{q^2}.$$

It is the result of this integral which provides the dominant temperature dependence of Coulomb drag, $\rho_{drag}\propto T^2$. The scattering probability is obtained from the effective interaction by use of the Born approximation, or equivalently the golden rule:

$$\Omega\left(\mathrm{q}\right)=\frac{2\pi}{\hbar}|e\phi\left(q\right)|^2,$$

where $e\phi\left(q\right)$ is the Fourier component of the screened Coulomb interaction between the layers. $e\phi\left(q\right)$ for two-dimensional electron gas with a finite thickness is derived in [51]. Since a graphene sheet can be assumed as a zero-thickness mathematical plane, $e\phi\left(q\right)$ for graphene double layers reduces to that of the screened Coulomb interaction between charge densities localized at the two quantum wells of zero thickness:

$$e\phi\left(q\right)=\frac{2\pi e^2}{\kappa}\frac{q}{2q_{TF}^2\sinh qd\ +\left(2q\ q_{TF}+q^2\right)\exp qd},$$

where κ is the dielectric constant and q_{TF} is the Thomas-Fermi screening wavevector. Here we assume the identical dielectric medium surrounds the two electron layers for simplicity; we refer to [56] for the case with different dielectric mediums. When q is comparable to or smaller than d^{-1}, we may neglect the second term in the denominator and the equation further simplifies into:

$$e\phi\left(q\right)\approx\frac{\pi e^{2}}{\kappa}\frac{q}{q_{TF}^{2}\sinh qd}.$$

Then the remaining integration becomes:

$$\int_{0}^{\infty}dq\ q|e\phi\left(q\right)|^{2}=\frac{3\pi^{2}e^{4}}{2\kappa^{2}}\frac{1}{q_{TF}^{2}}\frac{1}{d^{4}}\zeta\left(3\right),$$

where q_{TF} is the Thomas-Fermi screening wavevector, ζ is the Riemann zeta function and $\zeta(3)\cong 1.2$. Therefore, the final drag resistivity, ρ_{drag}, can be expressed as

$$\rho_{drag}=-\frac{h\pi\zeta(3)(k_{B}T)^{2}}{32\ {E_{F}}^{2}(q_{TF}d)^{2}\ (k_{F}d)^{2}}. \tag{3.31}$$

Again, this analytical result is valid for sufficiently low temperatures ($T\ll T_{F}$) and small momentum transfers ($q\ll k_{F}$).

	E_F	$D(E)$	$D_0=D(E_F)$	k_{F}	q_{TF}
MLG	$\hbar v_F\sqrt{\frac{4\pi n}{g_s g_v}}$	$\frac{g_s g_v E}{2\pi(\hbar v_F)^2}$	$\frac{\sqrt{g_s g_v n}}{\sqrt{\pi}\hbar v_F}$	$\sqrt{\frac{4\pi n}{g_s g_v}}$	$\frac{\sqrt{g_s g_v \pi n}e^2}{2\epsilon\pi\hbar v_F}$
BLG and 2DEG	$\frac{2\pi\hbar^2 n}{m^* g_s g_v}$	$\frac{g_s g_v m^*}{2\pi\hbar^2}$	$\frac{g_s g_v m^*}{2\pi\hbar^2}$	$\sqrt{\frac{4\pi n}{g_s g_v}}$	$\frac{g_s g_v m^* e^2}{4\pi\epsilon\hbar^2}$

Table 3.1: Elementary electronic quantities in monolayer graphene (MLG), bilayer graphene (BLG) and two-dimensional electron gas (2DEG). E_F, $D(E)$, k_{F} and q_{TF} represent the Fermi energy, density of states, Fermi wavevector and Thomas-Fermi screening wavevector, respectively. $D_0=D(E_F)$ is the density of states at the Fermi energy, and ϵ is the dielectric permittivity. All quantities are in SI unit. Expressions in cgs unit can be found in Ref.[1].

3.2.6 Analytical formula for drag in graphene

While the nonlinear susceptibility for graphene is quite different from that for a regular two-dimensional electron gas, we can show that the analytical expression of drag resistivity calculated for the regular two-dimensional electron gas in Equation 3.31, which is valid for low temperatures $T \ll T_F = \varepsilon_F/k_B$ and high density and/or large interlayer separation $k_F d \gg 1$, has the same form with the drag in graphene in the same regime. Using Table 3.2.6 [57], we can substitute the appropriate quantities into Equation 3.31 and obtain the drag resistivity in single layer graphene as a function of d, $n_{B,T}$ and T:

$$\rho_{drag} = -\frac{h\zeta\,(3)\,\epsilon^2}{32\ \mathrm{e}^6}\frac{1}{d^4}\frac{(k_B T)^2}{n_B^{3/2} n_T^{3/2}}, \tag{3.32}$$

where ϵ is the dielectric permittivity. This analytical expression is useful because the strong inverse dependence on d and the symmetry under layer interchange are clearly identified, and it also predicts clear dependence of ρ_{drag} on temperature, density and layer separation. We will use this result to compare our experimental measurements in the following chapters.

3.3 Coulomb Drag Measurement in Graphene Double Layers

Coulomb drag measurements provide key insight into the physics of the graphene double layer system [48, 49]. A current (I_{drive}) flown in one (drive) layer leads to a momentum transfer between the two layers, thanks to the interlayer electron-electron interaction. To counter this momentum transfer, a longitudinal voltage (V_{drag}) builds

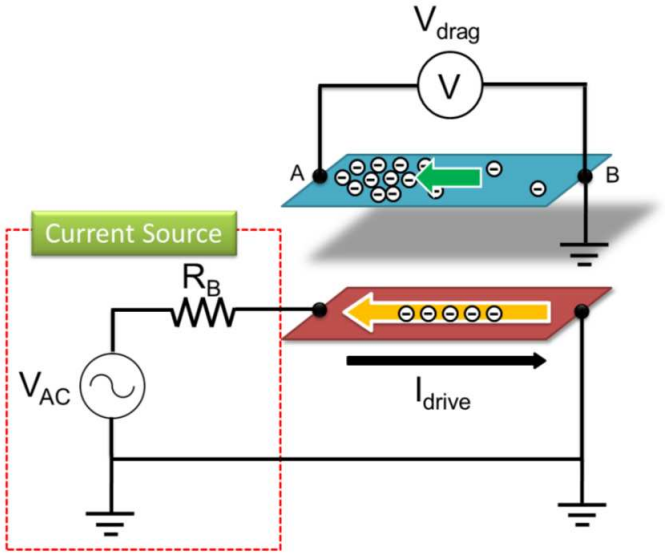

Figure 3.3: Drag voltage measurement setup. Low frequency AC voltage from lock-in amplifier and a large ballast resistor, R_B, are connected to form a current source. The drag voltage is measured in the passive (drag) layer, which can be grounded either at contact A or B. The carriers in both layers are exemplified to be electrons.

up in the opposite (drag) layer [Figure 3.3]. The polarity of V_{drag} depends on the carrier type in the two layers and is opposite (same) polarity as the voltage drop in the drive layer when both layers have the same (opposite) type of carriers. The drag resistivity is defined as $\rho_{drag} = (W/L)V_{drag}/I_{drive}$, where L and W are the length and width of the region where drag occurs.

3.3.1 Coulomb drag measurement setup

Now we focus on the drag measurement setup as illustrated in Figure 3.3. We take low-frequency AC voltage from a lock-in amplifier and connect it to a large ballast resistor R_B which makes the combination as a constant current source. By connecting the resistance of interest at one terminal of the ballast resistor and grounding the other

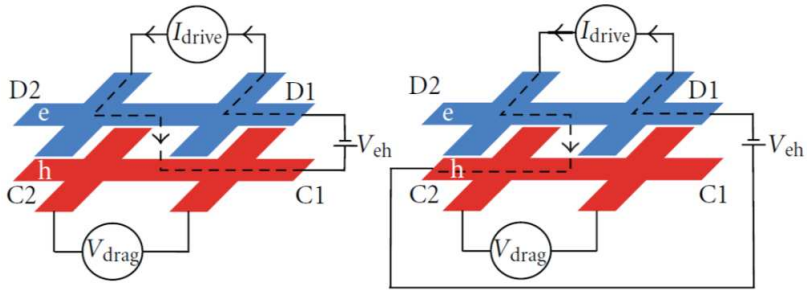

Figure 3.4: Drag consistency check to detect interlayer leakage current. If there is a leakage path, the sign reversal in the drag signal occurs when the grounding terminal in the drag layer is swapped, for example from C1 (left panel) to C2 (right panel). Adapted from [6].

terminal, we can supply a constant drive current, I_{drive}, through the drive layer. We probe the drag voltage, V_{drag}, in the drag layer using the preamplifier in the lock-in amplifier. In most measurements, we use 1 V AC voltage with the frequency of 7 - 17 Hz and a 10 MΩ ballast resistor to supply 100 nA drive current. Since the maximum resistivity value of high quality graphene single layers is in a few kΩ range, and the actual layer resistance, which depends on the device dimension, is also lower than a few tens of kΩ, the constant current supply is ensured regardless the layer resistivity change in the drive layer.

3.3.2 Consistency check

The consistency check of the drag signal is necessary to confirm if the measured voltage drop in the drag layer originates from the electron-electron scattering between the layers or from any other spurious mechanisms such as interlayer leakage current. If the drive current leaks between the layers, a finite voltage due to current flow in the drag layer will be measured in addition to the Coulomb drag voltage, preventing

an accurate drag resistivity measurement.

To check the presence of leakage currents, we alter the grounding points in the drag layer, for example from C1 (left panel) to C2 (right panel) in Figure 3.4, and compare the voltage drops between the two measurements. While the voltage drop generated by the Coulomb drag, V_{drag}, will not change its sign because it is determined by the carrier type and direction of the drive current, any voltage drop in the drag layer induced by leakage current (from the drive layer to the drag layer due to direct leakage, tunneling and/or capacitive coupling) will change the sign depending on the position of the grounding points. Therefore, the measured voltage drop when the contact C1 (C2) in the drag layer is grounded, $V_{measured,C1(C2)}$, can be expressed as:

$$V_{measured,C1} = V_{drag} + V_{leakage},$$
$$V_{measured,C2} = V_{drag} - V_{leakage}.$$

Thus, by shifting the point at which the drag layer is voltage-referenced, we can verify if the measured voltage was affected by leakage profile in the system or not. An example of the consistency check performed in BiSFET2 is shown in Figure 3.5. The drag resistances measured as a function of V_{BG} at combinations of different drive current directions, V_{BG} sweep directions and grounding configurations are overlapped well to each other, indicating that there is little leakage current measured with the drag signal.

If ρ_{drag} values measured at different grounding configurations are different,

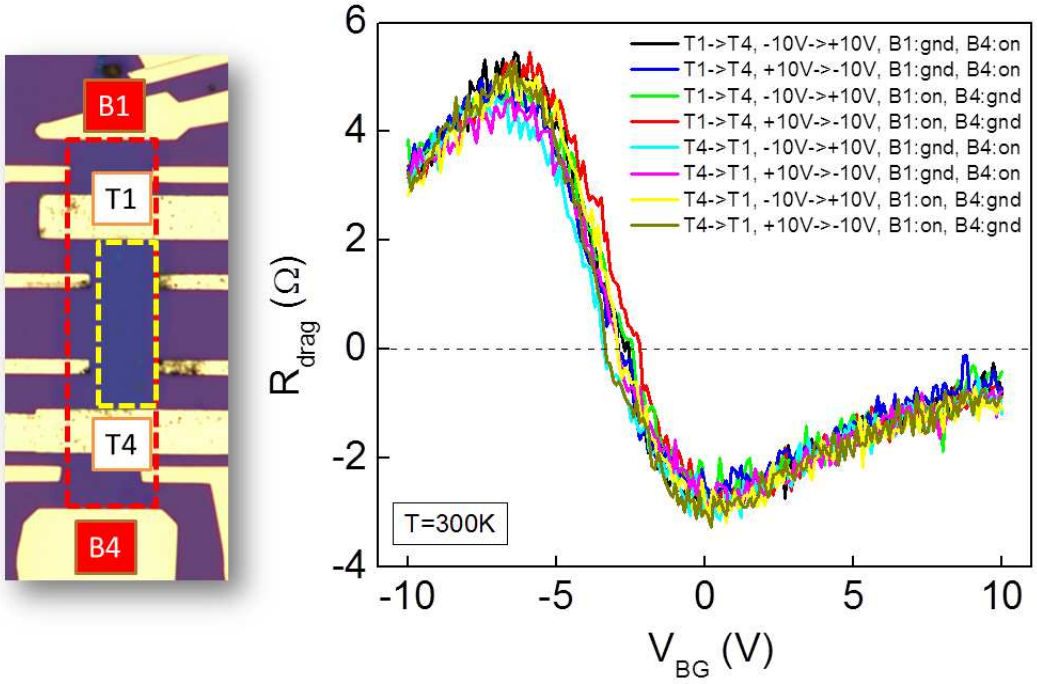

Figure 3.5: Optical micrograph of BiSFET2 (left). The top layer (yellow dashed line) is 24 μm long and 7.5 μm wide and the bottom layer (red dashed line) is 51 μm long and 14 μm wide. Coulomb drag resistances vs V_{BG} measured at T = 300 K and at different measurement configurations are shown in the right panel. Various consistency checks, such as swapping reference points in the drag layer, changing V_{BG} sweep directions and altering drive current directions, are performed to ensure the validity of the Coulomb drag signal.

then we can even out the contribution of the interlayer leakage in V_{drag} by averaging different measurements:

$$V_{drag,avg} = (V_{measured,C1} + V_{measured,C2})/2. \tag{3.33}$$

The assumption in Equation 3.33 is that the spurious component changes its sign but not the magnitude as the grounding configuration changes. One must understand that the pure drag component in V_{drag} cannot be recovered by Equation 3.33 unless the leakage/tunneling paths are symmetrically positioned between the voltage probes. Since it is very difficult to analyze the exact interlayer leakage profile in practical devices, we abandon the devices with significant inconsistency observed during the consistency check. Instead, we use Equation 3.33 to verify the accuracy of the drag measurement and obtain an error bar. The example of the inconsistent ρ_{drag} measurements with different ground points and averaged value is shown in Figure 3.6.

The consistency check is performed each and every time we measure the Coulomb drag. Separate DC leakage current measurements are performed for all the samples, confirming us the graphene double layer samples we explore show the interlayer resistance larger than 1 GΩ regardless the device dimensions and applied biases.

3.3.3 Coulomb drag in graphene double layers

Now we are ready to analyze our Coulomb drag data. After standard consistency checks, the drag resistivity ρ_{drag} along with the layer resistivities ρ_T and ρ_B vs

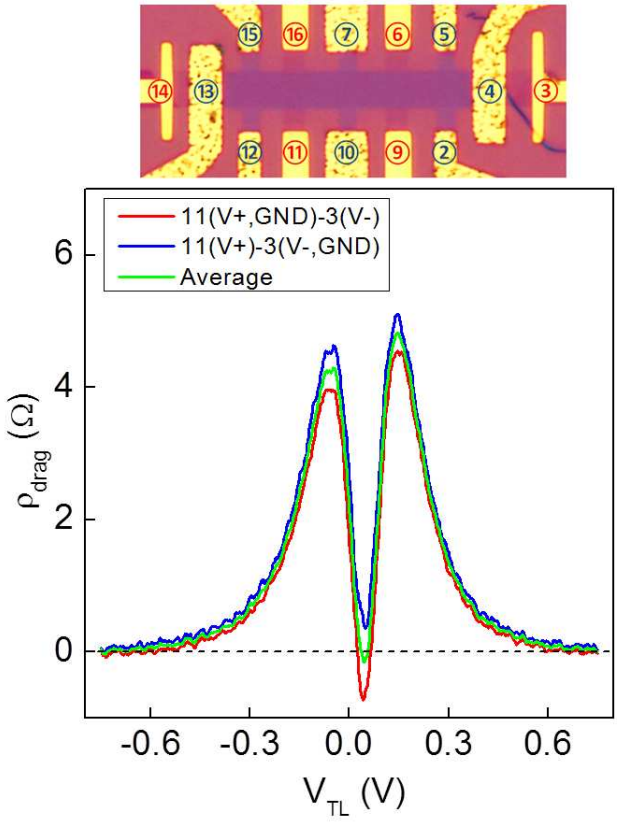

Figure 3.6: Top: contact numbering marked on the optical micrograph of BiSFET12. Red (blue) numbers indicate bottom (top) layer contacts. Bottom: ρ_{drag}vs top layer bias, V_{TL}, measured with different grounding configurations at T = 0.4 K in BiSFET12. 100 nA drive current flows from contact 10 to contact 5 in the top layer, and the voltage drop in drag layer is measured between contact 11 and 3.

V_{BG} measured at T = 250 K in BiSFET6 is shown in Figure 3.7. The charge neutrality (Dirac) points of both layers are captured in the experimentally accessible V_{BG} window in this device. Consequently, depending on the V_{BG} value, we can probe the Coulomb drag at three different regimes: a hole-hole double layer for $V_{BG} < -15V$, an electron-hole double layer for $-15V < V_{BG} < 2V$, and an electron-electron double layer for $V_{BG} > 2V$. The dependence of ρ_B and ρ_T on V_{BG} shown is also in good agreement with the model presented in Figure 2.14, which also provided the estimated layer densities marked in Figure 3.7.

Consistent with the above argument on the carrier type dependence of the sign of Coulomb drag, ρ_{drag} is positive in the electron-hole double layer regime, negative in the hole-hole or electron-electron regime, and changes sign when either the top or the bottom layer are at the charge neutrality point. The amplitude of ρ_{drag} is maximum near the charge neutrality point at the bottom layer both positive and negative cases, and decreases as layer density of the bottom layer increases. This observation can be explained based on our derivation of Equation 3.32 in Chapter 3.2,

$$\rho_{drag} = -\frac{h\zeta(3)\,\epsilon^2}{32\ \mathrm{e}^6}\frac{1}{d^4}\frac{(k_B T)^2}{n_B^{3/2} n_T^{3/2}}.$$

For two closely spaced graphene layers when the ground state of each layer is a Fermi liquid, ρ_{drag} depends on each layer's density as $\propto 1/n^{3/2}$, on temperature as $\propto T^2$, and interlayer distance as $\propto 1/d^4$ at weak coupling limit, $k_F d \ll 1$. Let us study temperature and density dependence of ρ_{drag} in more detail.

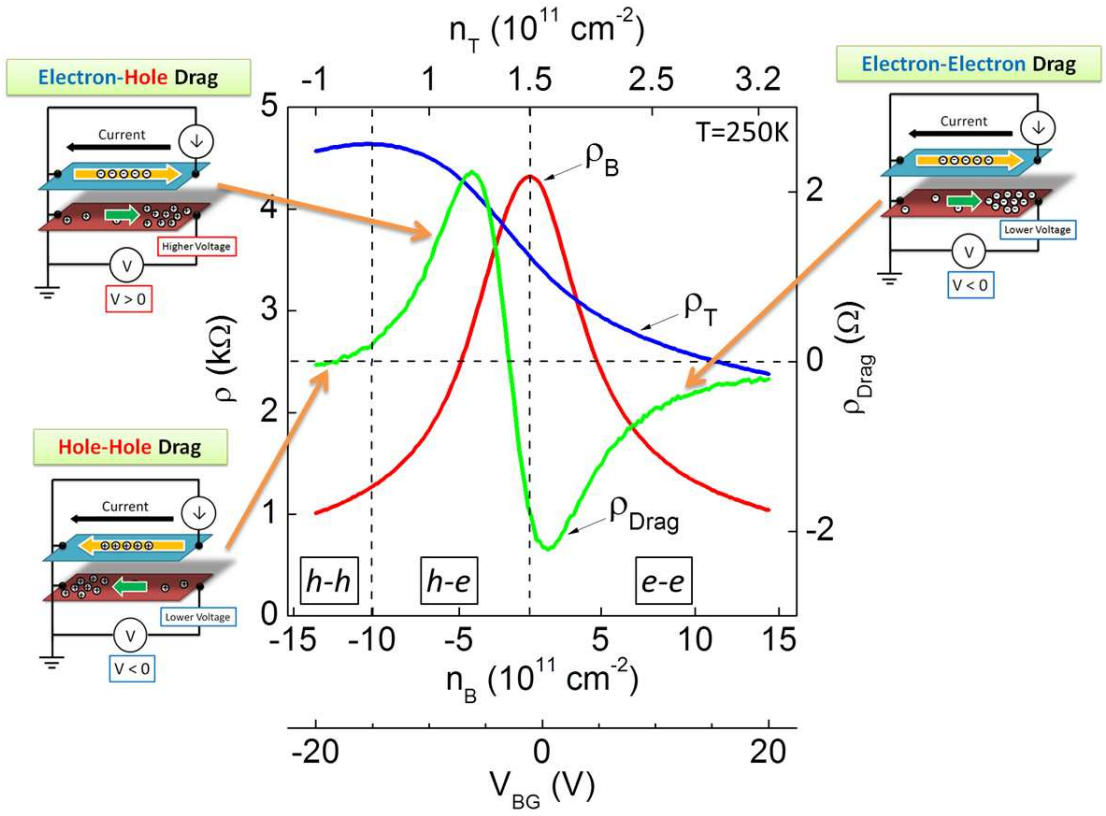

Figure 3.7: Coulomb drag in graphene. Layer resistivities ($\rho_{B,T}$) and ρ_{drag} vs layer densities ($n_{B,T}$) and V_{BG} for BiSFET6 measured at T = 250K. We have three different regimes: hole-hole, hole-electron and electron-electron, which show the corresponding signs of ρ_{drag}. Adapted from Ref.[3].

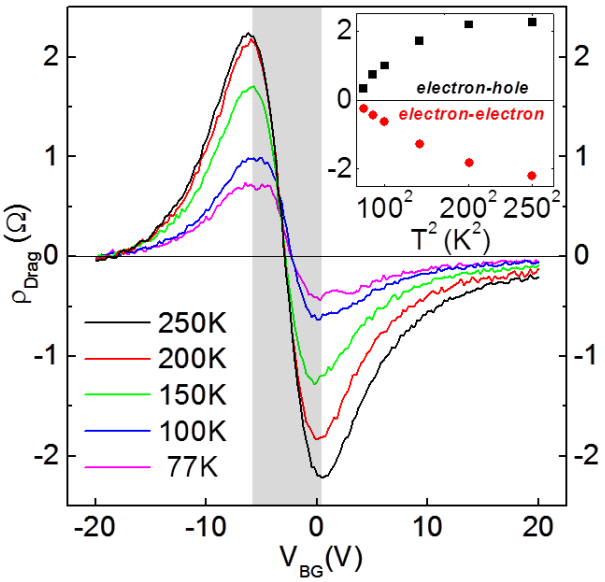

Figure 3.8: Temperature dependence of Coulomb drag in graphene. ρ_{drag} vs V_{BG} at different T values, from 250 to 77 K. The inset shows the maximum ρ_{drag} values vs T^2 in the electron-hole and electron-hole regimes. Adapted from Ref.[3].

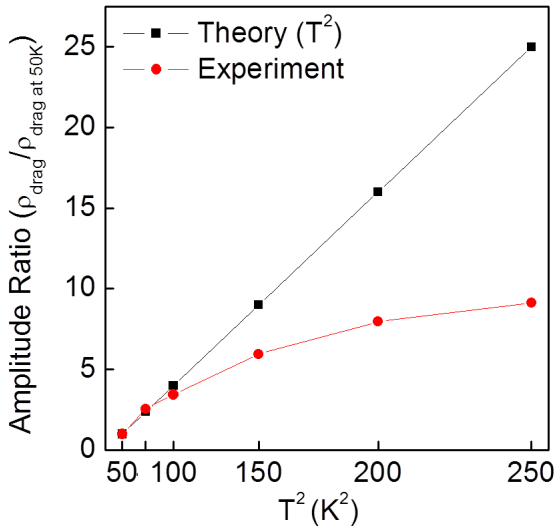

Figure 3.9: Relative Coulomb drag amplitude vs T^2 in BiSFET6. The black line represents theoretical T^2 dependence, and the red line represents the experimentally determined ratio. The x-axis is labeled by corresponding temperature.

3.3.3.1 Temperature dependence of drag resistivity

Figure 3.8 data show ρ_{drag} vs V_{BG} measured for BiSFET6 for T values between 77 and 250 K. The $\rho_{drag} \propto (k_B T)^2$ dependence, which stems from Pauli's exclusion principle, restricts the phase space where electron-electron scattering can occur. The T^2 dependence describes the available phase space for electrons to be scattered into, which in turn is dependent on the broadening of the Fermi distribution function in each layer. At zero temperature the electrons in a conductor will occupy energy states up to the Fermi level E_F, and the states with $E > E_F$ remain vacant. Therefore, ρ_{drag} will be zero at T = 0 K. As temperature increases, the distribution of occupied states changes in accordance with the Fermi-Dirac distribution function and the state occupancy fluctuates greatly near E_F, making ideal conditions for scattering to occur: the process requires occupied states and empty states on the order of k_BT from each other. The occupied states provide the electrons initially needed to participate in the scattering event while the empty states provide somewhere for these electrons to eventually scatter into.

The maximum absolute value of ρ_{drag} at each temperature is plotted in the inset of Figure 3.8. At temperatures between 70 and 100 K, the T^2 dependence is followed closely and softens for $T > 100K$ for both electron-hole drag and electron-electron drag. To further verify the temperature dependence, we define an error function,

$$\text{error(c, d)} = \sum_{V_{BG}} \left(\rho_{drag,ref}[V_{BG}] - c \times \rho_{drag}[V_{BG} - d]\right)^2, \tag{3.34}$$

and find an relative amplitude ratio, c, and V_{BG} offset, d, which minimize the error. The c value obtained from the fitting indicates the relative ratio of drag amplitude increase to the reference drag signal as we raise the sample temperature. The result shown in Figure 3.9 clearly shows that T^2 dependence matches well at temperatures below 100K, and becomes significantly weakened as temperature further increases. The temperature dependence of Coulomb drag at temperatures lower than 50 K is difficult to probe due to mesoscopic fluctuations which develops at low temperatures. We will discuss the Coulomb drag fluctuations in graphene double layers further in Section 3.3.4.

3.3.3.2 Density dependence of drag resistivity

Figure 3.7 data show that the magnitude of ρ_{drag} decreases with increasing n_B and n_T. However, it is difficult to study the density dependence of ρ_{drag} here because both n_B and n_T are changing simultaneously as V_{BG} changes. We achieved the independent control of n_B and n_T by applying an interlayer bias to the top layer and using it as a top-gate to control layer densities in the two layers as discussed in Chapter 2.4. Figure 3.10 shows ρ_{drag} plotted in the plane of n_T and n_B at different temperatures using the interlayer bias technique. We extract the ρ_{drag} cuts along the line where the two layers have equal density of carriers, $n_T = n_B$, and present the results in Figure 3.11.

We check the power law dependence of ρ_{drag} on layer densities, $\rho_{drag} \propto n_B^{\alpha}\, n_T^{\alpha}$, predicted in the Boltzmann transport theory of Coulomb drag in Figure 3.11, where we show $|\rho_{drag}|$ vs $|n_T|$ in a log-log plot. The linear dependence of ρ_{drag} on layer density

at high density limit both in electron-electron and hole-hole drag clearly confirms the power law dependence. The exponent we extract by linear fitting is $\alpha = -0.9 \pm 0.1$ which is larger than the expected value, $\alpha = -1.5$ in Equation 3.32, and depends little on temperature. A possible explanation for this discrepancy is that Equation 3.32 is valid for high densities and/or large interlayer spacing such that $k_F \cdot d \gg 1$; for Figure 3.11 data, $k_F \cdot d \leq 1$ ($k_F \cdot d \cong 1$ at n = 5×10^{11} cm^{-2}) at all layer densities and $k_F \cdot d$ is equal to or smaller than 3 ($k_F \cdot d \cong 3$ at n = 5×10^{12} cm^{-2}) in all measurements we performed. Carrega *et al.* [58] reviewed recent theory works on Coulomb drag in graphene [5, 56, 57, 59, 60] and suggested the density exponent of $\alpha = -1.5$ in the weak coupling limit, $k_F \cdot d \gg 1$ and $\alpha = -0.5$ in the strong coupling limit, $k_F \cdot d \ll 1$. Our measurement is performed in neither of limits; we are in the regime between the two different limits, and, therefore, the exponent presumably lies in between -0.5 and -1.5. The discrepancy in the drag magnitude, which is $\sim 10^2$ times lower than the value Equation 3.32, may be explained by the similar argument. Further theoretical work and numerical calculation will be needed to clearly explain these discrepancies.

3.3.3.3 Drag resistivity at zero layer density

Figure 3.8 data show a smooth crossover for ρ_{drag} through 0, from the electron-hole to the electron-electron regime [blue (shaded) corridor], and Figure 3.10 data also show zero drag points when the carriers change from electron-electron to hole-hole. The zero drag resistivity measured at the charge neutrality point of either drive or drag layer results from the electron-hole symmetry at $\varepsilon_F = 0$; (1) if the drive layer is at the charge neutrality point, the thermally generated electrons and holes, which

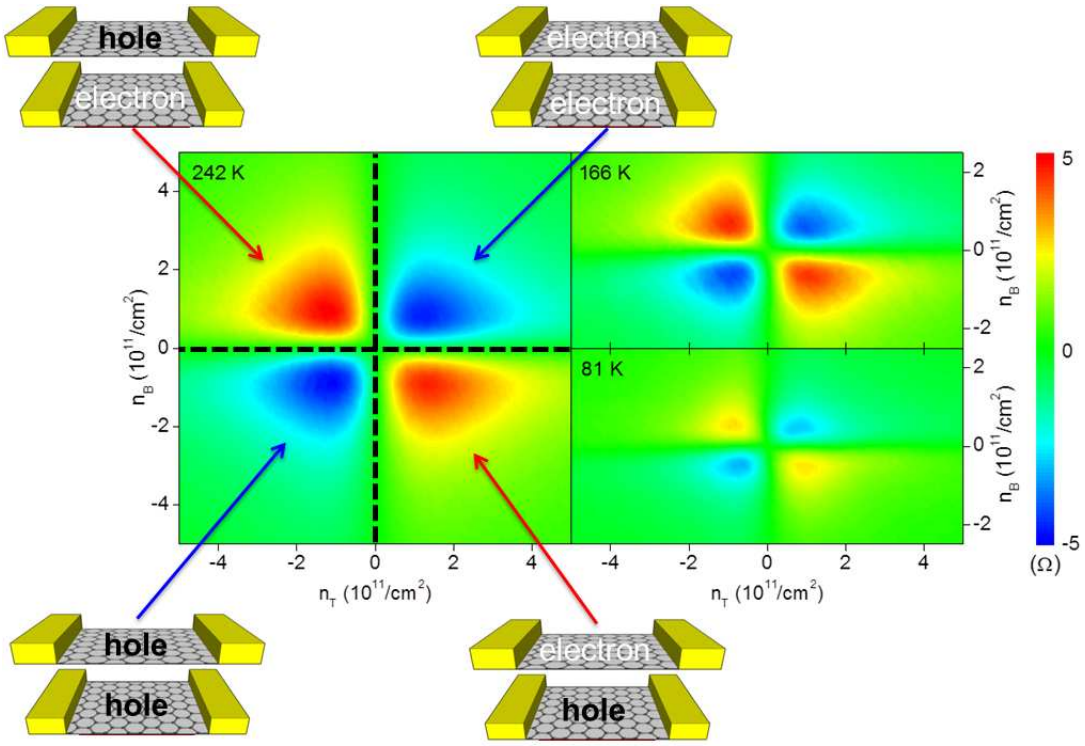

Figure 3.10: Contour plots of ρ_{drag} measured as a function of n_T and n_B at T = 242 K (left), 166 K (top right) and 81 K (bottom right) in BiSFET12.

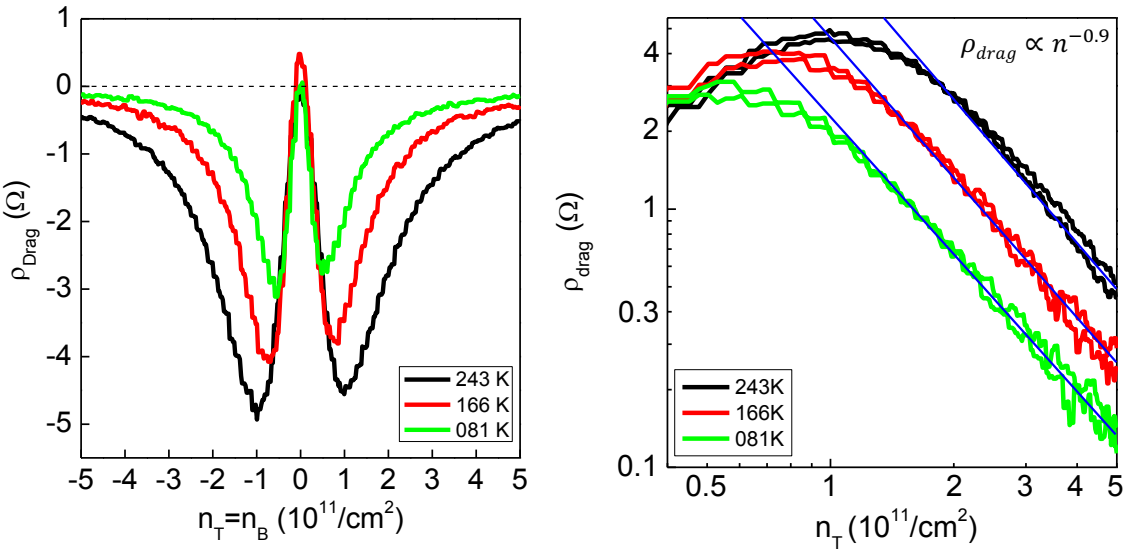

Figure 3.11: ρ_{drag} vs layer densities at different temperatures measured in BiSFET12 (left). Since ρ_{drag} values are taken at $n_B = n_T$ points, negative ρ_{drag} is measured as expected. The right panel shows $|\rho_{drag}|$ vs $|n_T|$ of the identical data in a log-log plot, where the linear dependence indicates the power law dependence. Both electron-electron and hole-hole drag resistivities are drawn in the same graph, showing the similar density dependence. Blue lines show the linear fitting results, whose slopes provide the exponent.

are exactly the same amount, transfer equal and opposite momentum to the drag layer carriers, leading to zero drag resistivity. (2) If the drag layer is at the charge neutrality point, the momentum transferred from the drive layer will be again equal and opposite direction and $\rho_{drag} = 0$.

The smoothness of the crossover can be explained by the coexistence of electron and hole puddles near the charge neutrality point, which generate drag electric fields of opposite sign, and cancel the ρ_{drag}. We expect the slope of the transition to be sharper in cleaner samples with lower charged impurity concentration, and therefore with less electron-hole puddles.

3.3.4 Mesoscopic fluctuations in Coulomb drag

We observe a macroscopic-to-mesoscopic transition in the drag resistance for temperatures lower than 50 K as shown in Figure 3.12. As T is reduced, the ρ_{drag} data start to develop fluctuations superposed on the average ρ_{drag} vs V_{BG} dependence of Equation 3.32, which is valid for average drag at higher temperatures. The fluctuation is fully reproducible in different measurements in the same cool down as shown in Figure 3.13, differentiating itself from the trivial electrical noise.

3.3.4.1 Phase coherence length

The important length scale to understand drag fluctuations is the phase coherence length, L_φ, which defines the distance that carriers can travel without losing their phase memory by inelastic scattering events such as in electron-electron and electron-phonon scattering events. At low enough temperatures, the density of phonons is

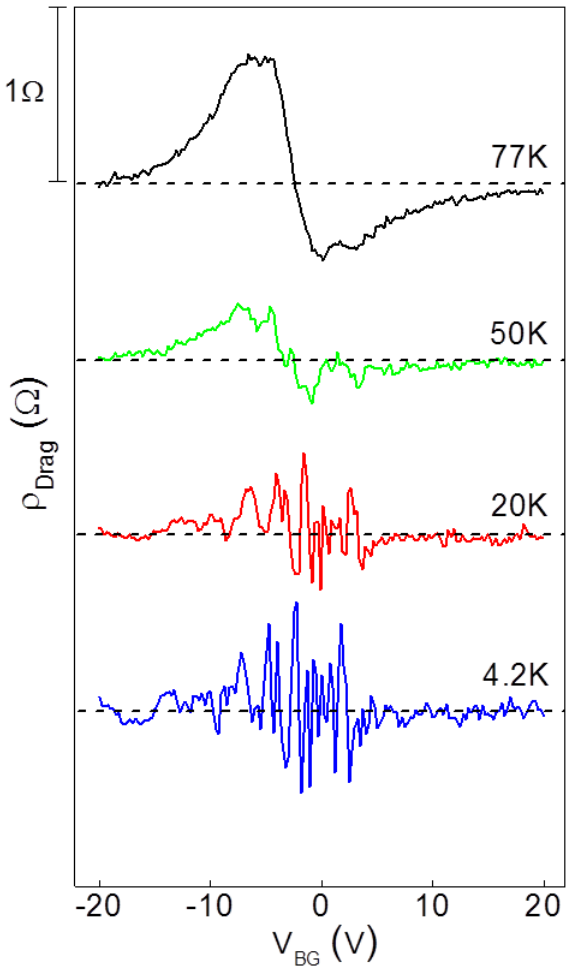

Figure 3.12: ρ_{drag} vs V_{BG} measured for T $\leq$ 77 K in BiSFET6. As T is reduced, mesoscopic fluctuations develop and fully obscure the average drag. The traces are shifted for clarity; the horizontal dashed lines indicate 0 Ω for each trace. Adapted from Ref.[3].

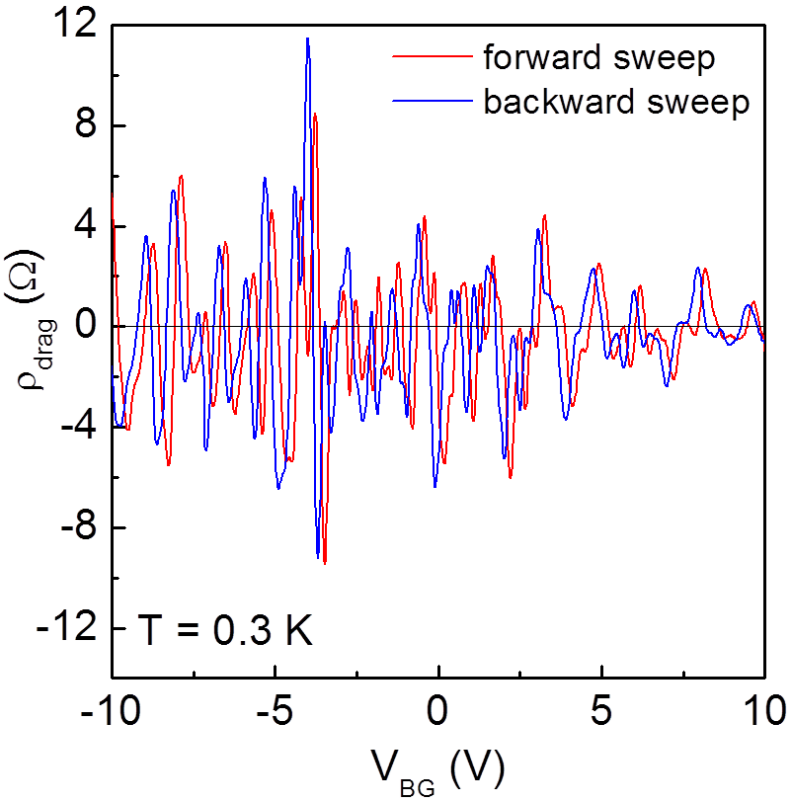

Figure 3.13: Reproducibility of drag fluctuation: ρ_{drag} vs V_{BG} at T = 0.3 K in BiSFET10: the forward sweep (red line) and backward sweep (blue line). A slight shift of one trace relative to the other is caused by the sweep rate which was slightly faster than the lock-in integration time.

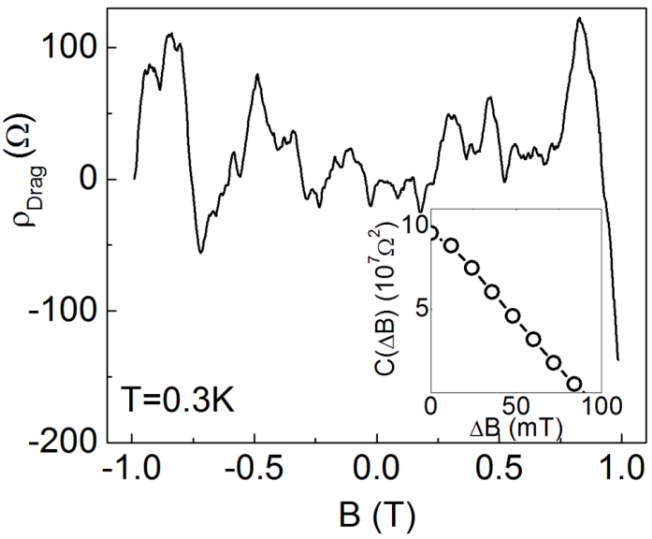

Figure 3.14: ρ_{drag} vs B measured at T = 0.3 K in BiSFET8, showing drag fluctuations as a function of magnetic field. Inset: Autocorrelation of the main panel data. The bottom (top) layer is the drive (drag) layer. Adapted from Ref.[3].

small and electron-electron interaction is the dominant dephasing mechanism [61]. In this condition the phase coherence length can be increased to the value significant to the sample dimension and electron waves traveling along different paths can interfere [Figure 3.16] creating interesting transport phenomena such as universal conductance fluctuations [62].

The phase coherence length can be determined by calculating autocorrelation function of $\sigma_{drag}[B]$, the drag conductivity fluctuation measured as a function of applied transverse magnetic field, and extracting a correlation magnetic field. The autocorrelation function, $C[\Delta B]$, of a discrete function, $\sigma_{drag}[B]$, is defined as:

$$C[\Delta B] = \sum_{B} \sigma_{drag}[B] \;\; \sigma_{drag}[B + \Delta \mathrm{B}].$$

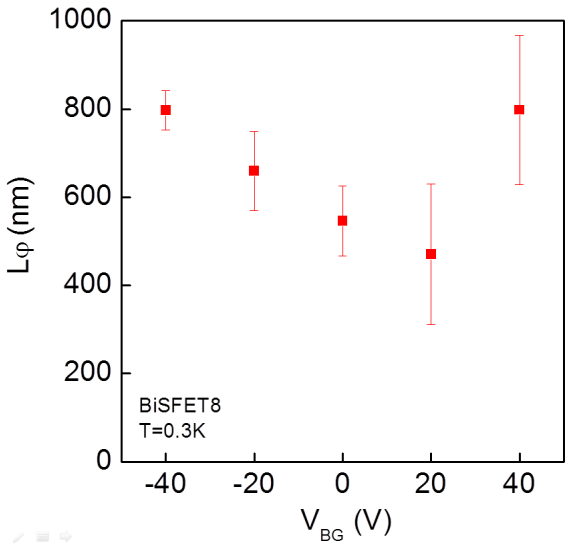

Figure 3.15: Phase coherence length L_φ determined as a function of V_{BG} in BiSFET8 at T = 0.3 K.

An example of measured drag fluctuations as a function of magnetic field and the autocorrelation function are plotted in Figure 3.14. The correlation field, B_c, is defined as the half-width at half-height, $C\left[\Delta B_c\right] = C\left[0\right]/2$, corresponding to the magnetic field required to increase the flux passing through a coherent area by one flux quantum:

$$B_c = \frac{h}{eL_\varphi{}^2}.$$

Figure 3.14 data reveal a correlation field $B_c = 47mT$, which corresponds to a phase coherence length $L_\varphi = \sqrt{h/eB_c} = 300$ nm. Similar measurements performed in the same sample at different back gate biases provide the range of phase coherence length $L_\varphi = 600 \pm 300$ nm. The value extracted from ensemble average measurements using scanning gate microscopy was consistent with the value determined from our

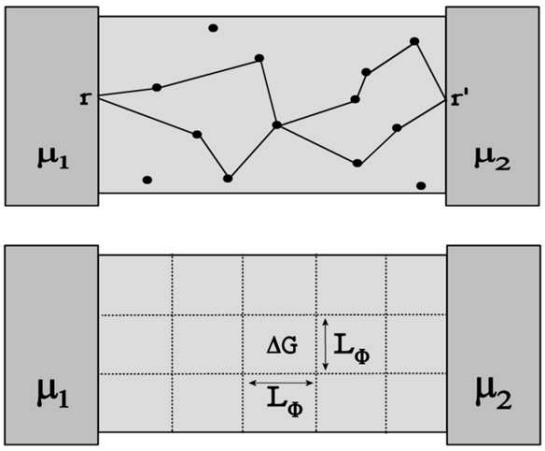

Figure 3.16: (Top) Electrons can take different trajectories when passing through a disordered two-terminal sample. If phase coherence is maintained, they can interfere. (Bottom) When the sample dimension is larger than the phase coherence length, the sample can effectively be regarded as a network of coherent regions of $L_\varphi{}^2$ and the conductance variance of ΔG. Adapted from Ref.[7].

measurements [63].

3.3.4.2 Universal conductance fluctuations

Drag fluctuation represents the counterpart of universal conductance fluctuation in Coulomb drag [64, 65] sharing the same origin. Universal conductance fluctuations are random fluctuations of the conductance as a function of magnetic field, chemical potential, and impurity configuration by a universal amount g $=e^2/h$, which is *independent of sample size and degree of disorder* [62]. This phenomenon is a consequence of interference between the various trajectories that electrons can take when traveling in a sample as shown in the top panel of Figure 3.16. Then a variance of the conductance fluctuation under the condition that the sample is diffusive, $l \ll L$, and at low temperatures, $L_\varphi > L$:

$$\Delta G \sim \left(\frac{e^2}{h}\right)^2.$$

At finite temperatures, phase coherence may not be maintained over the entire sample ($L_\varphi < L$) so that electrons lose its phase coherence before it reaches to the end of the channel. Then the sample can be regarded as a network of phase coherent regions, ${L_\varphi}^2$, and each region display a variance of $\Delta G \sim \left(\frac{e^2}{h}\right)^2$ as shown in Figure 3.16 (bottom). In this case, the variance of the fluctuation will be a classical average of the network of resistors with the effect of thermal broadening of the Fermi-Dirac distribution:

$$\Delta G \sim \left(\frac{e^2}{h}\right)^2 \left(\frac{L_\varphi}{L}\right)^2 \left(\frac{L_T}{L_\varphi}\right)^2 = \left(\frac{e^2}{h}\right)^2 \left(\frac{L_T}{L}\right)^2,$$

where $L_T = \sqrt{\hbar D/k_B T}$ is the thermal length. The above relations equally apply to the Coulomb drag fluctuations which share the fundamental principle with universal conductance fluctuations.

3.3.4.3 Giant magnitude of drag fluctuations

There is an important difference between universal conductance fluctuations and drag fluctuations. While universal conductance fluctuations only add small variance in the average value of the conductance, the drag fluctuations can be larger than the average drag in scale and even change the sign of the Coulomb drag randomly. Price *et al.* first reported reproducible fluctuations of the drag turn out to be much larger than its average value at very low temperatures, $T < 1$ K, in GaAs/AlGaAs

double layers [66]. This result is consistent with our observation in graphene double layers, where the amplitude of drag fluctuations becomes comparable to or one to two orders of magnitude larger than that of the average drag resistivity.

Price *et al.* [64] proposed a plausible qualitative explanation for the four orders of magnitude higher enhancement in drag fluctuations than the theoretical prediction reported in [67] with the assumption of diffusive motion of interacting electrons. The British group argued that the giant drag fluctuations are caused by large momentum transfers between two electrons interacting at a small distance, and at such short range interactions it is the local electron properties of the layers that determine electron-electron interaction. The fluctuations of local density of states are known to exceed those of global density of states by a factor of $g = e^2/h$ [65], and, therefore, the drag fluctuations are greatly enhanced. To elaborate the interlayer electron-electron interaction will be limited to two electrons located at a small distance Δr in the order of the layer spacing d, because the longer range interactions at distances $\Delta r \gg d$ will be screened by other electrons. The smallest distance in which electrons in different layers can interact is d and the interlayer momentum transfer, q, is limited by $q < 1/d$, which originated from the fundamental quantum mechanical uncertainty principle, $\Delta r \Delta q \sim 1$. To generate the giant drag fluctuations, the large momentum transfer is necessary and Δr needs to be small; the two electrons interact at a distance Δr that is smaller than the average impurity separation, $\Delta r < l$. At such a small distance, it is the local properties of the layers that determine electron-electron interaction, not the global properties averaged over the entire sample. As a result, larger fluctuation in the *local* density of states creates electron-hole asymmetry, and this greatly enhances the drag fluctuation through the nonlinear susceptibility term in Equation 3.30.

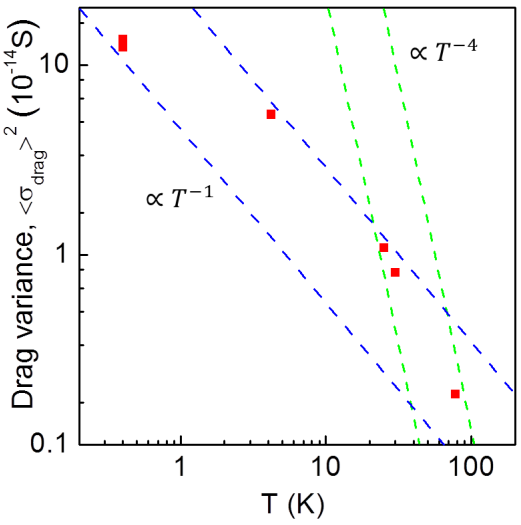

Figure 3.17: Drag conductivity variance vs T measured in BiSFET12 is plotted in a log-log plot. Each variation value is determined in wide range of layer densities using a few tens of thousands data points.

The authors insisted that a temperature dependence of drag fluctuations created by such mechanism is uniquely given by:

$$\left\langle {\sigma_{drag}}^2 \right\rangle \propto \begin{cases} T^{-1} & \text{if } T < \dfrac{\hbar}{k_B \tau} \\ T^{-4} & \text{if } T > \dfrac{\hbar}{k_B \tau} \end{cases}$$

where drag conductivity, σ_{drag}, is $\sigma_{drag} \approx \rho_{drag}/\rho_T \rho_B$ and $\langle {\sigma_{drag}}^2 \rangle$ is the variance of σ_{drag}.

In our measurements, the mean free path in each layer $l = (h/2e^2\sqrt{\pi})\mu\sqrt{n}$ is 50 nm $\leq l \leq$ 130 nm, and the transition temperature $T_t = \hbar/k_B\tau$ separating the two regimes is 70 K $\leq T_t \leq$ 170 K. Since the drag fluctuations become very small at these high temperatures, it is difficult to separate the fluctuation component and study the temperature dependence of drag fluctuations in the regime of $T > T_t$. In

Figure 3.17, $\langle {\sigma_{drag}}^2 \rangle$ as a function of temperature is plotted with T dependence guide lines corresponding to $T < T_t$ regime (blue lines) and $T > T_t$ regime (green lines). More data will be needed to verify if our data support Price *et al.*'s explanation or not.

3.3.4.4 Onset temperature of drag fluctuation

The ρ_{drag} fluctuations become noticeable below 77 K and fully obscure the average diffusive drag below 20 K in our graphene double layers [Figure 3.12]. This manifestation of mesoscopic physics at elevated temperatures is closely related to the high Fermi energy, E_F, in graphene, roughly ten times higher than that in semiconductor heterostructures. Narozhny *et al.* [67] defined the critical temperature, T^* as the temperature at which the crossover from the average Coulomb drag regime to the fluctuation regime occurs. They suggested that it is proportional to E_F, $T^* \propto E_F$, supporting the observation of drag fluctuations at high temperatures in graphene.

3.4 Conclusion

Interesting observations on the drag fluctuation results in graphene which are not understood at present or require more careful work are summarized as following: (1) density dependence of ρ_{drag} fluctuation - drag fluctuation amplitude reaches a maximum near the charge neutrality point of the layers and slowly decrease as layer densities increase [Figure 3.18]; (2) drag layer density dependence of fluctuations - drag resistivity fluctuates strongly depending on the drag layer density, but

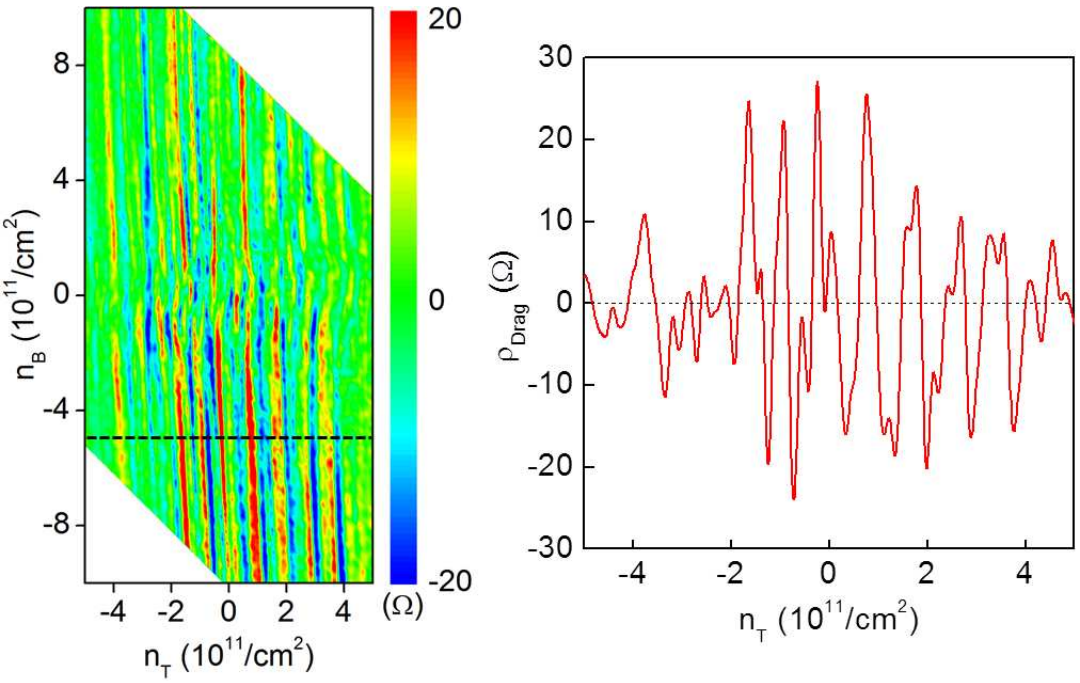

Figure 3.18: Contour plot of ρ_{drag} mapped in the plane of n_T and n_B measured in BiSFET8 at 4.2K (left) and a ρ_{drag} trace along the constant bottom density line, at n_B = - 5 $\times$ 10^{11} cm^{-2}, (right) marked by a dashed line in the left panel. The bottom (top) layer is the drive (drag) layer.

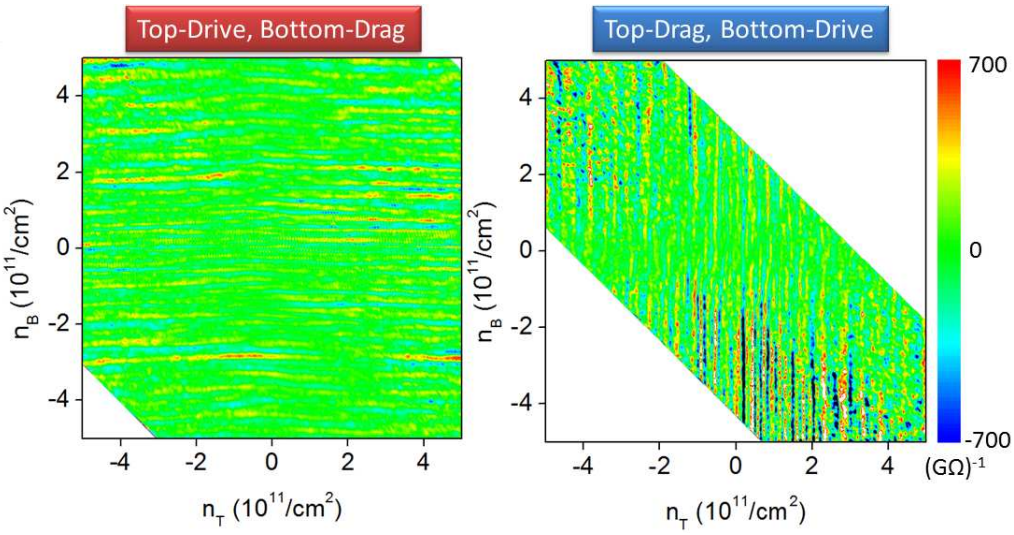

Figure 3.19: σ_{drag} as a function of n_T and n_B measured at 0.4K in BiSFET12 The drag layer is the bottom layer (left) or top layer (right) in each measurement, respectively. The fluctuation patterns are parallel to the constant density lines of the drag layer.

insensitive on the drive layer density. When drive layer and drag layer are swapped, line-shaped fluctuation patterns observed in one measurement setup is orthogonal to those measured in the other setup as shown in Figure 3.19.

In summary, we probe the Coulomb drag in independently contacted graphene double layers. At elevated temperatures, the drag resistance dependence on density and temperature is consistent with the Fermi liquid theory. At reduced temperatures, the drag exhibits mesoscopic fluctuations that obscure the average drag, a result of the interplay between electron-electron interaction and phase-coherent intralayer transport.

Chapter 4

Direct Measurement of Fermi Energy in Graphene Using a Double Layer Heterostructure

The Fermi energy is a fundamental property of an electron system, which is closely related to the host material's density of states, energy band structure and electron interaction effects. In this chapter, we introduce a technique which allows a direct measurement of the relative Fermi energy in an electron system using a graphene double layer structure. We demonstrate this method by measuring the Fermi energy in a graphene single layer as a function of density, at zero and in high magnetic fields, and determine the Fermi velocity, Landau level spacing and Landau level broadening in graphene.

4.1 Introduction

The Fermi energy or density of states of a two-dimensional electron gas is key to understand electron transport properties and phenomena at strong magnetic fields such as the quantum Hall effect. A number of thermodynamic properties can be measured to extract the density of states in an electron system. By applying a heat pulse or heat flux of a short duration and probing the temperature change in the sample, Gornik *et al.* [68] and Wang *et al.* [69] measured the magnetic-field-dependent

specific heat, $C_{electron}$, for two-dimensional electrons in GaAs/AlGaAs multilayers and extracted its density of states using the relation:

$$C_{electron} = \int E \, \frac{df(E)}{dT} \, D\,(E) \;\; dE,$$

where $f(E)$ is the Fermi-Dirac distribution function, T is the temperature and $D(E)$ is the density of states. Eisenstein *et al.* [70] measured the magnetization in GaAs/AlGaAs single and multilayer heterostructures by a torsional technique to observe the shape and amplitude of density of states in magnetic fields. Capacitive techniques such as magnetocapacitance [71] and compressibility [72] measurement can also be utilized to probe the density of states in an electron system. The thermodynamic compressibility, K, is simply related to the total energy E_{tot} (per unit area), chemical potential, μ, and carrier density n of the system:

$$K^{-1}{=}n^2\frac{\delta^2 E_{tot}}{\delta n^2}{=}n^2\frac{\delta\mu}{\delta n} = n^2 D(E)^{-1}.$$

In the case of graphene, the limited sample size significantly restricts the density of states measurement. In spite of the recent advances in graphene growth techniques, graphene samples of the highest quality are still manually obtained by mechanical exfoliation from graphite crystals, and the dimension of typical graphene devices is in micrometer scale [10]. Therefore, specific heat measurement and magnetization measurement are exceedingly difficult, and the accuracy of compressibility [73, 74] measurement is limited. Ponomarenko *et al.* [75] fabricated giant graphene capacitors ($\sim 100\ \mu\text{m} \times 100\ \mu\text{m}$) using very large graphene flakes to obtain reliably high capacitance signals, however, the measured density of states suffered from the

macroscopic charge inhomogeneity. The density of states measured by other capacitive measurement technique [43] did not agree well with the theory.

In this chapter, using a double layer device structure where graphene is one of the layers we describe a technique which allows a direct measurement of the relative Fermi energy in an electron system which is independent of the sample size. Our technique shares its basic principle with the Kelvin probe measurement [23]. As shown in Figure 4.1, when two materials with different work functions are placed in close proximity and connected by a wire, charge carriers will transfer from the smaller work function material to the larger. This creates the electric field between the surfaces and contact potential difference (CPD) which corresponds to the difference between the work functions. By applying an external DC bias to counter this potential and simultaneously monitoring the charge transfer, the CPD, and therefore work function difference, can be measured. In the practical instruments, a mechanically vibrating tip is used to find the charge-free voltage [Figure 4.2]. We found that in the double layer structure, where one of the layers is a single layer graphene, a graphene layer can be used as a charge-free point detector and replace the vibrating probe by simply measuring its layer resistivity and find the charge-neutrality point. We demonstrate this technique by probing the Fermi energy in graphene both at zero and in high magnetic fields, showing the accurate determination of the Fermi velocity, Landau level spacing, and Landau level broadening in graphene.

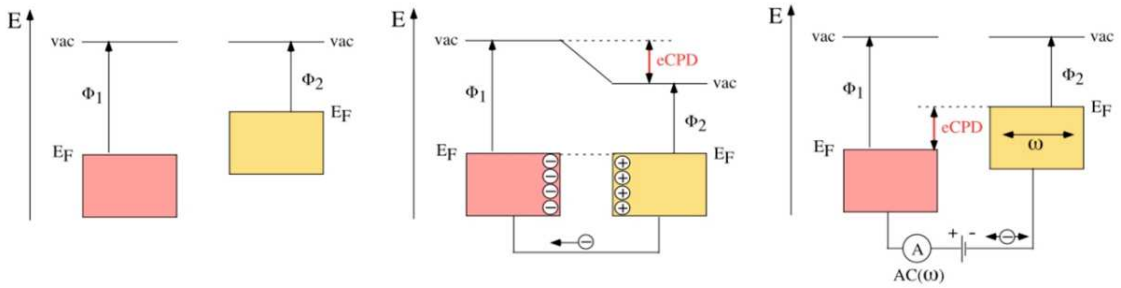

Figure 4.1: Basic principle of the Kelvin probe measurement.

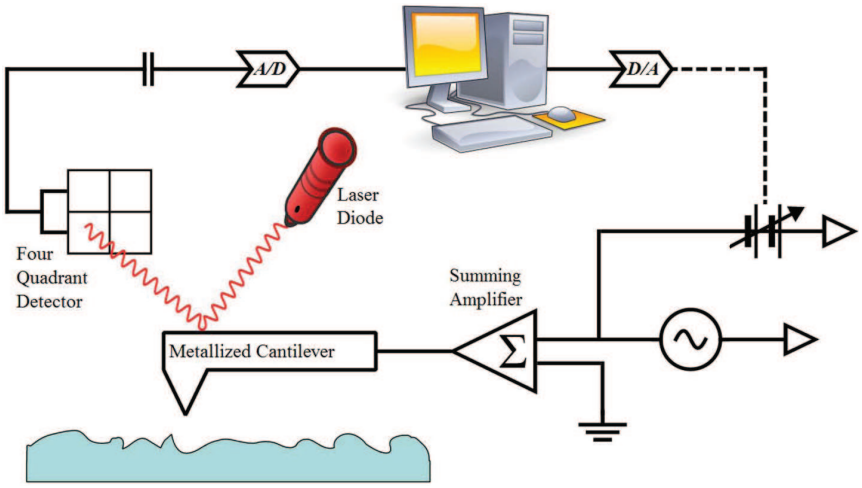

Figure 4.2: Typical setup of the Kevin probe measurement.

4.2 Fabrication

Graphene double layer heterostructures, where two independently contacted graphene single layers are placed in a close proximity but electrically isolated by thin interlayer dielectric, are briefly revisited as shown in Figure 4.3. First, we mechanically exfoliate the bottom graphene layer from natural graphite onto a 285 nm thick SiO_2 dielectric, thermally oxidized on a highly doped Si substrate. The degenerately doped Si substrate will be used as a bottom-gate electrode. Standard e-beam lithography, 50 nm thick Ni or 5 nm thick Cr and 40 nm thick Au deposition followed by lift-off, and O_2 plasma etching are used to define a Hall bar device. A 4 to 9 nm top Al_2O_3 dielectric layer is deposited on the bottom layer by atomic layer deposition using e-beam evaporated Al as a nucleation layer [17]. The dielectric film thickness grown on graphene is further verified by transmission electron microscopy in multiple samples. To fabricate the graphene top layer, another graphene single layer is mechanically exfoliated on a similar SiO_2/Si substrate. After spin-coating poly(methyl methacrylate) (PMMA) on the top layer and curing, we etch the underlying substrate with NaOH, and detach the graphene layer along with some alignment markers captured in the PMMA membrane. The membrane is transferred onto the bottom layer device and aligned under the optical microscope. A Hall bar geometry is patterned on the top layer, and metal contacts are subsequently defined, completing the double layer graphene device [Figure 4.3].

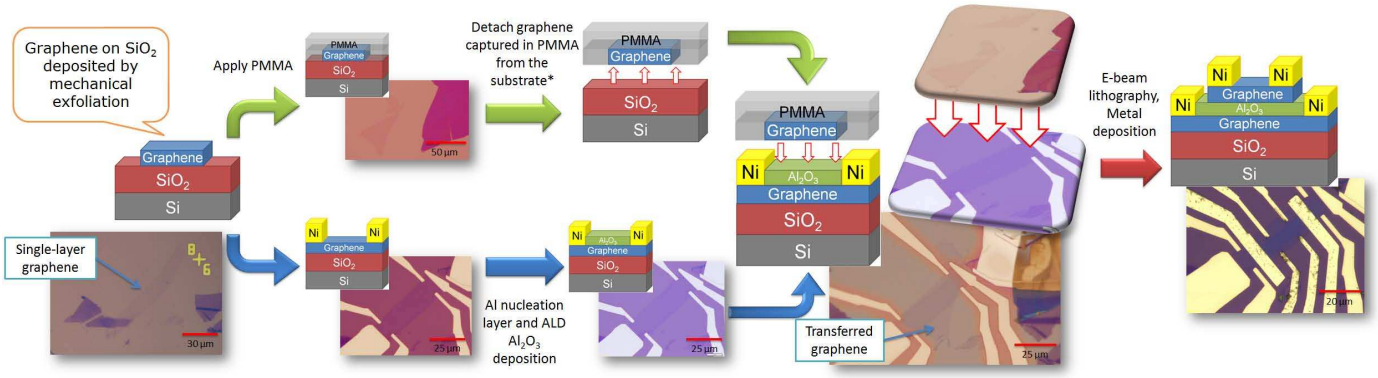

Figure 4.3: Fabrication of a graphene double layer heterostructure. Optical images are taken from BiSFET2.

4.3 Fermi energy measurement using a graphene double layer structure

4.3.1 Principle

A closer examination of the top layer charge neutrality point dependence on V_{BG} and V_{TL} provides the principle of Fermi energy measurement using a double layer heterostructure. If the top layer is at the charge neutrality point, setting $n_T = 0$ in Equation 2.13 yields:

$$\frac{E_{F,B}(n)}{e} = V_{TL}. \tag{4.1}$$

This equation contains a simple, yet remarkable result. The interlayer bias required to bring the top layer to the charge neutrality point is equal to the Fermi energy of the opposite layer, in units of eV. Consequently, tracking the top layer charge neutrality point in the V_{BG}-V_{TL} plane, results in a measurement of the bottom layer Fermi energy as a function of V_{BG}. Furthermore, setting $n_T = 0$ in Equation 2.9, and using Equation 4.1 allows for n_B to be determined as a function of V_{BG} and V_{TL} along the top layer charge neutrality line:

$$V_{BG} - V_{TL} = \frac{e n_B}{C_{SiO_2}}. \tag{4.2}$$

Equations 4.1 and 4.2 provide a direct measurement of the bottom layer Fermi energy as a function of density.

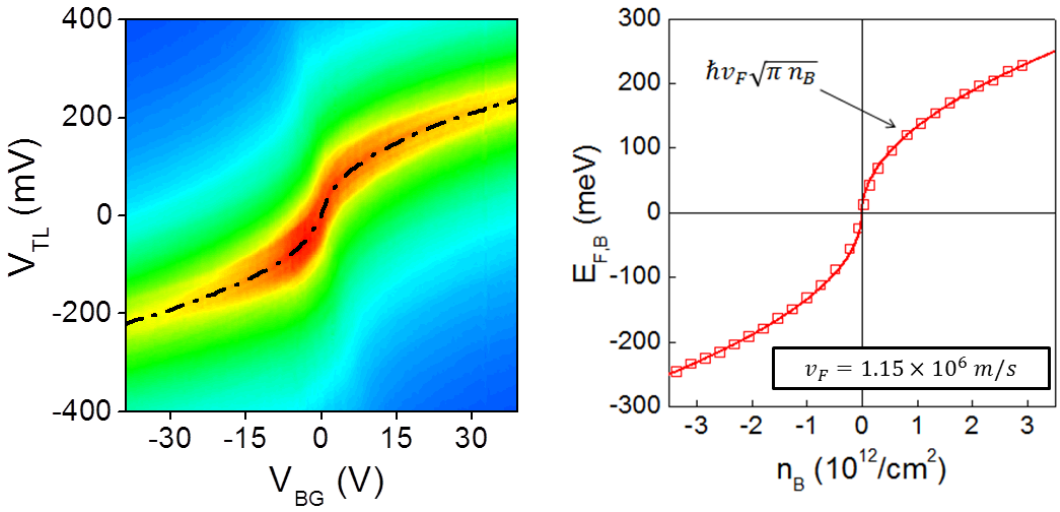

Figure 4.4: Fermi energy as a function of density in the bottom graphene layer of BiS-FET12 (right) extracted from the top layer resistivity measurement (left). Adapted from Ref.[4].

4.3.2 Fermi energy measurement in graphene

To demonstrate the technique, we show the Fermi energy in the bottom graphene layer $E_{F,B}$ as a function of n_B [right panel, Figure 4.4], determined by Equations 4.1 and 4.2 using the data in the left panel of Figure 4.4. The E_F values are in an excellent agreement with the $E_{F,B}(n) = \hbar v_F \sqrt{\pi n_B}$ dependence expected for the linear energy-momentum dispersion of graphene, and with an extracted Fermi velocity of $v_F = 1.15{\times}10^8$ cm/s. This method is powerful because E_F(n) in a material of interest is measured by simply probing a remote graphene layer's resistivity. We can picture this technique as a resistively-determined Kelvin probe, since the top graphene layer serves as a replacement of the mechanically vibrating tip to detect the charge-neutrality point.

4.3.3 Fermi energy measurement in high magnetic fields

Application of a magnetic field to conductors causes the charge carriers to circulate in cyclotron orbits with discrete and degenerate energy levels, called Landau levels. In the following we show that the above method applies equally well to measure the Fermi energy or density of states in an electron system at high magnetic fields, allowing a direct measurement of Landau level energies and broadening. In Figure 4.5 we show the contour plots of ρ_T (top panel) and ρ_B (bottom panel) measured as a function of V_{BG} and V_{TL} in an applied perpendicular magnetic field B = 8 T at T = 0.4 K. Both layers show quantum Hall states marked by vanishing resistivities at filling factors $\upsilon = 4(N + 1/2)$, consistent with those of monolayer graphene [14, 76]. The integer N represents the Landau level index. The top panel of Figure 4.6 shows a staircase dependence of the top layer charge neutrality point on V_{BG} and V_{TL}. Similarly to Figure 4.4, substituting eV_{TL} with $E_{F,B}$ at the top layer charge neutrality line in Figure 4.5 (left panel) provides a mapping of $E_{F,B}$ as a function of V_{BG}. To visualize this, the top layer charge neutrality line in the V_{BG}-V_{TL} plane as shown in Figure 4.6(a) (top panel) is superposed with the ρ_B contour plot of Figure 4.6(a) (bottom panel), which shows staircase-like increments of $E_{F,B}$ coinciding with the bottom layer quantum Hall states.

Figure 4.6(b) shows $E_{F,B}$ vs n_B at B = 8 T determined by tracking the top layer charge neutrality line in the V_{TL}-V_{BG} plane in Figure 4.6 (a), and using Equations 4.1 and 4.1 to convert V_{TL} and V_{BG} into $E_{F,B}$ and n_B, respectively. Figure 4.6(b) also shows ρ_B vs $E_{F,B}$, determined by tracking the bottom layer resistivity along the top layer charge neutrality line [dash-dotted line of Figure 4.6(a)]. Figure 4.6(b) data

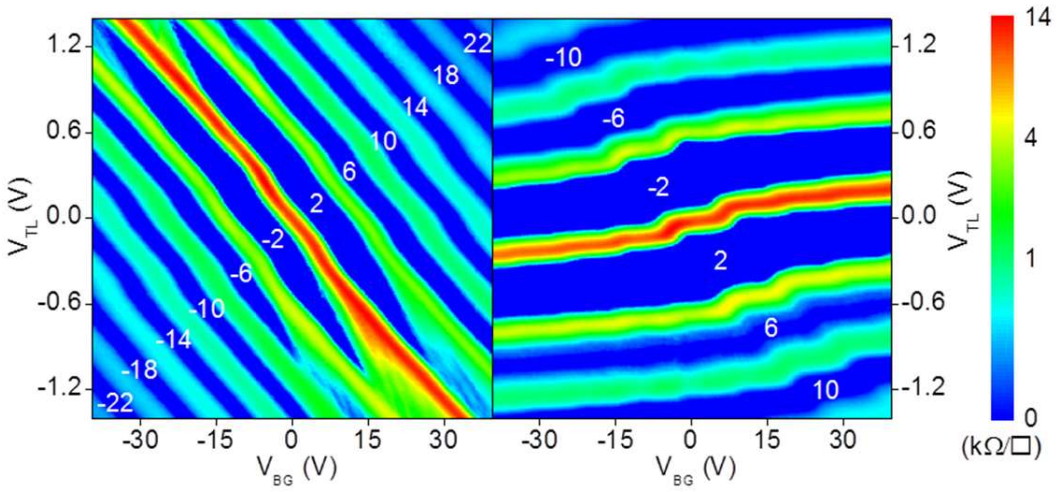

Figure 4.5: ρ_B (left) and ρ_T (right) contour plots measured as a function of V_{BG} and V_{TL} at B = 8T, and T = 0.4 K in BiSFET12.

manifestly show the staircase-like behavior expected for the Fermi level dependence on density for a two-dimensional electron system in a perpendicular magnetic field. The peaks in the ρ_B vs $E_{F,B}$ data of Figure 4.6(b), corresponding to the Fermi level lying in the LL center and probing extended states, correlate with plateaus in the $E_{F,B}$ vs n_B, associated with the large LL density of states. The peaks in the ρ_B vs $E_{F,B}$ data of Figure 4.6(b) provide a direct measurement of the LL energy.

Figure 4.7 summarizes the bottom graphene layer LL energy as a function of index (N) at B = 8 T. The experimental data is in excellent agreement with the theoretical dependence $E_N = \pm v_F\sqrt{2\hbar eB\,|N|}$, corresponding to a Fermi velocity $v_F = 1.17\times10^8$cm/s, a value less than 2 % different than the Fermi velocity determined at B = 0 T using Figure 2.18 data.

In Figure 4.8 we compare the $E_{F,B}$ vs n_B data determined experimentally at B = 8 T, with calculations. Assuming a Lorentzian distribution of the disorder-induced

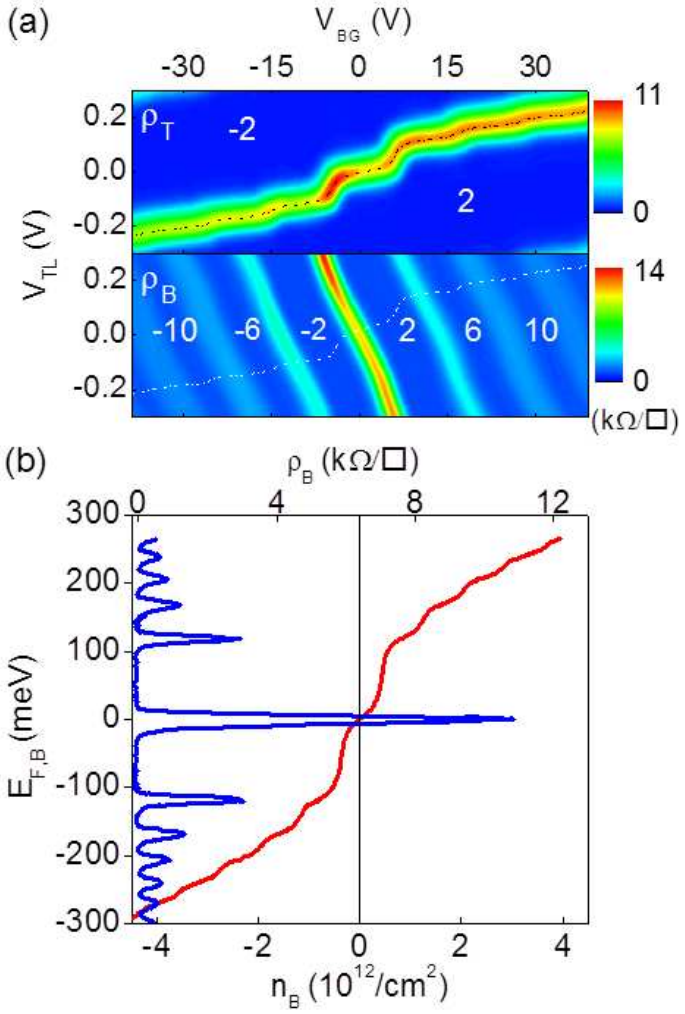

Figure 4.6: (a) ρ_T (top) and ρ_B (bottom) contour plots measured as a function of V_{BG} and V_{TL} at B = 8 T, and T = 0.4 K in BiSFET12. Both layers show quantum Hall states marked by vanishing longitudinal resistance at filling factors $\nu = \pm$ 2, 6, 10, consistent with monolayer graphene. The top layer charge neutrality line (dashed line) shows a staircase-like dependence, with the steps matching the bottom layer quantum Hall states. (b) ρ_B (blue line, top axis) vs $E_{F,B} = eV_{TL}$, and $E_{F,B}$ vs n_B (red line, bottom axis) determined from the top layer charge neutrality line of panel (a). The $E_{F,B}$ values at the peak position of ρ_B provide the center positions of Landau levels. Adapted from Ref.[4].

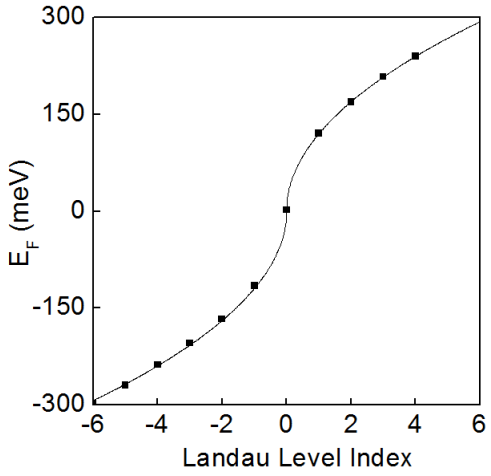

Figure 4.7: Landau level energy in monolayer graphene as a function of index (N). The symbols are experimental data determined from the $E_{F,B}$ positions at the ρ_B peaks in Figure 4.6(b). The solid line is the theoretical $\pm v_F\sqrt{2\hbar eB\,|N|}$ dependence using $v_F = 1.17 \times 10^8$ cm/s. Adapted from Ref.[4].

LL broadening, the density of states D(E) writes:

$$\mathrm{D\,(E)} = \frac{4e}{h} B \sum_N \frac{1}{\pi} \frac{\gamma_N}{(E - E_N)^2 + {\gamma_N}^2} \tag{4.3}$$

with γ_N being the broadening of the Nth LL. The carrier density (n) dependence on E_F in the limit T = 0 K is:

$$\mathrm{n}\,(E_F) = \int_0^{E_F} D\,(E)\,dE. \tag{4.4}$$

Using Equations 4.3 and 4.4, the best fit to $E_{F,B}$ vs n_B data is obtained for γ_N= 6.5 meV, and γ_0= 14 meV for $|N| > 0$. The summation in Equation 4.3 does not converge if carried out to infinity, and a high-energy cutoff is customarily used. For the calculations of Figure 4.8 we used $|N| \leq 100$ in Equation 4.3, corresponding to a 1

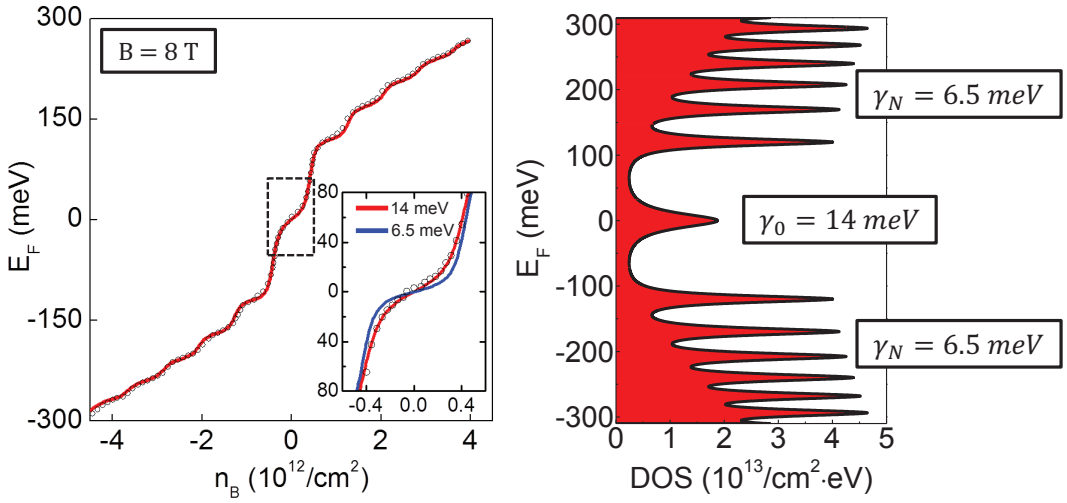

Figure 4.8: $E_{F,B}$ vs n_B at B = 8 T and at T = 0.4 K in BiSFET12. In the left panel, the symbols represent experimental data, and the solid (red) line is a fit assuming a Lorentzian broadening in each Landau level. The best fit is obtained with γ_N= 6.5 meV for $|N| > 0$, γ_0= 14 meV, and with $v_F = 1.17 \times 10^8$ cm/s . The lower inset shows the E_F vs n_B data, and the lines are calculations with different γ_0= 14 meV (red line) and γ_0= 6.5 meV (blue line). The right panel shows the extracted density of states corresponding to the best fit line in the left panel.

eV cutoff energy; increasing the cutoff LL index to 1,000 will change the best fit value by less than 0.5 meV. The lower inset of Figure 4.8 (left panel) shows a comparison of the $E_{F,B}$ vs n_B experimental data with calculations using the same broadening for the N = 0 LL as the upper and lower LLs, γ_N= 6.5 meV. The larger broadening of the N = 0 LL by comparison to the other LLs is an interesting finding. A theoretical study [77], which examined the impact of static disorder on LL broadening in graphene without considering interaction showed that the N = 0 LL broadening is the same as for the other LLs. On the other hand electron-electron interaction can impact the broadening of the fourfold degenerate N = 0 LL, and experimental data on exfoliated graphene on SiO_2 substrates show a splitting of the N = 0 LL in high, B = 45 T magnetic fields [78], explained as a many-body effect.

Lastly, we note that a Gaussian-shaped Landau level density of states yields worse fits to the Figure 4.8 data, by comparison to the Lorentzian shape density of states. Scanning tunneling microscopy [79, 80], and compressibility studies in graphene [73] also favor the Lorentzian LL line shape by comparison to the Gaussian one. A recent theoretical study argues that LL local density of states has a Lorentzian line shape while the total density of states is Gaussian [81]. Presumably, the sample size examined here, defined by a 4 μm Hall bar width coupled with the 8 μm top layer contact spacing is sufficiently small such that the Lorentzian LL line shape dominates.

4.3.4 Fermi energy measurement at non-zero top layer density

We introduced a method to calculate the Fermi energy of the bottom layer at the points where the top layer is at its charge neutrality point, n_T=0. Here, we

will prove that at any set of constant n_T points we can use the principle of the Fermi energy measurement technique, and extract the Fermi energy.

If the top layer density is fixed at a certain value, n_T=n_T^*, Equations 2.12 and 2.13 yield:

$$eV_{BG}=\frac{e^2\ n_B}{C_{SiO_2}}+eV_{TL}+C_1, \tag{4.5}$$

$$E_F\left(n_B\right)=eV_{TL}+C_2, \tag{4.6}$$

where $C_1 = e^2\ n_T^*/C_{SiO_2} + e^2 n_T^*/C_{Al_2O_3} + E_F\left(n_T^*\right)$ and C_2=$e^2 n_T^*/C_{Al_2O_3}$+$E_F\left(n_T^*\right)$ are both constant at a given n_T=n_T^*. This set of equations can be interpreted as follows: if one tracks the points with a constant density of any value, then we can calculate the bottom layer's Fermi energy using Equations 4.5 and 4.6 with additional constant terms. Since C_1 and C_2 are required to be constant at a fixed top layer density, Equations 4.5 and 4.6 after constant compensation for C_1 and C_2 provide the Fermi energy as a function of layer density just as Equations 2.12 and 2.13. This observation further extends our method by enabling the Fermi energy measurement at any constant n_T points.

This extension of the technique is particularly useful when the experimental access of $n_T = 0$ points is difficult due to the practical limitations. For example, when the charge neutrality point in a device is away from the zero bias point, a high back gate and interlayer bias are necessary to examine the region where $n_T = 0$, which can be potentially destructive to the device. Therefore, in some cases, it is better to track a non-zero, constant top layer density points and calculate the Fermi energy in the bottom layer.

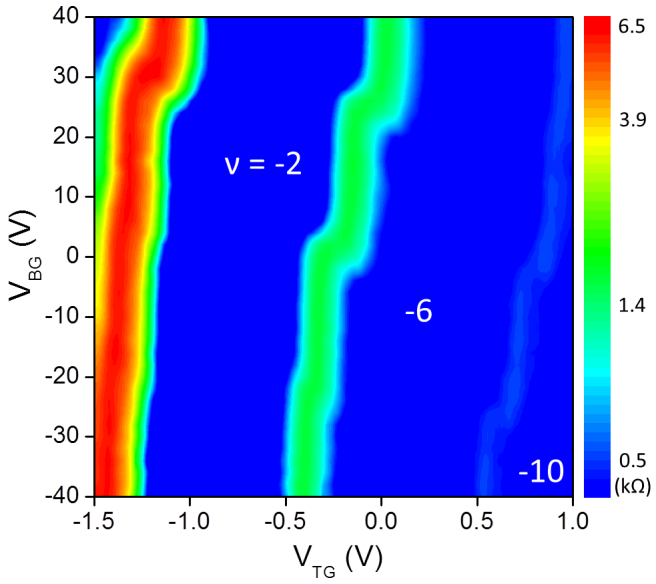

Figure 4.9: ρ_{xx} vs V_{TL} and V_{BG} at T = 17 mK and at B = 18 T measured in BiSFET11. The quantum Hall states distinguished with a vanishing resistivity are marked with the corresponding filling factors.

Figure 4.9 shows a longitudinal resistivity of BiSFET11 measured at T = 17 mK and B = 18 T, with the absolute charge neutrality point, where $n_T = n_B = 0$, positioned at $V_{BG} = +40\ V$ and V_{TL}=$-1.2\ V$. Due to the large shift of the absolute zero density point, the points where $n_T = 0$ are located at large negative V_{TL} (red peak region in Figure 4.9). Instead of tracking the $n_T = 0$ points, we follow the points where the filling factor $\upsilon = -4$ ($n_T = -1.74 \times 10^{12}$ cm^{-2} at B = 18 T) marked by the green peak region in the center of the contour plot [Figure 4.9] and calculate the Fermi energy using Equations 4.5 and 4.6. The results obtained at B = 10, 14 and 18 T are shown in Figure 4.10. Again, the staircase-like dependence of the Fermi energy as a function of the bottom layer density corresponding to the LL formation at high magnetic fields are observed (green line), evincing that our technique extends to non-zero top layer density points as well as at higher magnetic fields. Similar

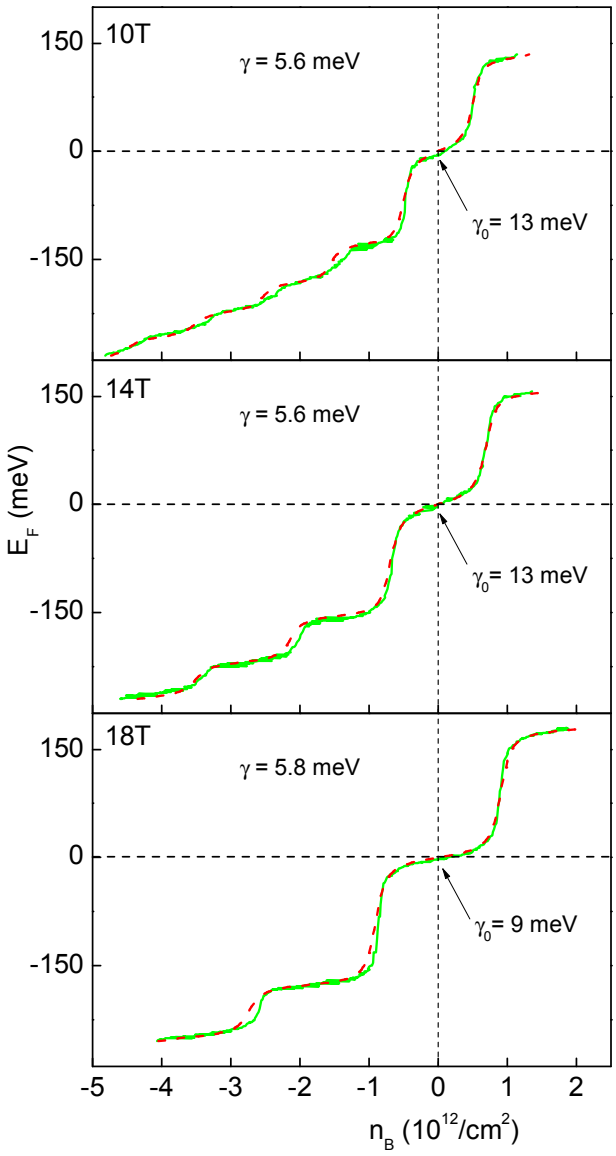

Figure 4.10: E_F vs n_B measured at T = 17 mK and at different magnetic fields in BiS-FET11. Lines (green) are experimental data, and dashed lines (red) are calculations using the broadenings γ_0 and γ as presented.

fitting as demonstrated in Figure 4.8 is performed to Figure 4.10 data and shown as red dashed lines in Figure 4.10. Consistent with the previous finding, N = 0 LL is broader than all other LLs at all the magnetic fields we probe. One interesting observation is that the broadening of zeroth LL is 30 % smaller at 18 T compared to that at lower magnetic fields, while the broadening of N = 0 LLs stays at similar value. Further experimental investigation is required to draw a conclusion on the magnetic field dependence of LL broadening.

4.4 Conclusion

In summary, we present a method to determine the Fermi energy in a two-dimensional electron system, using a graphene double-layer heterostructure. The graphene gate serves as not only a gate to control the densities in the channel but also a sensor to detect the charge-free point which is corresponding to the maximum resistance point of the graphene gate. We illustrate this technique by probing the Fermi energy in single layer graphene at zero and in a high magnetic fields, and determine with high accuracy the Fermi velocity, Landau level spacing, and Landau level broadening.

Chapter 5

Spin-polarized to Valley-polarized Transition in Graphene Bilayers at $\nu = 0$ in High Magnetic Fields

In this chapter, we investigate the $\nu = 0$ quantum Hall state (QHS) in dual-gated graphene bilayers, and analyze its dependence on transverse electric (E) and perpendicular magnetic field (B). The dual-gated structure enables the independent control of E field and layer density in graphene bilayers. The longitudinal resistivity ρ_{xx} measured at $\nu = 0$ shows an insulating behavior which is strongest in the vicinity of E = 0, as well as at large E fields. At a fixed perpendicular magnetic field, the $\nu = 0$ QHS undergoes a transition as a function of the applied E, marked by a minimum, temperature-independent ρ_{xx}. This observation is explained by a transition from a spin-polarized $\nu = 0$ QHS at small E fields to a valley(layer)-polarized $\nu = 0$ QHS at large E fields. The E field value at which the transition occurs follows a linear dependence on B.

5.1 Introduction

Graphene bilayers [8, 21] represent an attractive system for electron physics and potential device application. This system exhibits a transverse electric field tunable bandgap [18, 19], as evidenced by angle-resolved photoemission [82] and transport

measurements [83, 84]. In a perpendicular magnetic field, the electrons occupy quantized and degenerate energy levels, Landau levels (LLs). Graphene bilayers show quantum Hall states at integer filling factors (ν) multiple of four [8, 83], owing to spin and valley degeneracy [Figure 5.1]. Interestingly, without an applied E field (E = 0) the $\varepsilon = 0$ Landau levels in graphene bilayers show an eight-fold degeneracy at the charge neutrality point (zero density), namely two orbital LLs (N = 0, 1) along with their respective double spin and valley degeneracy. Here, we show that spin and valley degeneracy of the graphene bilayer's $\varepsilon = 0$ LLs can be lifted by applied E field and B field, leading to broken symmetry QHSs. An applied B field lifts the spin degeneracy thanks to the Zeeman splitting, while an applied E field lifts the valley degeneracy [19]. Broken symmetry states were experimentally observed in single-gated suspended [85] and supported [86] graphene bilayers, and explained by electron-electron interaction effect [87].

We investigate dual-gated graphene bilayers, a device geometry which allows independent control of the total density and transverse electric field. At a fixed perpendicular magnetic field, we observe the emergence of a QHS at filling factor $\nu = 0$ in the presence of a transverse electric field, evinced by a large longitudinal resistivity (ρ_{xx}) with an insulating behavior, consistent with the opening of a gap between the electron and hole bands. Interestingly, as the B field is increased we observe a developing $\nu = 0$ QHS at E = 0, explained by the Zeeman splitting of the Landau levels at zero energy. As a function of E, the $\nu = 0$ QHS undergoes a transition from spin polarized at small E fields, to valley(layer)-polarized at large E fields.

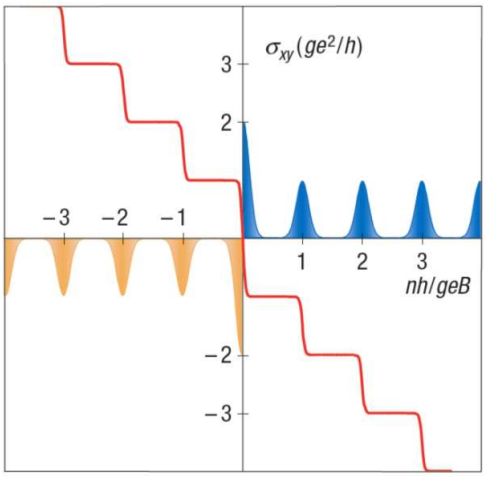

Figure 5.1: Integer quantum Hall Effect in graphene bilayer. Plateaus in Hall conductivity σ_{xy}occur at values $(4e^2/h)N$, where N is an integer, e^2/h the conductance quantum and 4 the double spin and double valley degeneracy. The distance between steps along the concentration axis is defined by the degeneracy $4e^2B/h$ on each Landau level. Adapted from Ref.[8].

5.2 Realization of a Dual-gated Graphene Bilayers

Our samples consist of natural graphite mechanically exfoliated on a 300 nm SiO_2 dielectric layer, thermally grown on a highly doped n-type Si substrate, with an As doping concentration of $\sim 10^{20}$ cm^{-3}. Optical inspection and Raman spectroscopy are used to identify graphene bilayer flakes for device fabrication. We define metal contacts using electron beam (e-beam) lithography followed by 50 nm Ni deposition and lift-off [Figure 5.2]. A second e-beam lithography step followed by O_2 plasma etching is used to pattern a Hall bar on the graphene bilayer flake. To deposit the top gate dielectric, we first deposit a 2-nm-thick Al layer as a nucleation layer for the atomic layer deposition of Al_2O_3 [17]. The sample is then transferred *ex-situ* to an atomic layer deposition chamber. X-ray photoelectron spectroscopy and electrical

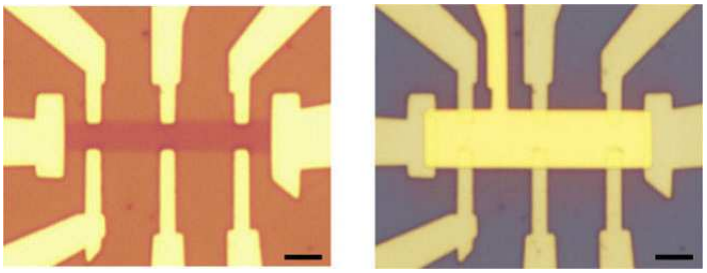

Figure 5.2: Optical micrograph of a dual-gated graphene bilayer, sample K24, before (left) and after (right) top gate deposition. Both scale bars are 3 μm. Adapted from Ref.[9].

measurements confirm the Al layer is fully oxidized in the presence of residual O_2 during evaporation, and the exposure to ambient O_2 [88]. Next, a 15-nm-thick Al_2O_3 film is deposited using trimethyl aluminum as the Al source and H_2O as oxidizer, followed by the Ni top gate deposition [Figure 5.2].

5.3 Characterization

5.3.1 Transport characteristics at zero magnetic field

Longitudinal (ρ_{xx}) and Hall (ρ_{xy}) resistivity measurements are performed down to a temperature of T = 0.3 K, and using standard low-current, low-frequency lock-in techniques. Three samples, labeled as K24, K18, and N046, with mobilities of 1500 - 2400 cm^2/Vs were investigated in this study, all with similar results. We use Hall measurements to determine the total carrier density (n_{tot}) as a function of top (V_{TG}) and back (V_{BG}) gate voltages, and the corresponding capacitance values. Equally relevant here is the transverse electric field, which induces an imbalance between the bottom (n_B) and top (n_T) layer densities. Up to an additive constant, n_{tot} and E are

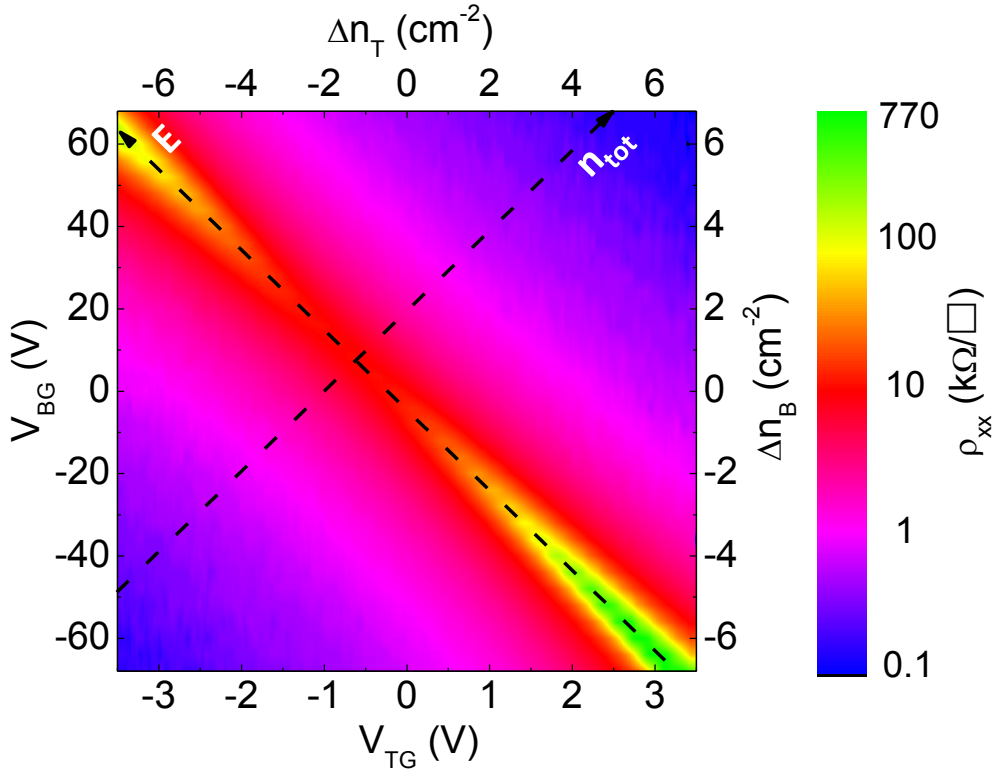

Figure 5.3: Contour plot of ρ_{xx} measured as a function of V_{TG} and V_{BG} in sample K24. The right and top axes represent the density change for the back and top gates, respectively. Adapted from Ref.[9].

related to V_{TG} and V_{BG} by

$$n_{tot} = (C_{BG}V_{BG} + C_{BG}V_{BG})/e,$$

and

$$E = (C_{BG}V_{BG} - C_{BG}V_{BG})/2\epsilon_0,$$

where e is the electron charge, and ϵ_0 is the vacuum dielectric permittivity. To calculate the E field we offset V_{TG} and V_{BG} by the gate biases required to reach n_{tot} = 0 and E = 0. The C_{TG} values for our samples range between 225 and 270 nF/cm^2, with a dielectric constant k = 4.2 - 5.

In Figure 5.3 we show ρ_{xx} measured as a function of V_{TG} and V_{BG} in sample K24, at T = 0.3 K. The diagonals of constant $C_{BG}V_{BG} + C_{BG}V_{BG}$ represent the loci of constant n_{tot} and varying E, while diagonals of constant $C_{BG}V_{BG} - C_{BG}V_{BG}$ define the loci of constant E at varying n_{tot}. The diagonal of n_{tot} = 0 is defined by the points of maximum ρ_{xx} measured as a function of V_{TG} at fixed V_{BG} values. In order to determine the V_{TG} and V_{BG} values at which n_{tot} = 0 and E = 0, we consider ρ_{xx} measured along the diagonal n_{tot} = 0. The ρ_{xx} shows a minimum and increases markedly on both sides, thanks to the transverse electric field induced band-gap opening [18, 19, 84]. The minimum ρ_{xx} on the n_{tot} = 0 diagonal defines the E = 0 point. Having established a correspondence between (V_{TG}, V_{BG}) and (n_{tot}, E), we characterize the bilayers in terms of n_{tot} and E in the remainder.

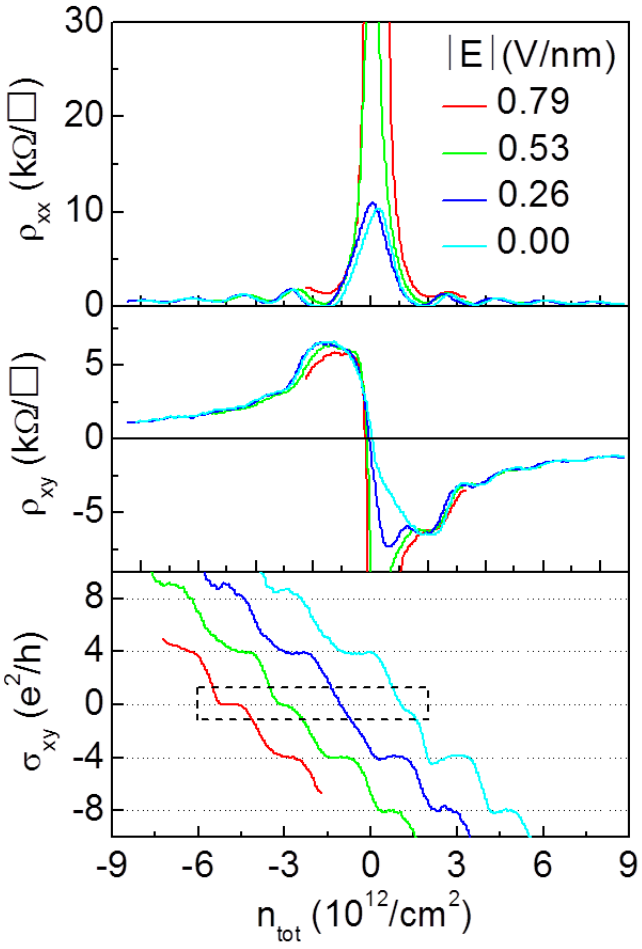

Figure 5.4: (a) ρ_{xx} vs n_{tot}, and (b) ρ_{xy} vs n_{tot} measured at B = 18 T and T = 0.3 K, for different E field values in sample K24. (c) σ_{xy} vs n_{tot} corresponding to panels (a, b) data, at different E values, and at B = 18 T and T = 0.3 K. The traces are shifted horizontally for clarity. Adapted from Ref.[9].

5.3.2 Quantum Hall Effects in dual-gated graphene bilayers

In Figure 5.4(a) and (b), we show ρ_{xx} vs n_{tot} and ρ_{xy} vs n_{tot}, respectively, measured at fixed E field values, at B = 18 T and T = 0.3 K in sample K24. These data are measured by simultaneously sweeping V_{TG} and V_{BG}, such that E remains constant. The data show QHSs marked by vanishing ρ_{xx} at integer filling factors multiple of four, consistent with the four-fold degeneracy associated with spin and valley of each Landau level [8, 21]. Using the measured ρ_{xx} and ρ_{xy}, we determine the Hall conductivity (σ_{xy}) via a tensor inversion, σ_{xy}=$\rho_{xy}/(\rho_{xx}^2+\rho_{xy}^2)$. Figure 5.4(c) data show σ_{xy} vs n_{tot}, measured at B = 18 T and T = 0.3 K, and for different values of E. Figure 5.4(a) data show an increasing ρ_{xx} at $n_{tot} = 0$ with increasing E, translating into a Hall conductivity plateau at $\sigma_{xy} = 0$ [Figure 5.4(c)], which signals a developing QHS at $\nu = 0$ at large E.

The $\nu = 0$ QHS in graphene bilayers at large E fields is explained as follows. In an applied perpendicular B field the energy spectrum consists of the four-fold spin and valley degenerate LLs. At E = 0 an eightfold degenerate LL, i.e., the spin and valley degenerate N = 0 and N = 1 LLs, exists at zero energy, $\varepsilon = 0$, the electron-hole symmetry point [8, 21]. The N = 0 and N = 1 LL wave functions are layer polarized, and can be indexed by the layer degree of freedom, in addition to spin. In an applied transverse E field the eightfold degenerate LL at $\varepsilon = 0$ splits into two four-fold degenerate LLs, separated by the same energy gap (Δ), which exists between the electron and hole bands at B = 0 [83, 89]. The higher (lower) energy LLs correspond to the spin degenerate N = 0 and N = 1 LLs residing in the layer with higher (lower) on-site energy.

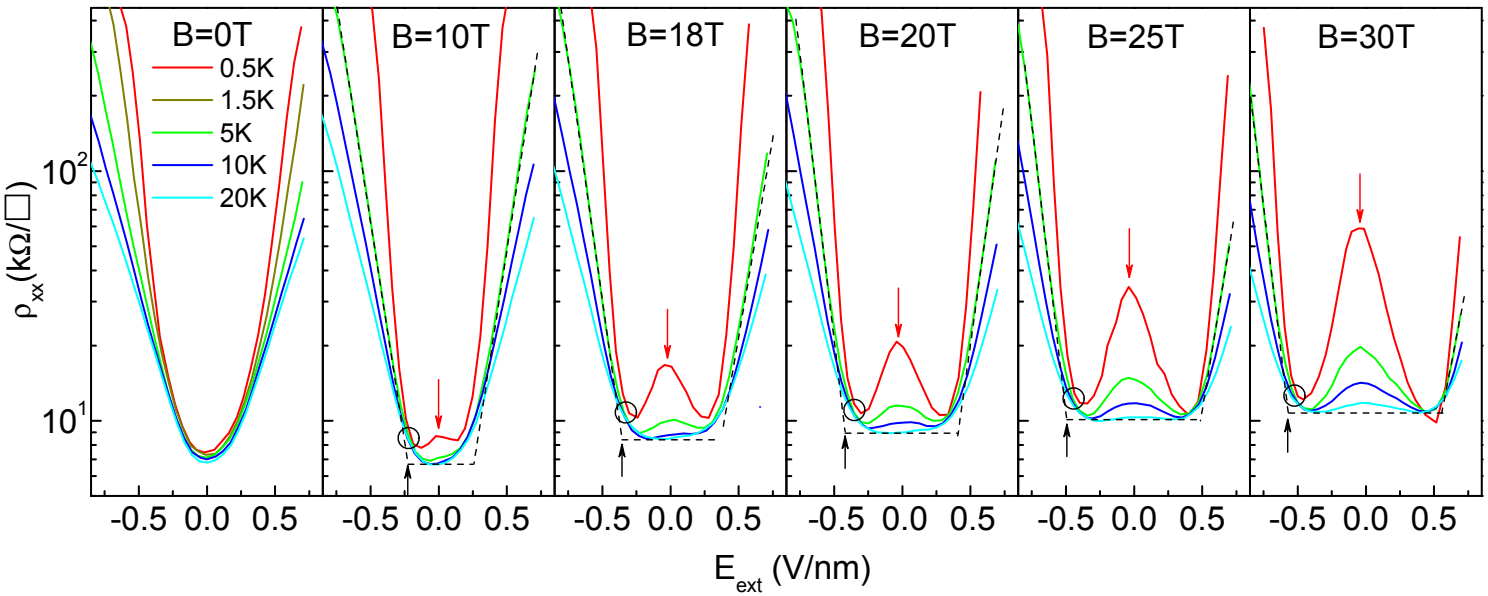

Figure 5.5: ρ_{xx} vs E measured at $n_{tot} = 0$ ($\nu = 0$) at different values of the perpendicular B field, and temperature. At B = 0, ρ_{xx} shows an exponential dependence on E, as well as an insulating behavior at finite E, a consequence of the E field induced band-gap opening in the bilayer. In a perpendicular B field, the onset of the exponential dependence of ρ_{xx} vs E (black arrow), which marks the E field induced splitting of the LLs at $\varepsilon = 0$, increases with the B field. As the B field increases, ρ_{xx} vs T shows an insulating state centered at E = 0, indicating a developing $\nu = 0$ QHS at E = 0 (red arrow). Adapted from Ref.[9].

Figure 5.5 data show ρ_{xx} vs E measured at different T values, at $n_{tot} = 0$. The data are collected by sweeping V_{TG} and V_{BG} in opposite directions, with sweep rates proportional to C_{TG}, and C_{BG}, respectively. At B = 0, the ρ_{xx} shows a nearly exponential increase with E, combined with an insulating behavior, a consequence of the E field induced band-gap opening. The T dependence of the ρ_{xx} is weaker than the exponential, $\propto e^{\Delta/2k_BT}$, expected for a band insulator, and instead follows more closely a $\propto e^{(T_0/T)^{1/3}}$ dependence, attributed to variable range hopping between disorder-induced states in the gap [90, 91].

In a perpendicular magnetic field, the ρ_{xx} vs E data also show an exponential divergence at finite E values, consistent with the E field induced splitting of the = 0 LLs. However, a closer examination of the ρ_{xx} vs E data in high B fields reveals an interesting trend. Let us first consider Figure 5.5 data collected at the highest temperature, T = 20 K. Unlike the B = 0 case, the onset of the ρ_{xx} divergence occurs at a finite E field, which also increases with B, indicating the E field induced LL splitting is suppressed for small transverse E fields. This observation is a direct consequence of the N = 0 and N = 1 LLs being layer polarized. Let us assume the transverse E field is applied such that the on-site energy of electrons of the top layer is higher than that on the bottom layer. At filling factor $\nu = 0$ the N = 0 and N = 1 LLs of the bottom layer will be fully occupied, while the N = 0 and N = 1 LLs of the top layer will be empty. Such LL occupancy will innately place more electrons in the bottom layer, setting up an internal electric field which opposes the externally applied E field. The magnitude of the internal electric field is related to the LL degeneracy as

$$E_{int} = (\frac{4e^2}{h}B)/2\epsilon_0. \quad (5.1)$$

Further examination of Figure 5.5 data reveals another interesting finding. In high B fields, ρ_{xx} shows an insulating state centered at E = 0, which becomes more pronounced with increasing the B field. This signals a splitting of the $\varepsilon = 0$ LLs, and consequently a developing $\nu = 0$ QHS at E = 0, which is attributed to the spin splitting of the N = 0 and N = 1 LLs. As the E field increases, ρ_{xx} decreases, and the insulating state weakens. At a fixed B field, the ρ_{xx} vs E data show a temperature-independent minimum at a critical field E_c. For fields higher than E_c, the ρ_{xx} shows a diverging dependence on E, a consequence of the E field induced splitting of the N = 0 and N = 1 LLs. The E_c field marks a transition at $\nu = 0$, from a spin-polarized QHS at small E fields to a valley(layer)-polarized QHS at large E fields, in agreement with several recent theoretical studies which examined the $\nu = 0$ phase diagram as a function of transverse E field, and considering the electron-electron interaction [92–94]. We remark that the ρ_{xx} vs E data in Figure 5.5 are symmetric for both negative and positive E fields, which indicates the disorder in both layers is similar.

Figure 5.6(a) shows qualitatively the expected dependence of the N = 0 and N = 1 LL energies on the E field. In the absence of spin splitting [Figure 5.6(a), left panel], the LL layer degree of freedom remains degenerate at finite E field, owing to the LL layer polarization. In the presence of spin splitting [Figure 5.6(a), right panel], the spin down LLs of both layers are occupied, while the spin up LLs are empty. An applied E field increases (reduces) the energy of the top (bottom) layer LLs, which cross at a field Ec. Figure 5.6(b) data summarize the E_c vs B data measured for three samples, marked by different symbols. We employ two criteria to define E_c using

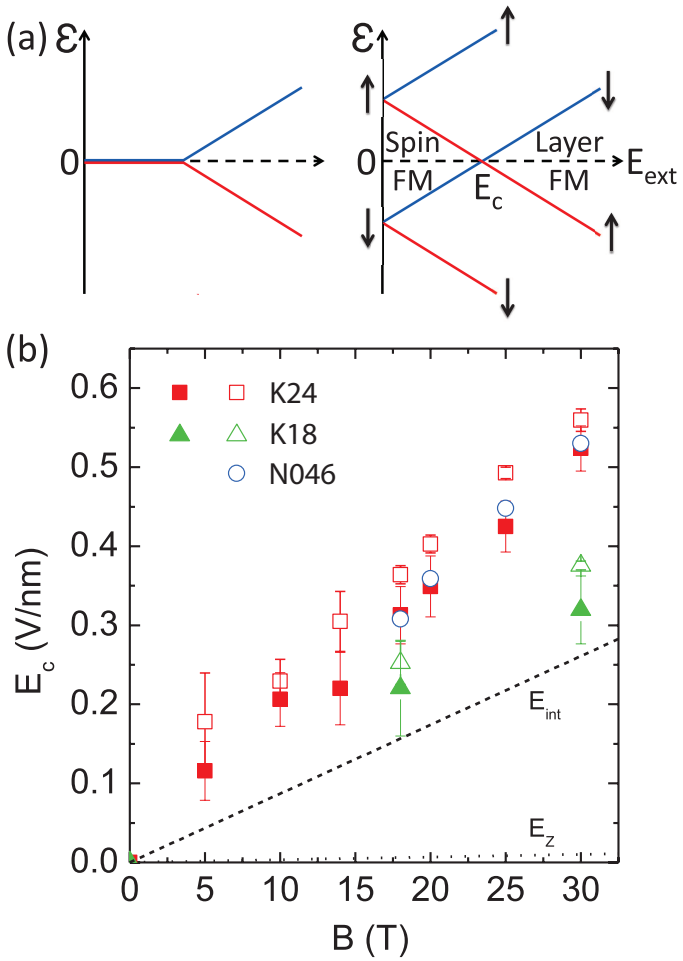

Figure 5.6: (a) LL energy vs E dependence neglecting (left panel) and including (right panel) the electron spin. The light (red) and dark (blue) lines denote the LLs corresponding to the bottom and top layer, respectively. In the absence of spin splitting, the LLs at $\varepsilon = 0$ remain degenerate owing to layer polarization (left panel). When spin (Zeeman) splitting is considered, the $\nu = 0$ QHS undergoes a transition at a critical electric field (E_c) from spin polarized at small E to layer (valley) polarized at large E. (b) E_c vs B measured in three different samples. The dashed and dotted lines represent E_{int} and E_Z calculated using Equation 5.1, respectively. Adapted from Ref.[9].

Figure 5.5 data. The open symbols in Figure 5.6(b) indicate the onset of the ρ_{xx} divergence at high E fields, shown as black arrows in Figure 5.5. The closed symbols in Figure 5.6(b) represent the E fields at which ρ_{xx} is temperature-independent, and are marked by circles in Figure 5.5. Both criteria yield similar E_c values, with slightly higher values for the first criterion. It is instructive to compare the experimental E_c values with two simple calculations. The first is the electric field (E_{int}) required to split the N = 0, 1 LLs when the layer polarization is taken into account [Equation 5.1]. The second is the electric field E_Z at which the electron Zeeman energy (Δ_Z) is equal to the on-site energy difference between the layers:

$$E_Z = g\mu_B B/d. \tag{5.2}$$

The E_Z values calculated assuming a g factor of 2, and an interlayer distance d = 3.4 Å, are represented by the dotted trace in Figure 5.6(b); μ_B is the Bohr magneton. Neglecting interaction, the $\nu = 0$ QHS undergoes a transition from spin to valley polarized at an E field equal to E_Z. Examination of Figure 5.6 data shows that E_c is much larger than E_Z, and comparable albeit larger than E_{int}.

We discuss the role of Zeeman splitting on the spin-to-valley-polarized transition. Using ρ_{xx} vs E at different B fields, measured at a $48^{\circ\,\mathrm{deg}}$ angle between the normal to the sample plane and the magnetic field, we extracted a set of E_c vs B values similar to Figure 5.6(b) data, but with a 1.5 times larger Zeeman splitting. We find that the $E_c$values remain independent of the in-plane component of the magnetic field, and are determined only by the B field perpendicular to the sample.

Last, one question arises with the exfoliated graphene bilayers is whether the

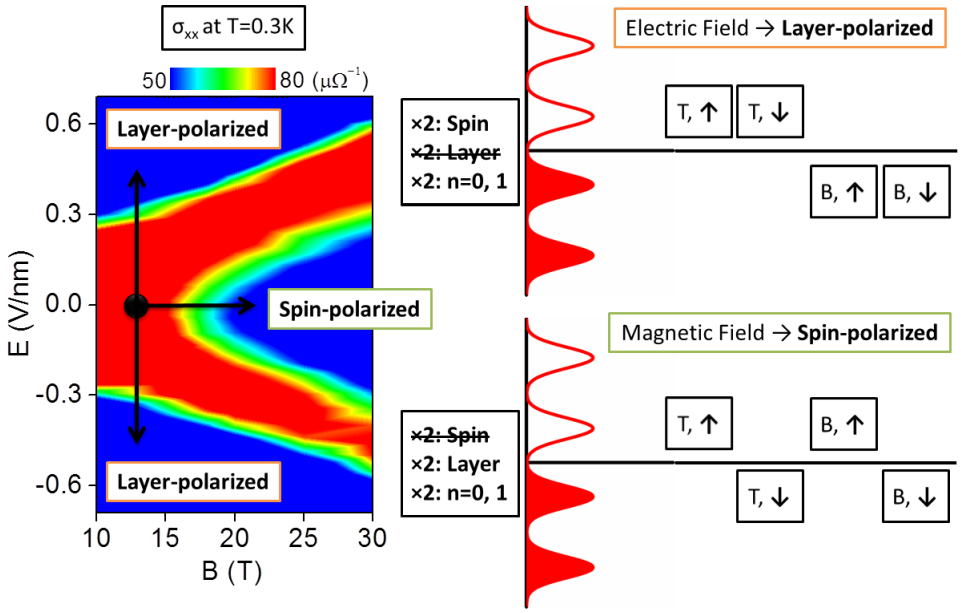

Figure 5.7: Contour plot of σ_{xx} in B and E field plane measured at $\varepsilon = 0$ and T = 0.3 K (left panel). The color map is chosen to exaggerate the boundary between the insulating states with different symmetry breaking mechanisms. The regions of the layer-polarized and spin-polarized QHSs are clearly captured. The gap opening at each polarization case and possible mechanism are illustrated in the right panel, where T(B) stands for the top (bottom) layer in a graphene AB-bilayer and up or down arrows indicate corresponding spin directions, respectively.

edges of the graphene flake are homogeneously bilayer or not. It is plausible that the two layers may not necessarily terminate at the same position, leading to single layer edge states and consequently single layer-like magnetotransport in high magnetic fields. To test if the edge states affects Figure 5.5 and 5.5 data, we probed both as exfoliated samples (K24), and samples (K18, N046) where an O_2 plasma etch was used to pattern Hall bars, and where both layers terminate at the same position.

The main finding in this study is summarized in Figure 5.7, which shows the contour plot of σ_{xx} in B and E field plane at $\varepsilon = 0$ and T = 0.3 K (left panel) and illustration of valley-polarized and spin-polarized QHSs (right panel). The blue area in the left panel of Figure 5.7 indicates the low σ_{xx} region, equivalently high ρ_{xx} region, where a $\nu = 0$ QHS develops due to the symmetry breaking. The regions of high conductance (red area in the left panel of Figure 5.7) mark the transition between the low and high E field $\nu = 0$ QHSs. The layer-polarized phase is stabilized at high E fields and spin-polarized phase at high B fields, which is consistent with our discussion about the different mechanisms of broken symmetry phases. The linear dependence of E_c on B field is clearly visible in Figure 5.7.

Several theory groups studied the spin-to-valley polarized transition at $\nu = 0$ in graphene bilayers. Gorbar, Gusynin, and Miransky [92] predict a first-order phase transition from spin to valley polarized at an E field of $\cong 1$ mV/nm $\times$ B [T] . A similar linear E_c vs B dependence is found in two other studies [93, 94], but at a larger E_c field, of $\cong 9$ mV/nm $\times$ B [T] . Töke and Falḱo [94] suggest an intermediate, compressible phase between the spin- and valley-polarized $\nu = 0$ QHSs, with the spin-polarized phase collapsing at relatively small electric fields. Figure 5.5 data show that the spin-polarized phase remains gapped at all fields except for in the vicinity of E_c. A closely

similar system to the $\nu = 0$ QHS in graphene bilayers is the $\nu = 2$ QHS in double layer GaAs/AlGaAs heterostructures [95]. Depending on the balance between the Zeeman energy, on-site layer energy difference (Δ), and the tunneling energy (Δ_t), the $\nu = 2$ QHS can be either spin or layer polarized, with an intermediate canted spin phase [96, 97]. The Hartree-Fock theory of the $\nu = 2$ QHS [97] shows a first-order transition from spin to layer polarized when the exchange energy equals the direct (Hartree) energy, a limit reached when d is much smaller than the magnetic length ($l_B = \sqrt{h/eB}$). The $d \ll l_B$ is satisfied up to the highest magnetic fields here, as $d = l_B = 0.07$ at B = 30 T, rendering the $\nu = 0$ QHS in graphene AB bilayers equivalent with the $\nu = 2$ QHS in double quantum wells, in the limit of zero tunneling ($\Delta_t = 0$), and small Zeeman energy (Δ_Z). Interestingly, the $d/l_B \cong 0$ limit in GaAs double quantum wells cannot be reached because of limitations associated with finite well and barrier widths, finite tunneling, and carrier density.

A similar transition at $\nu = 0$ as a function of transverse electric field was reported in dual-gated, suspended graphene bilayers [98]. Weitz *et al.* probed at much lower E fields and up to 5.5 T and also in single-gated, supported graphene bilayers formed on SiC [22]. Although the sample mobilities, the range of E fields, and magnetic fields explored in Ref.[98] are very different, remarkably the linear E_c vs B dependence is in good agreement with the results of this study.

5.4 Conclusion

In summary, the $\nu = 0$ QHS in dual-gated graphene bilayers in a high magnetic field reveals two regimes: at E = 0, as a result of the spin splitting, and at large E fields

when the system is layer polarized. The $\nu = 0$ QHS undergoes a transition from spin- to valley(layer)-polarized QHS at a critical electric field (E_c), which depends linearly on B, with a slope of $12 - 18$ $(\mathrm{mV/nm})\,\mathrm{T}^{-1}$. Our data, interpreted in the framework of existing theories, suggest the exchange and direct energies are comparable at zero filling factor.

Chapter 6

Conclusion

6.1 Summary

In this dissertation we discussed the realization of graphene double layer heterostructures, where we observed interesting magnetotransport and Coulomb drag phenomena. Key breakthroughs in fabrication techniques such as dielectric deposition technique on graphene and graphene transfer process, which enabled the advanced graphene double layer structures, were described in detail. The simple dielectric deposition technique provided an ultra-thin and highly insulating interlayer insulator in double layer graphene devices. Precise and damage-free graphene transfer and alignment technique was also crucial to the realization of double layer graphene devices. We extended our understanding of the system by proposing a model to explain layer density and resistivity dependence on applied gate biases, which showed an excellent agreement with the experiments. In this graphene double layer system, we measured the Coulomb drag in graphene for the first time, and studied carrier type, temperature and density dependence of the drag resistivity. The history and physics of this interlayer electron-electron interaction induced phenomena were studied in detail. At low temperatures, the drag resistance featured random and giant fluctuations superposed on the average drag signal as a signature of macroscopic-to-mesoscopic transition. The possible mechanism of the fluctuations were examined and compared

with our results. We also introduced a method to measure the relative Fermi energy as a function of layer density in one layer of the double layer system by employing the opposite graphene layer as a charge detection sensor. We demonstrated the method by measuring the Fermi energy in graphene at zero and high magnetic fields. Lastly, we fabricated dual-gated bilayer graphene devices and investigated quantum Hall effects and broken symmetry states in the system. The zero energy Landau levels in graphene bilayer are known to be eight-fold degenerate, and theoretical study showed that the degeneracy can be lifted upon applying transverse electric field and perpendicular magnetic field. We focused on the $\nu = 0$ quantum Hall state and observed a gap opening at large electric fields and in high magnetic fields, which is explained by broken spin and valley spin symmetry in the zero energy Landau levels.

6.2 Future Work

One future research effort could be further exploration of a signature of electron-hole pairing in the independently contacted graphene double layer system using the Coulomb drag measurement and/or interlayer tunneling current measurement as a probing tool will be interesting. To date we have not observed a clear evidence of electron-hole condensation in our double layer system. Multiple device and measurement parameters need to be tuned in order to find the optimal condition at which electron-hole pairing may be observed: device parameters such as spacing between layers, d, and dielectric constant of the interlayer dielectric, κ, and measurement parameters such as charge carrier density in each layer, n_B and n_T, and measurement temperature, T. The range of parameters we have explored are summarized in Figure

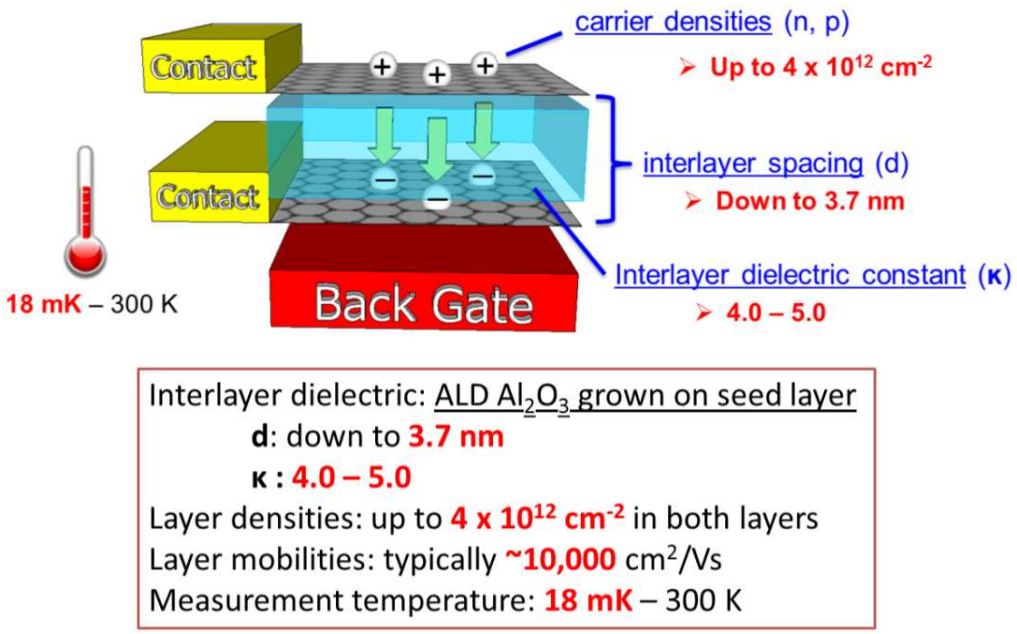

Figure 6.1: Schematic of a graphene double layer system, and various experimental parameters we have investigated to observe electron-hole pairing.

6.1.

The best and ultimate device structure to search for electron-hole pairs in graphene double layers will be suspended double layer structures, where both graphene layers are levitated but still in very close proximity. This structure will guarantee the highest mobility in both layers [99] and ideal low-κ environment [100] to minimize the extrinsic screening of the medium embedding the layers. The fabrication process to achieve levitated double graphene layers, placed in only 1-2 nm apart [101] while not touching to each other, is by no means trivial. Also if realized, extreme care during the measurement must be taken. However, there is no fundamental limitation to fabricate this structure. Transitional device structures such as air-gapped double layer with no interlayer dielectric, and partially or singly suspended graphene double

layers will provide good testbeds for this formidable, but interesting challenge. The fabrication of top gate will widen the layer density range one can explore by reducing the excessive electric field applied across the ultra-thin interlayer dielectric.

Further investigation of the Coulomb drag in graphene double layers will be useful. While our data showed a qualitative agreement with the existing theory, the amount of experimental data obtained is still limited due to the technical reasons: tremendous time required to collect the small-scale Coulomb drag signals without noise and with high resolution in the wide range of layer densities, at various temperatures. More experimental data to validate the observed behavior and to explain other effects originating from different drag mechanisms still remain to be established. Efforts for quantitative explanation of the average drag resistivity and fluctuations will also be worthwhile.

The idea of using a graphene layer as a gate and charge sensor to measure the Fermi energy of the underlying electron system can be extended into various practical applications. If one builds a system with a movable and suspended graphene tip with two contacts, it can function as a scanning Kelvin probe system to measure surface potential with spatial resolution only limited by the size of the graphene. This system can also be used to measure the Coulomb drag and excitonic condensation if the surface of a suspended graphene device can be scanned by the graphene tip. The interlayer distance can be tuned as one desires. In transport measurements, if a graphene gate is deposited instead of a metal gate, one can apply electric field to the channel of interest and measure the Fermi energy of the channel at the same time using the graphene gate: we can certainly call it as a *graphene smart gate*.

References

[1] S. Das Sarma, Shaffique Adam, E. H. Hwang, and Enrico Rossi. Electronic transport in two-dimensional graphene. *Rev. Mod. Phys.*, 83:407–470, May 2011.

[2] S. K. Banerjee, L. F. Register, E. Tutuc, D. Reddy, and A. H. MacDonald. Bilayer PseudoSpin Field-Effect Transistor (BiSFET): A Proposed New Logic Device. *Electron Device Letters, IEEE*, 30(2):158–160, 2009.

[3] Seyoung Kim, Insun Jo, Junghyo Nah, Z. Yao, S. K. Banerjee, and E. Tutuc. Coulomb drag of massless fermions in graphene. *Physical Review B*, 83(16):161401, 2011.

[4] Seyoung Kim, Insun Jo, D. C. Dillen, D. A. Ferrer, B. Fallahazad, Z. Yao, S. K. Banerjee, and E. Tutuc. Direct Measurement of the Fermi Energy in Graphene Using a Double-Layer Heterostructure. *Phys. Rev. Lett.*, 108(11):116404, 2012.

[5] N. M. R. Peres and et al. Coulomb drag and high-resistivity behavior in double-layer graphene. *EPL (Europhysics Letters)*, 95(1):18001, 2011.

[6] K. Das Gupta, A. F. Croxall, J. Waldie, C. A. Nicoll, H. E. Beere, I. Farrer, D. A. Ritchie, and M. Pepper. Experimental Progress towards Probing the Ground State of an Electron-Hole Bilayer by Low-Temperature Transport. *Advances in Condensed Matter Physics*, 2011, 2011.

[7] Adam S. Price. Coulomb Drag, Mesoscopic Physics, and Electron-Electron Interactions. *Ph.D. Dissertation*, 2008.

[8] K. S. Novoselov, E. McCann, S. V. Morozov, V. I. Fal/'ko, M. I. Katsnelson, U. Zeitler, D. Jiang, F. Schedin, and A. K. Geim. Unconventional quantum Hall effect and Berry's phase of 2π in bilayer graphene. *Nat Phys*, 2(3):177–180, 2006.

[9] Seyoung Kim, Kayoung Lee, and E. Tutuc. Spin-Polarized to Valley-Polarized Transition in Graphene Bilayers at $\nu = 0$ in High Magnetic Fields. *Phys. Rev. Lett.*, 107(1):016803, 2011.

[10] K. S. Novoselov, A. K. Geim, S. V. Morozov, D. Jiang, Y. Zhang, S. V. Dubonos, I. V. Grigorieva, and A. A. Firsov. Electric Field Effect in Atomically Thin Carbon Films. *Science*, 306(5696):666–669, 2004.

[11] Andre K. Geim. Graphene Update. *American Physical Society March Meeting 2012*, Mar 2012.

[12] Jian-Hao Chen, Chaun Jang, Shudong Xiao, Masa Ishigami, and Michael S. Fuhrer. Intrinsic and extrinsic performance limits of graphene devices on SiO_2. *Nat Nano*, 3(4):206–209, 2008.

[13] Andrea F. Young and Philip Kim. Quantum interference and Klein tunnelling in graphene heterojunctions. *Nat Phys*, 5(3):222–226, 2009.

[14] K. S. Novoselov, A. K. Geim, S. V. Morozov, D. Jiang, M. I. Katsnelson, I. V. Grigorieva, S. V. Dubonos, and A. A. Firsov. Two-dimensional gas of massless Dirac fermions in graphene. *Nature*, 438(7065):197–200, 2005.

[15] Yu-Ming Lin, Keith A. Jenkins, Alberto Valdes-Garcia, Joshua P. Small, Damon B. Farmer, and Phaedon Avouris. Operation of Graphene Transistors at Gigahertz Frequencies. *Nano Letters*, 9(1):422–426, 2009.

[16] Shaffique Adam, E. H. Hwang, V. M. Galitski, and S. Das Sarma. A self-consistent theory for graphene transport. *Proceedings of the National Academy of Sciences*, 104(47):18392–18397, 2007.

[17] Seyoung Kim, Junghyo Nah, Insun Jo, Davood Shahrjerdi, Luigi Colombo, Zhen Yao, Emanuel Tutuc, and Sanjay K. Banerjee. Realization of a high mobility dual-gated graphene field-effect transistor with Al_2O_3 dielectric. *Applied Physics Letters*, 94(6):062107, 2009.

[18] Hongki Min, Bhagawan Sahu, Sanjay K. Banerjee, and A. H. MacDonald. *Ab initio* theory of gate induced gaps in graphene bilayers. *Phys. Rev. B*, 75:155115, Apr 2007.

[19] Edward McCann. Asymmetry gap in the electronic band structure of bilayer graphene. *Phys. Rev. B*, 74:161403, Oct 2006.

[20] Fengnian Xia, Damon B. Farmer, Yu-ming Lin, and Phaedon Avouris. Graphene Field-Effect Transistors with High On/Off Current Ratio and Large Transport Band Gap at Room Temperature. *Nano Letters*, 10(2):715–718, 2010.

[21] Edward McCann and Vladimir I. Fal'ko. Landau-Level Degeneracy and Quantum Hall Effect in a Graphite Bilayer. *Phys. Rev. Lett.*, 96:086805, Mar 2006.

[22] Kayoung Lee, Seyoung Kim, M. S. Points, T. E. Beechem, Taisuke Ohta, and E. Tutuc. Magnetotransport Properties of Quasi-Free-Standing Epitaxial Graphene Bilayer on SiC: Evidence for Bernal Stacking. *Nano Letters*, 11(9):3624–3628, 2011.

[23] M. Nonnenmacher, M. P. Oboyle, and H. K. Wickramasinghe. Kelvin probe force microscopy. *Applied Physics Letters*, 58(25):2921–2923, 1991.

[24] J. A. Seamons, C. P. Morath, J. L. Reno, and M. P. Lilly. Coulomb Drag in the Exciton Regime in Electron-Hole Bilayers. *Phys. Rev. Lett.*, 102(2):026804, 2009.

[25] J. P. Eisenstein and A. H. MacDonald. Bose-Einstein condensation of excitons in bilayer electron systems. *Nature*, 432(7018):691–694, 2004.

[26] Y.E. Lozovik and V.I. Yudson. Feasibility of superfluidity of paired spatially separated electrons and holes; a new superconductivity mechanism. *JETP Lett.*, 22(11):274–276, 1975.

[27] M. Pohlt, M. Lynass, J. G. S. Lok, W. Dietsche, K. v. Klitzing, K. Eberl, and R. Muhle. Closely spaced and separately contacted two-dimensional electron and hole gases by in situ focused-ion implantation. *Applied Physics Letters*, 80(12):2105–2107, 2002.

[28] A. F. Croxall, K. Das Gupta, C. A. Nicoll, M. Thangaraj, H. E. Beere, I. Farrer, D. A. Ritchie, and M. Pepper. Anomalous Coulomb Drag in Electron-Hole Bilayers. *Phys. Rev. Lett.*, 101(24):246801, 2008.

[29] A. K. Geim and K. S. Novoselov. The rise of graphene. *Nat. Mater.*, 6(3):183–191, 2007.

[30] Hongki Min, Rafi Bistritzer, Jung-Jung Su, and A. H. MacDonald. Room-temperature superfluidity in graphene bilayers. *Physical Review B (Condensed Matter and Materials Physics)*, 78(12):121401, 2008.

[31] C.-H. Zhang and Yogesh N. Joglekar. Excitonic condensation of massless fermions in graphene bilayers. *Phys. Rev. B*, 77:233405, Jun 2008.

[32] P. Blake, E. W. Hill, A. H. Castro Neto, K. S. Novoselov, D. Jiang, R. Yang, T. J. Booth, and A. K. Geim. Making graphene visible. *Applied Physics Letters*, 91(6):063124, 2007.

[33] Y. Xuan, Y. Q. Wu, T. Shen, M. Qi, M. A. Capano, J. A. Cooper, and P. D. Ye. Atomic-layer-deposited nanostructures for graphene-based nanoelectronics. *Applied Physics Letters*, 92(1):013101, 2008.

[34] B. Lee, G. Mordi, M. J. Kim, Y. J. Chabal, E. M. Vogel, R. M. Wallace, K. J. Cho, L. Colombo, and J. Kim. Characteristics of high-k Al[sub 2]O[sub 3] dielectric using ozone-based atomic layer deposition for dual-gated graphene devices. *Applied Physics Letters*, 97(4):043107, 2010.

[35] Xinran Wang, Scott M. Tabakman, and Hongjie Dai. Atomic Layer Deposition of Metal Oxides on Pristine and Functionalized Graphene. *J. Am. Chem. Soc.*, 130(26):8152–8153, 2008.

[36] Inanc Meric, Melinda Y. Han, Andrea F. Young, Barbaros Ozyilmaz, Philip Kim, and Kenneth L. Shepard. Current saturation in zero-bandgap, top-gated graphene field-effect transistors. *Nat Nano*, 3(11):654–659, 2008.

[37] J. R. Williams, L. DiCarlo, and C. M. Marcus. Quantum Hall Effect in a Gate-Controlled p-n Junction of Graphene. *Science*, 317(5838):638–641, 2007.

[38] Alfonso Reina, Hyungbin Son, Liying Jiao, Ben Fan, Mildred S. Dresselhaus, ZhongFan Liu, and Jing Kong. Transferring and Identification of Single- and Few-Layer Graphene on Arbitrary Substrates. *The Journal of Physical Chemistry C*, 112(46):17741–17744, 2008.

[39] J. Martin, N. Akerman, G. Ulbricht, T. Lohmann, J. H. Smet, K. von Klitzing, and A. Yacoby. Observation of electron-hole puddles in graphene using a scanning single-electron transistor. *Nat Phys*, 4(2):144–148, 2008.

[40] Young-Jun Yu, Yue Zhao, Sunmin Ryu, Louis E. Brus, Kwang S. Kim, and Philip Kim. Tuning the Graphene Work Function by Electric Field Effect. *Nano Letters*, 9(10):3430–3434, 2009.

[41] Serge Luryi. Quantum capacitance devices. *Applied Physics Letters*, 52(6):501–503, 1988.

[42] J. H. Chen, C. Jang, S. Adam, M. S. Fuhrer, E. D. Williams, and M. Ishigami. Charged-impurity scattering in graphene. *Nat Phys*, 4(5):377–381, 2008.

[43] S. Droscher, P. Roulleau, F. Molitor, P. Studerus, C. Stampfer, K. Ensslin, and T. Ihn. Quantum capacitance and density of states of graphene. *Applied Physics Letters*, 96(15):152104, 2010.

[44] Jilin Xia, Fang Chen, Jinghong Li, and Nongjian Tao. Measurement of the quantum capacitance of graphene. *Nat Nano*, 4(8):505–509, 2009.

[45] M. B. Pogrebinskii. Mutual Drag of Carriers in a Semiconductor-insulator-semiconductor System. *Soviet Physics Semiconductors-Ussr*, 11(4):372–376, 1977.

[46] P. M. Price. Hot electron effects in heterolayers. *Physica B*, 117:750, 1983.

[47] Kurt Hubner and William Shockley. Transmitted Phonon Drag Measurements in Silicon. *Phys. Rev. Lett.*, 4(10):504–505, 1960.

[48] P. M. Solomon, P. J. Price, D. J. Frank, and D. C. La Tulipe. New phenomena in coupled transport between 2D and 3D electron-gas layers. *Phys. Rev. Lett.*, 63(22):2508, 1989.

[49] T. J. Gramila, J. P. Eisenstein, A. H. MacDonald, L. N. Pfeiffer, and K. W. West. Mutual friction between parallel two-dimensional electron systems. *Phys. Rev. Lett.*, 66(9):1216, 1991.

[50] U. Sivan, P. M. Solomon, and H. Shtrikman. Coupled electron-hole transport. *Phys. Rev. Lett.*, 68(8):1196–1199, 1992.

[51] Antti-Pekka Jauho and Henrik Smith. Coulomb drag between parallel two-dimensional electron systems. *Physical Review B*, 47(8):4420, 1993.

[52] D. L. Maslov. Mutual drag of two- and three-dimensional electron gases: A collective-collisions approach. *Physical Review B*, 45(4):1911–1914, 1992.

[53] Karsten Flensberg, Ben Yu-Kuang Hu, Antti-Pekka Jauho, and Jari M. Kinaret. Linear-response theory of Coulomb drag in coupled electron systems. *Physical Review B*, 52(20):14761–14774, 1995.

[54] Alex Kamenev and Yuval Oreg. Coulomb drag in normal metals and superconductors: Diagrammatic approach. *Physical Review B*, 52(10):7516–7527, 1995.

[55] Lian Zheng and A. H. MacDonald. Coulomb drag between disordered two-dimensional electron-gas layers. *Physical Review B*, 48(11):8203–8209, 1993.

[56] M. I. Katsnelson. Coulomb drag in graphene single layers separated by a thin spacer. *Physical Review B*, 84(4):041407, 2011.

[57] Wang-Kong Tse and S. Das Sarma. Coulomb drag and spin drag in the presence of spin-orbit coupling. *Physical Review B*, 75(4):045333, 2007.

[58] M. Carrega, T. Tudorovskiy, A. Principi, M. I. Katsnelson, and Marco Polini. Theory of Coulomb drag for massless Dirac fermions. *arXiv.org*, page 1203.3386v1, 2012.

[59] E. H. Hwang, Rajdeep Sensarma, and S. Das Sarma. Coulomb drag in monolayer and bilayer graphene. *Physical Review B*, 84(24):245441, 2011.

[60] I. V. Gornyi P. M. Ostrovsky B. N. Narozhny, M. Titov. Coulomb drag in graphene: perturbation theory. *arXiv.org*, page 1110.6359, 2011.

[61] B. N. Narozhny, Gábor Zala, and I. L. Aleiner. Interaction corrections at intermediate temperatures: Dephasing time. *Physical Review B*, 65(18):180202,

2002. PRB.

[62] P. A. Lee, A. Douglas Stone, and H. Fukuyama. Universal conductance fluctuations in metals: Effects of finite temperature, interactions, and magnetic field. *Physical Review B*, 35(3):1039–1070, 1987.

[63] J. Berezovsky and et al. Imaging coherent transport in graphene (part I): mapping universal conductance fluctuations. *Nanotechnology*, 21(27):274013, 2010.

[64] A. S. Price, A. K. Savchenko, B. N. Narozhny, G. Allison, and D. A. Ritchie. Giant Fluctuations of Coulomb Drag in a Bilayer System. *Science*, 316(5821):99–102, 2007.

[65] Clark R. Landis and Frank Weinhold. Origin of Trans-Bent Geometries in Maximally Bonded Transition Metal and Main Group Molecules. *Journal of the American Chemical Society*, 128(22):7335–7345, 2006.

[66] A. S. Price, A. K. Savchenko, B. N. Narozhny, G. Allison, and D. A. Ritchie. Giant Fluctuations of Coulomb Drag in a Bilayer System. *Science*, 316(5821):99–102, 2007.

[67] B. N. Narozhny and I. L. Aleiner. Mesoscopic Fluctuations of the Coulomb Drag. *Phys. Rev. Lett.*, 84:5383–5386, Jun 2000.

[68] E. Gornik, R. Lassnig, G. Strasser, H. L. Störmer, A. C. Gossard, and W. Wiegmann. Specific Heat of Two-Dimensional Electrons in GaAs-GaAlAs Multilayers. *Phys. Rev. Lett.*, 54:1820–1823, Apr 1985.

[69] J. K. Wang, D. C. Tsui, M. Santos, and M. Shayegan. Heat-capacity study of two-dimensional electrons in GaAs/$Al_xGa_{1-x}As$ multiple-quantum-well structures in high magnetic fields: Spin-split Landau levels. *Phys. Rev. B*, 45:4384–4389, Feb 1992.

[70] J. P. Eisenstein, H. L. Stormer, V. Narayanamurti, A. Y. Cho, A. C. Gossard, and C. W. Tu. Density of States and de Haas-van Alphen Effect in Two-Dimensional Electron Systems. *Phys. Rev. Lett.*, 55(8):875–878, 1985.

[71] T. P. Smith, B. B. Goldberg, P. J. Stiles, and M. Heiblum. Direct measurement of the density of states of a two-dimensional electron gas. *Physical Review B*, 32(4):2696–2699, 1985.

[72] J. P. Eisenstein, L. N. Pfeiffer, and K. W. West. Compressibility of the two-dimensional electron gas: Measurements of the zero-field exchange energy and fractional quantum Hall gap. *Physical Review B*, 50(3):1760–1778, 1994.

[73] E. A. Henriksen and J. P. Eisenstein. Measurement of the electronic compressibility of bilayer graphene. *Physical Review B*, 82(4):041412, 2010.

[74] A. F. Young, C. R. Dean, I. Meric, S. Sorgenfrei, H. Ren, K. Watanabe, T. Taniguchi, J. Hone, K. L. Shepard, and P. Kim. Electronic compressibility of gapped bilayer graphene. *arXiv:1004.5556v2*, 2010.

[75] L. A. Ponomarenko, R. Yang, R. V. Gorbachev, P. Blake, A. S. Mayorov, K. S. Novoselov, M. I. Katsnelson, and A. K. Geim. Density of States and Zero Landau Level Probed through Capacitance of Graphene. *Phys. Rev. Lett.*, 105(13):136801, 2010.

[76] Y. Zhang, Z. Jiang, J. P. Small, M. S. Purewal, Y. W. Tan, M. Fazlollahi, J. D. Chudow, J. A. Jaszczak, H. L. Stormer, and P. Kim. Landau-Level Splitting in Graphene in High Magnetic Fields. *Phys. Rev. Lett.*, 96(13):136806, 2006.

[77] W. Zhu, Q. W. Shi, X. R. Wang, J. Chen, J. L. Yang, and J. G. Hou. Shape of Disorder-Broadened Landau Subbands in Graphene. *Phys. Rev. Lett.*, 102:056803, Feb 2009.

[78] Y. Zhang, Z. Jiang, J. P. Small, M. S. Purewal, Y.-W. Tan, M. Fazlollahi, J. D. Chudow, J. A. Jaszczak, H. L. Stormer, and P. Kim. Landau-Level Splitting in Graphene in High Magnetic Fields. *Phys. Rev. Lett.*, 96:136806, Apr 2006.

[79] Guohong Li, Adina Luican, and Eva Y. Andrei. Scanning Tunneling Spectroscopy of Graphene on Graphite. *Phys. Rev. Lett.*, 102(17):176804, 2009.

[80] David L. Miller, Kevin D. Kubista, Gregory M. Rutter, Ming Ruan, Walt A. de Heer, Phillip N. First, and Joseph A. Stroscio. Observing the Quantization of Zero Mass Carriers in Graphene. *Science*, 324(5929):924–927, 2009.

[81] W. Zhu, H. Y. Yuan, Q. W. Shi, J. G. Hou, and X. R. Wang. Shape of the Landau subbands in disordered graphene. *Phys. Rev. B*, 83:153408, Apr 2011.

[82] T. Ohta, A. Bostwick, T. Seyller, K. Horn, and E. Rotenberg. Controlling the electronic structure of bilayer graphene. *Science*, 313:951–954, 2006.

[83] Eduardo V. Castro, K. S. Novoselov, S. V. Morozov, N. M. R. Peres, J. M. B. Lopes dos Santos, Johan Nilsson, F. Guinea, A. K. Geim, and A. H. Castro Neto. Biased Bilayer Graphene: Semiconductor with a Gap Tunable by the Electric Field Effect. *Phys. Rev. Lett.*, 99(21):216802–4, 2007.

[84] Jeroen B. Oostinga, Hubert B. Heersche, Xinglan Liu, Alberto F. Morpurgo, and Lieven M. K. Vandersypen. Gate-induced insulating state in bilayer graphene devices. *Nat Mater*, advanced online publication, 2007.

[85] Benjamin E. Feldman, Jens Martin, and Amir Yacoby. Broken-symmetry states and divergent resistance in suspended bilayer graphene. *Nat Phys*, 5(12):889–893, 2009.

[86] Y. Zhao, P. Cadden-Zimansky, Z. Jiang, and P. Kim. Symmetry Breaking in the Zero-Energy Landau Level in Bilayer Graphene. *Phys. Rev. Lett.*, 104:066801, Feb 2010.

[87] Yafis Barlas, R. Côté, K. Nomura, and A. H. MacDonald. Intra-Landau-Level Cyclotron Resonance in Bilayer Graphene. *Phys. Rev. Lett.*, 101:097601, Aug 2008.

[88] M. J. Dignam, W. R. Fawcett, and H. Bohni. The Kinetics and Mechanism of Oxidation of Superpurity Aluminum in Dry Oxygen. *Journal of The Electrochemical Society*, 113(7):656–662, 1966.

[89] Masaaki Nakamura, Eduardo V. Castro, and Balázs Dóra. Valley Symmetry Breaking in Bilayer Graphene: A Test of the Minimal Model. *Phys. Rev. Lett.*, 103:266804, Dec 2009.

[90] K. Zou and J. Zhu. Transport in gapped bilayer graphene: The role of potential fluctuations. *Phys. Rev. B*, 82:081407, Aug 2010.

[91] Thiti Taychatanapat and Pablo Jarillo-Herrero. Electronic Transport in Dual-Gated Bilayer Graphene at Large Displacement Fields. *Phys. Rev. Lett.*, 105:166601, Oct 2010.

[92] E. V. Gorbar, V. P. Gusynin, and V. A. Miransky. Dynamics and phase diagram of the $\nu = 0$ quantum Hall state in bilayer graphene. *Phys. Rev. B*, 81:155451, Apr 2010.

[93] R. Nandkishore and L. S. Levitov. *arXiv:1002.1966*, 2010.

[94] Csaba Tőke and Vladimir I. Fal'ko. Intra-Landau-level magnetoexcitons and the transition between quantum Hall states in undoped bilayer graphene. *Phys. Rev. B*, 83:115455, Mar 2011.

[95] A. Sawada, Z. F. Ezawa, H. Ohno, Y. Horikoshi, Y. Ohno, S. Kishimoto, F. Matsukura, M. Yasumoto, and A. Urayama. Phase Transition in the $\nu = 2$ Bilayer Quantum Hall State. *Phys. Rev. Lett.*, 80:4534–4537, May 1998.

[96] L. Brey, E. Demler, and S. Das Sarma. Electromodulation of the Bilayered $\nu = 2$ Quantum Hall Phase Diagram. *Phys. Rev. Lett.*, 83:168–171, Jul 1999.

[97] A. H. MacDonald, R. Rajaraman, and T. Jungwirth. Broken-symmetry ground states in $\nu = 2$ bilayer quantum Hall systems. *Phys. Rev. B*, 60:8817–8826, Sep 1999.

[98] R. T. Weitz, M. T. Allen, B. E. Feldman, J. Martin, and A. Yacoby. Broken-Symmetry States in Doubly Gated Suspended Bilayer Graphene. *Science*, 330(6005):812–816, 2010.

[99] K. I. Bolotin, K. J. Sikes, Z. Jiang, M. Klima, G. Fudenberg, J. Hone, P. Kim, and H. L. Stormer. Ultrahigh electron mobility in suspended graphene. *Solid State Commun.*, 146(9-10):351–355, 2008.

[100] Allan H. MacDonald Inti Sodemann, D. A. Pesin. Interaction-Enhanced Coherence Between Two-Dimensional Dirac Layers. *arXiv:1203.3594*, 2012.

[101] E. P. De Poortere, H. L. Stormer, L. M. Huang, S. J. Wind, S. O'Brien, M. Huang, and J. Hone. 1- to 2-nm-wide nanogaps fabricated with single-walled carbon nanotube shadow masks. volume 24, pages 3213–3216. AVS, 2006.